Comprehensive Study of Cumulus Cloud Initiation Observed by High-Resolution BLR, Doppler Lidar, and Time Lapse Camera using Wavelet Approach

Ginaldi Ari Nugroho

2022

Acknowledgment

I want to express my gratitude to Professor Eiichi Nakakita, who has supervised, supported and guided me with kindness. I want to express my greatest appreciation to Dr. Kosei Yamaguchi, who has spent time discussing, guiding, and showing new ideas for my research. I want to express my appreciation to Prof. Kenji Tanaka for his guidance as my sub-supervisor. I want to thank Dr. Naka Yukari, who taught me about CReSS and for her input on my research.

I want to thank Prof. Kazuhiro Tsuboki, Dr. Masayuki Yamamoto, Dr. Seiji Kawamura, Dr. Hironori Iwai, Dr. Tadayasu Ohigashi, Dr. Taro Shinoda for the discussion and support of my research journal.

I would like to acknowledge that this study used Ka-band radar data from Nagoya University, Doppler lidar data in collaboration with NICT (National Institute of Information and Communications Technology), and Himawari-8 satellite data from JMA (Japan Meteorological Agency).

I want to thank Prof. Hubert Luce, Dr. Ying-Hsin Wu, Dr. Mariko Ogawa, Dr. Kazuyoshi Souma, and Dr. Satoshi Watanabe for the research discussion. I want to thank Tsuji san for helping me with many difficult documents and administration. I want to thank Ono san for his help, discussion, and guidance. I want to thank Ana san, and Yeon san for their help and support throughout our Doctoral study. I also want to thank all members of Nakakita Laboratory for their help, kindness, and warm welcome.

This study was partially supported by JSPS KAKENHI, Grant numbers 15H05765, 20H02258, 16K12861. I also acknowledge and value the financial support from Indonesia Endowment Fund for Education (LPDP) for my scholarship.

I want to thank Dr. Wendi Harjupa for introducing me to Nakakita Lab and supporting me during my early stay in Kyoto. I want to thank Prof. Thomas Djamaluddin, Prof. Eddy Hermawan, Mr. Halimurrahman, Mr. Afif Budiyono, and Dr. Didi Satiadi, who have encouraged and supported me in applying for the scholarship and studying at Kyoto University. I want to thank all LAPAN and BRIN staff members for their help and support.

I am deeply grateful for my mother and family, who support and pray for me. My deepest appreciation for my lovely wife Nur Hayati and my son Haidar Takahiro Nugroho who accompany, encourage, and give positive energy all the time. I want to thank all Indonesian family members in Kyoto who have helped my family to enjoy living in Japan.

August 2022

Ginaldi Ari Nugroho

Abstract

The impact of the short-period isolated heavy rainfall on flash floods has proven to cause many damaging effects, including fatalities. This short period of rainfall that lasted only about 1 hour is referred to as Guerrilla heavy rainfall (GHR) in Japan. This short period of rainfall also occurs in Indonesia. Early detection of GHR is essential to minimize the damaging impact. The lead time of early detection would give valuable time for mitigating prevention action.

In order to gain more lead time, it is necessary to observe the source of the GHR, which is the initiation of the start of the cloud or cloud initiation. That is why the objective of this study is to observe the cloud initiation before the cloud could generate into a baby rain cell. Another objective is to find another parameter that could be used as an early indicator compared with the previous study. The benefit of analyzing the cloud initiation is that it could also give a better understanding of the mechanism of cloud development.

This study observed cloud initiation from three main instruments with high temporal resolution. **Chapter 3** describes the instrument that is used in this research. The main instruments are time-lapse camera, advanced boundary layer radar (BLR), and Doppler lidar. Time-lapse camera is used to observe the visual evolution of cumulus cloud development, cloud growth size, and period of cloud initiation. Advanced BLR is used to observe the vertical movement, thermal plume activity, horizontal wind direction, and boundary layer condition. Meanwhile, Doppler lidar is used to detect the vertical vorticity during the cloud initiation. An additional instrument such as Ka-band radar, Radiosonde, and Himawari satellite was also utilized to observe the baby rain cell first echo, wind condition, atmospheric instability, and cloud albedo. Utilizing high-resolution observation data from multiple

instruments will give detailed information on the cloud initiation process.

Several methods were used in this study to analyze the observation data. Pseudo vorticity is used to derive the vertical vorticity from Doppler lidar data. Image processing is used to extract quantitative information from the camera cloud image. Doppler beam swinging derives the horizontal wind profile from the BLR data. The observation is taken place in Kobe urban area, Japan. We limit the observation data for analysis from 2018 until 2020 during the summer season (July until September). We also used a wavelet to handle several time series data with high temporal resolution. In **chapter 4**, we briefly describe the wavelet. This study mainly uses Wavelet to analyze these different kinds of data for comparison. Wavelet is suitable for locating the small-coherent signal within the time series data. Wavelet could analyze the time series of the data in the time domain and frequency domain. The appropriate wavelet function or mother wavelet could determine which target to analyze.

Chapter 5 showed two examples of wavelet applications. The first example is to quantify the coherent vertical movement of the thermal plume. A thermal plume can be expressed as a column of rising air moving from the surface into the atmosphere. Advanced BLR could detect this thermal plume profile in a rapid time interval. Using the wavelet, we could observe the coherent structure of the thermal plume in the time and frequency domains. In the time domain, we could analyze the early start of the thermal plume and how long the thermal plume would last. In the frequency domain, we could observe the frequency occurrence of different kinds of thermal plumes based on their scale period. The second example of the wavelet application is its ability to detect the coherent structure of the downdraft-updraft combination during thermal plume activity. The test performance showed that the paul wavelet is the appropriate mother wavelet to detect the downdraft-updraft combination. Continuous wavelet transforms first dimension (CWT 1D) combined with the BLR can resolve these structures and quantify it according to height and period.

Wavelet could also be used to study the non-linear impact of the thermal plume on the cumulus cloud initial stage. This process is described in detail in **chapter 6**. The quantized leading phase coherence ($-\pi/2-\pi/4 < \Delta\varphi < -\pi/2+\pi/4$) expresses the relationship between thermal and cumulus cloud initial stage. From the wavelet scale period, we found that at least it needs more than two minutes from the start of the thermal plume to impact the initial stage of the new individual cumulus cloud. We found several vertical vorticities observed by Doppler lidar in the initial stage of cumulus cloud, ranging from $\pm$ 0.001 s^{-1} to $\pm$ 0.01 s^{-1}.

We found a pair of small vertical vorticity in two consecutive layers heights (vortex tube) observed by Doppler lidar during the first echo of the Ka-band radar. This new finding is described in **chapter 7**. The pair of vertical vorticity from Doppler lidar has a value from $\pm$ 0.002 s^{-1} until $\pm$ 0.006 s^{-1}. Meanwhile, the vertical vorticity from Ka-band radar has a value from $\pm$ 0.01 s^{-1} until $\pm$ 0.02 s^{-1}. The vortex tube from Doppler lidar seems related to vertical vorticity from Ka-band radar since the location and orientation are almost similar. This vortex tube is also observed five to nine minutes before the Ka-band first echo. Information on the atmospheric condition is also observed during this period.

In conclusion, from a series of investigations using three main instruments and several other data, we could observe the cumulus cloud initiation in the initial stage and the stage where the Ka-band radar first echo appears. The description and schematic of this conclusion are depicted in **chapter 8**. At the early stage of the cumulus cloud, the initiation is strongly related to thermal plume activity. Several events showed that the impact of the thermal plume activity could generate small vertical vorticity during this stage. Meanwhile, we found a small vortex tube below the cumulus cloud location in the Ka-band radar first echo stage. Since this small vortex tube also occurs several minutes before the first echo, this new finding could be considered another parameter for the early detection of GHR.

Acronym and abbreviation

Acronym	**Abbreviation**
ACS	Adaptive clutter suppression
AHI	Advanced Himawari Imagers
AVI	Audio Video Interleave
BLR	Boundary layer radar
CNR	Carrier to noise ratio
COI	Cone of influence
CPA	Cloud Pixel Area
CWT	Continuous wavelet transform
DBS	Doppler Beam Swinging
dB	Decibel
Fps	Frame per second
GHR	Guerrilla Heavy Rainfall
GPS	Global Positioning System
HDR	High Dynamic Range
JST	Japan Standard Time
LCL	Lifting Condensation Level
LFC	Level of Free Convection
LIDAR	Light detecting and ranging
MSM	Meso Scale Model
OS	Over sampling
PPI	Plan position indicator
PRF	Pulse Repetition Frequency
RADAR	Radio detecting and ranging
RIM	Range imaging
RH	Relative Humidity
RHI	Range height indicator
SNR	Signal to noise ratio
VAV	Vertical Air Velocity
WPR	Wind profile radar

Table of contents

List of Figures

List of tables

List of symbols

ζ	Vorticity
ϕ	Phase coherence
$\Delta\phi$	Phase coherence difference
$R^2{}_n$	Wavelet coherence level
W^x , W^y	Wavelet power spectrum
W^{xy}	Cross wavelet
φ	Elevation angle
α	Azimuth angle
θ	Zenith angle
Ψ^*	Complex conjugate of the wavelet function
δt	Sampling interval
s	Wavelet scale
j	Number of wavelet scales used
δj	Wavelet scale interval

Chapter 1. Introduction

1.1. Background

A short period of localized heavy rainfall has frequently occurred in recent years. These short heavy rainfall will cause a sudden downpour of rainfall. This sudden downpour is one factor that could trigger a flash flood, especially in an urban area. The impact of the flash flood could be devastating since it could cause damage and even casualties of human lives. In Indonesia, one example was the short period of heavy rainfall in Bandung on March 17, 2017. This rainfall caused flash floods and damaged many houses, building even vehicles, with several casualties. Observed reflectivity from the X-band radar CAPPI product could capture the initial stage of the cumulonimbus cloud in 10:50 Local time (Nugroho et al., 2019). CAPPI from 1 km to 8 km showed vertical reflectivity representing the cumulonimbus cloud. The radial velocity data showed two rotation (vorticity couplet) during the initial stage. Himawari satellite RGB data also confirm this heavy rainfall event.

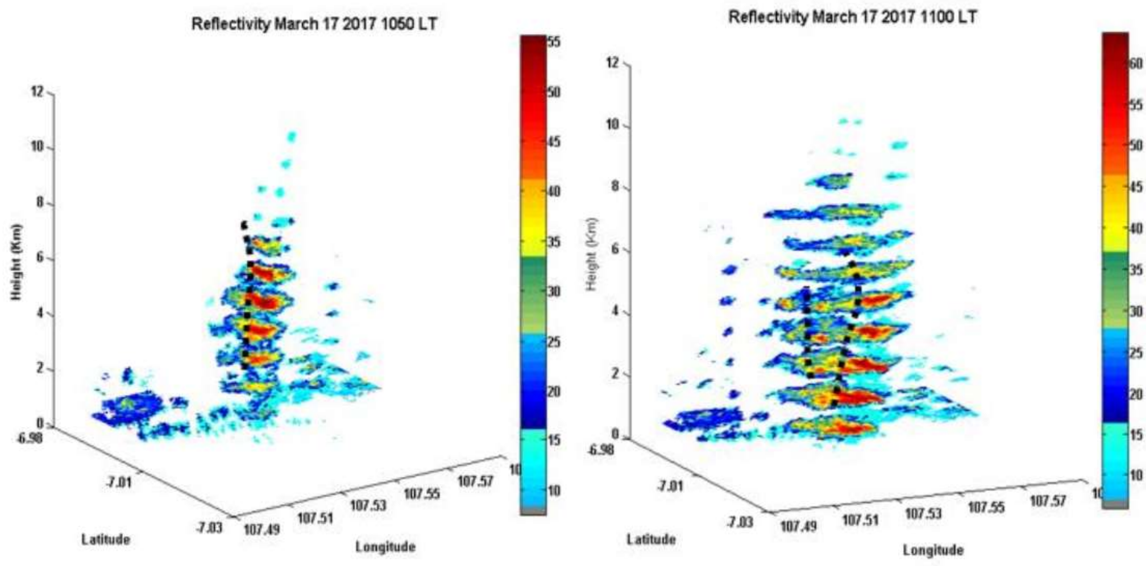

(a)

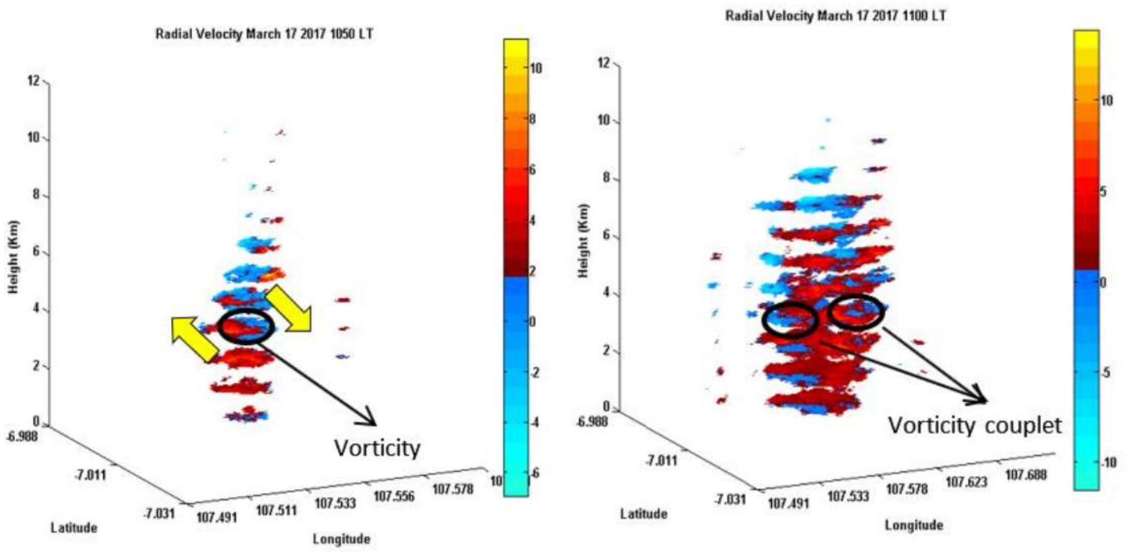

(b)

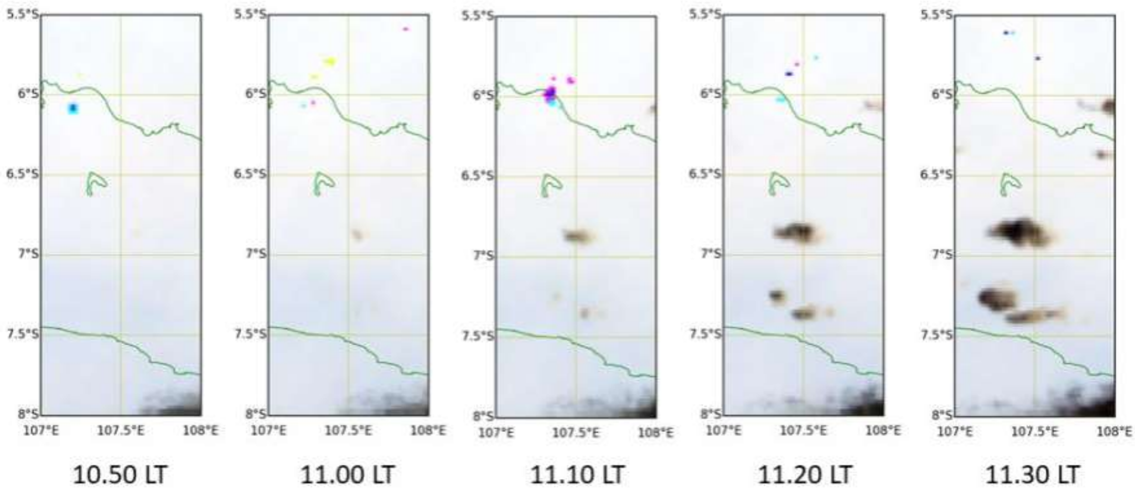

(c)

Figure 1.1. Observation data during a short period of heavy rainfall in Bandung Indonesia, a) Reflectivity from X-band radar, b) Radial velocity from X-band radar, c) Water vapour distribution derived from RGB Himawari-8 satellite (Nugroho et al., 2019).

In Japan, the short period of localized heavy rainfall is often known as guerrilla heavy rainfall (hereafter abbreviated as GHR). One example of the impact of GHR that impacts human lives is the Toga river Kobe Japan event on July 28, 2008. This GHR caused a flash flood that hit the Togagawa river basin from 14:40 JST until 15:00 JST.

From ground-based rain gauge observation, a 10 min period of rainfall was particularly intense in Nagamine and Tsurukabuto starting at 14:40 JST. At the Kobashi water level station, the water level rose 1.34 meters in 10 min between 14:40 JST and 14:50 JST, almost simultaneously with the downpour of the rainfall. The camera image from CCTV also captures the flash flood event. This flash flood killed five people (including children), with eleven people rescued and forty-one people evacuated.

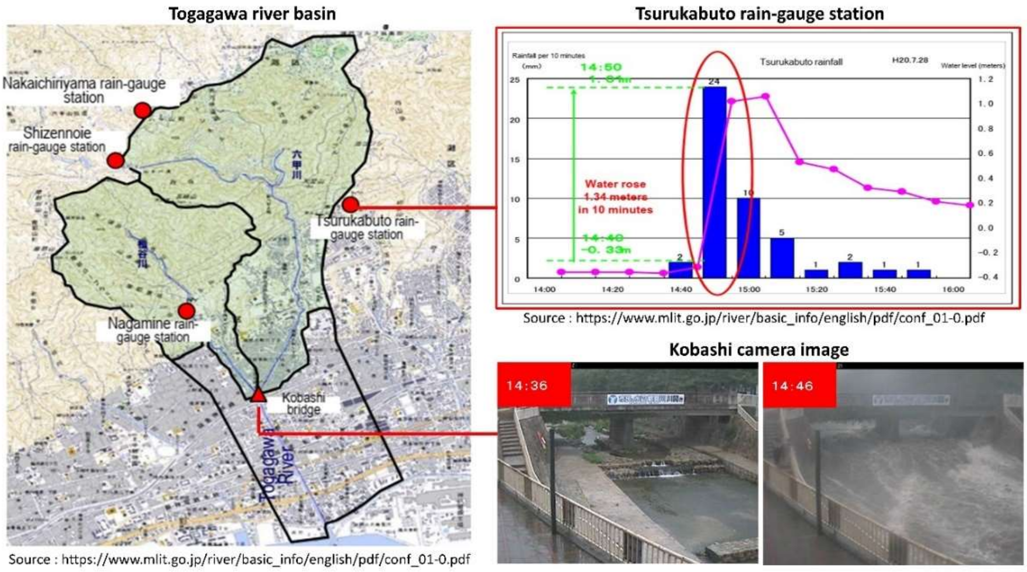

(a)

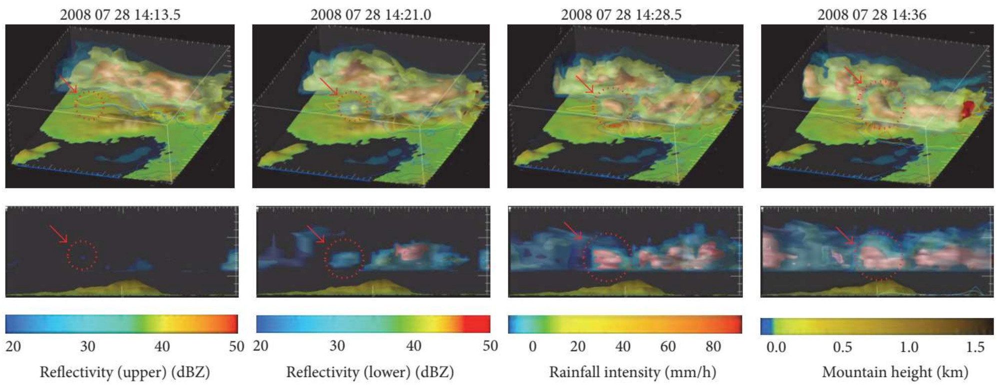

(b)

Figure 1. 2. Example of localized heavy rainfall in Togagawa river basin Kobe city of Japan, a) Ground-based observation, b) C-band radar observation (Nakakita et al., 2017)

In order to reduce the damage, it is essential to detect the localized heavy rainfall more early. Research for detecting the early stage before heavy rainfall occur have been done by Nakakita et al. (2017). The early stage is based on the first echo (baby rain cell) captured by the weather radar (Fig 1.2). The combination between the first echo and vertical vorticity tube detection has been further developed into an established X band network system (XRAIN) operated by MLIT.

The life stage of GHR is illustrated in figure 1.3. There are three-stage, initial stage, mature stage and developed stage. Most concern on disaster prevention is the initial stage (steps 1 until 3 in Fig 1.3), where the lead time period only lasted from 10 to 15 min. Previous research by Nakakita et al. (2017) showed that the first echo of cumulonimbus cloud detected by XRAIN (point 1) that contain a vertical vortex tube (step 2) has a bigger chance of generating GHR. However, it is essential to investigate the mechanism before the initial cloud stage (before step 1) to obtain more lead time.

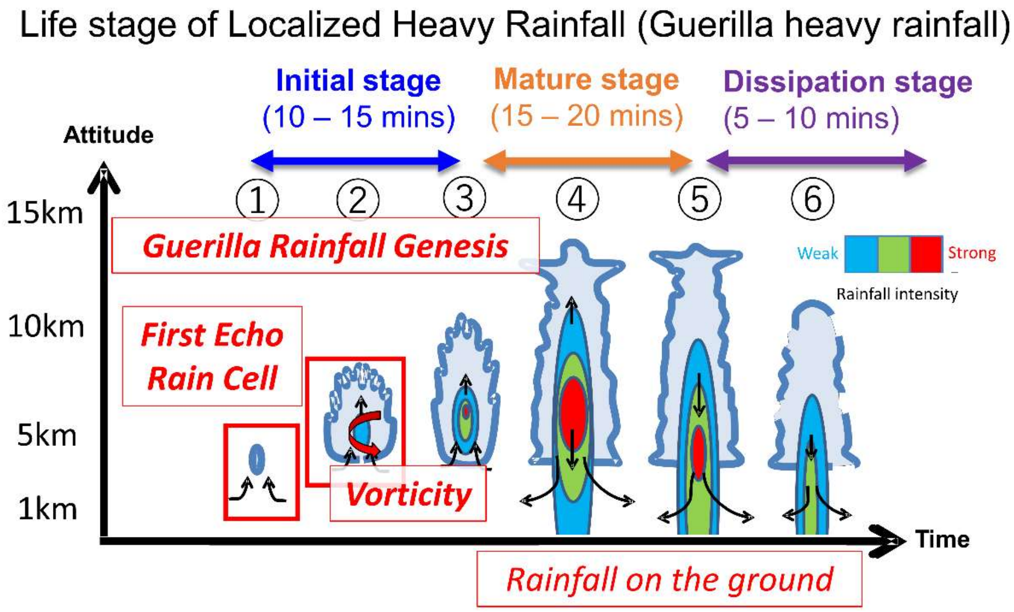

Figure 1. 3. Guerilla heavy rainfall life stage.

Another essential parameter is the cloud initiation before it generates into a baby rain cell. The early process of the cloud initiation, especially the cumulus cloud type that could combine or generate into a cumulonimbus cloud, is essential for revealing the mechanism of the early stage of Guerrilla heavy rainfall. In order to observe the mechanism of this early process, multiple data from different instruments are needed. The data sources in this study are from multiple observations based on several instruments in Kobe city of Japan. This is an opportunity because there were not enough instruments in Indonesia to do this complete observation. Japan has a rapid operational instrument that can measure many parameters related to the convection mechanism.

1.2. Significance of the study

Many cumulus cloud initiation research projects have been conducted to study the convective activity, but no research correlates it with the baby cell generation. This research would benefit the early detection of heavy rainfall, especially the localized category of heavy rainfall. Using a combination of the high resolution of multi-sensor for observation will give a more detailed and different perspective on the interaction and mechanism between cumulus cloud initiation and baby cell generation. The experience and knowledge from this study on cumulus cloud initiation detection before the baby cell generation will be very useful for future localized heavy rainfall studies in Japan and Indonesia.

1.3. Structure of dissertation

The objectives of the study are to investigate the cumulus cloud initiation process using several high-resolution instruments and also wavelet, in order to increase the lead time before the initial stage of guerrilla heavy rainfall. The flow structure of this dissertation is illustrated in Figure 1.2, with the detailed structure as follows:

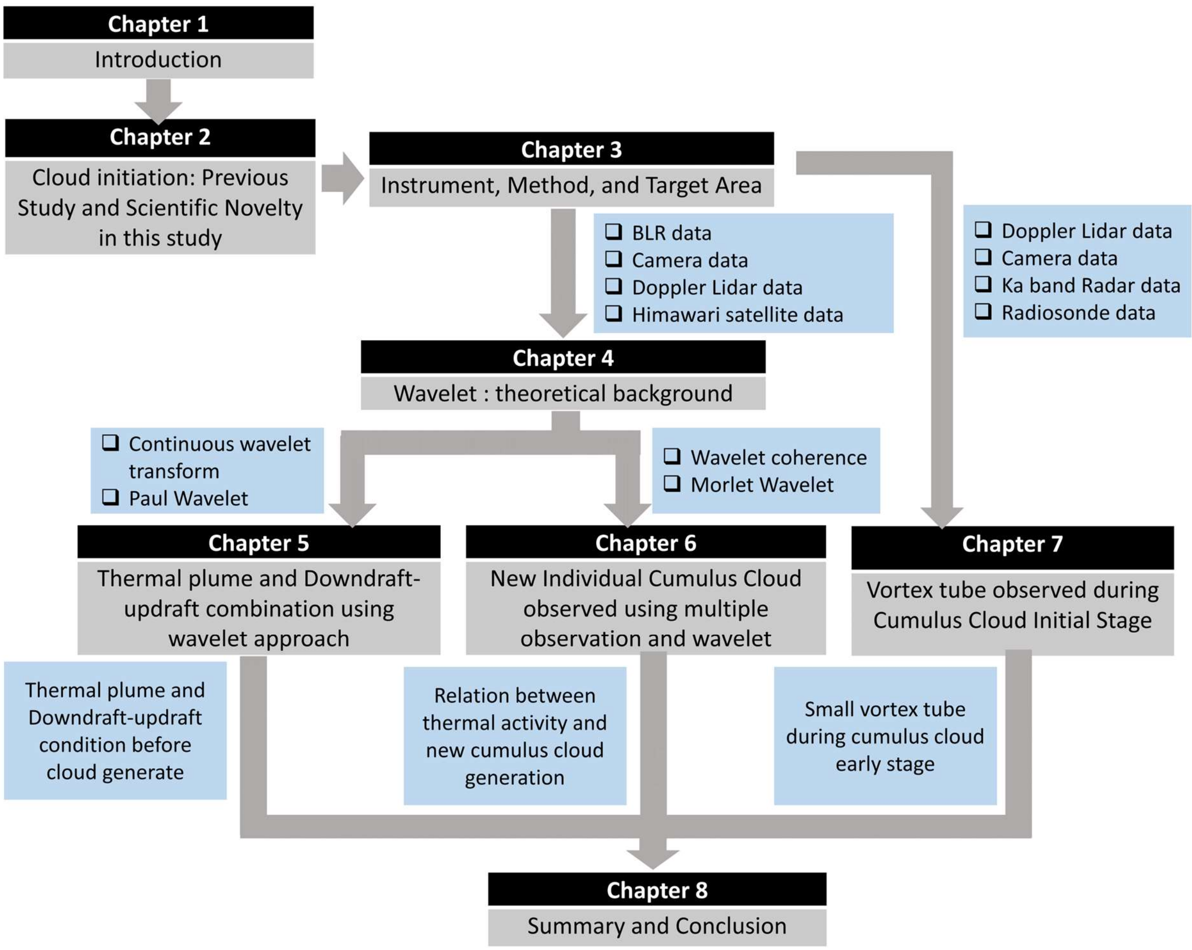

Figure 1.4. Flow structure of the dissertation. The black-grey rectangle represents the chapter number and title. Meanwhile, the blue rectangle represents the main input for the next chapter.

- Chapter 2 describes previous research related to the cumulus cloud initiation process. This chapter introduces the novelty in relation to pair vorticity detection using several instruments.
- Chapter 3 provides detailed information on the research location, specification of each instrument used, and method applied in this study.

- Chapter 4 describes the wavelet theoretical background and its properties.
- Chapter 5 discuss the wavelet approach to the thermal plume and downdraft-updraft combination.
- Chapter 6 elaborates on wavelet application for revealing the relationship between thermal plume with individual cumulus cloud and vorticity detection during this period.
- Chapter 7 investigate the vorticity condition before and during the early stage of the Ka-band radar first echo.
- Chapter 8 describes the summary of the cumulus cloud initiation process and the conclusion of this study.

Chapter 2. Cloud initiation: Previous research and Scientific novelty in this study

2.1. Cumulus cloud initiation process

Previous research by Nakakita et al. (2017) has achieved an early detection of GHR by detecting the first echo of a rain cell or “baby rain cell” using X-band radar. Baby rain cell is a term used to describe the first precipitation genesis that forms inside the cloud. Another type of radar, Ka-band radar, has higher sensitivity for baby rain cell detection than X-band radar.

Several studies utilize Ka-band radar first echo to observe the early stage of cumulus cloud (Nakakita et al.,2017; Knight and Miller, 1994) as a convective initiation indicator. Knight stressed the difficulty of using a higher frequency of Ka-band radar to detect the first echo due to its high sensitivity to interference (Knight and Miller, 1993). Utilizing Ka-band radar with SNR pre-processing gives better information on the first echo of the cloud. Previous research by Nakakita et al. (2017b) investigates the relationship between Ka-band radar first echo height and the LCL (Lifting Condensation Level). Nakakita et al. (2017) observe the power reflectivity of the radar data and derive the vertical vorticity inside the first echo. Comparison of the lead time of first echo and vertical vorticity detected by Ka-band radar and X-band radar is also investigated. The result revealed that Ka-band radar was detected earlier than X-band radar on those two (first echo and vertical vorticity).

The vertical vorticity structure was previously investigated concerning the generation of a supercell (Rotunno,1981; Klemp, J.B, 1987; Cotton et al., 2010). The mechanism of the vertical vorticity is illustrated in Figure 1.4. Vertical vorticity is related to horizontal vorticity conditions. Firstly, horizontal vorticity occurs due to the vertical shear of the horizontal wind. The presence of updraft will cause the horizontal vorticity to tilt, causing a pair of vertical vorticity with different orientations (positive and negative vorticity). Positive vorticity will be generated on the left side of the updraft relative to the shear flow. Meanwhile, negative vorticity will be generated on the right side of the updraft. The strong updraft will amplify the pair of vorticity to a higher altitude in the form of a stretching motion. The pair of vorticity is exist along the updraft that represent vortex tube (Nakakita et al, 2017a; Nakakita et al, 2017b).

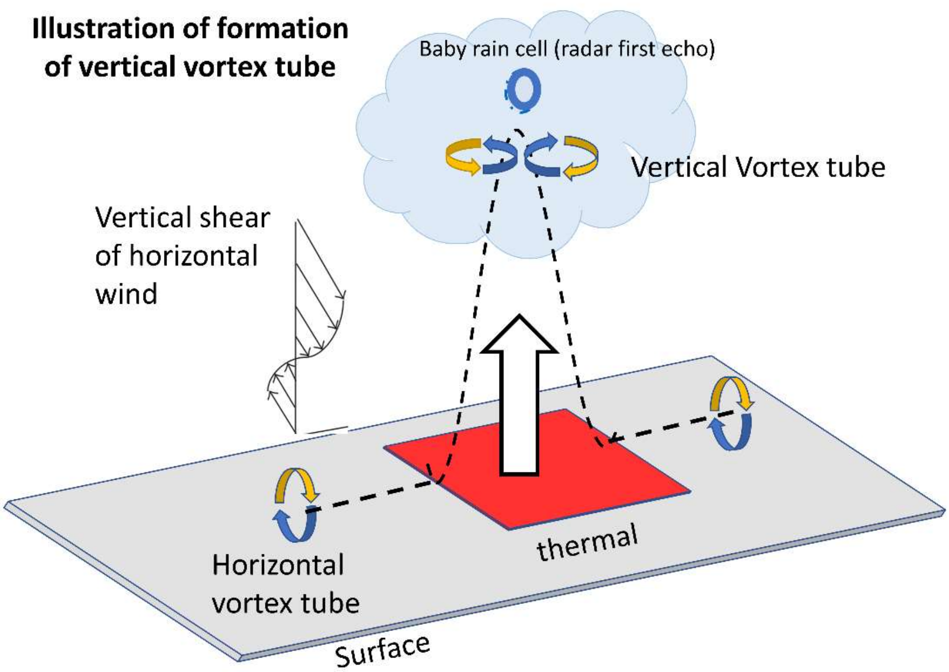

Figure 2.1. Illustration of vertical vortex tube generation.

Another question remains, what causes the updraft that creates vortex formulation. Many lifting parcel mechanisms can affect the updraft, but perhaps the answer to the question will be the convection factor. Convection happens naturally in the atmosphere where a particular area on the ground surface is heated by the sun and increases the air temperature unevenly, and the expanded warm air is buoyed upward and rises (Ahrens, 1993). Three criteria must be observed for the convection: first is where the convection will occur, second is when the convection will occur, and third is at what level the convection will occur.

Localized lifting is usually the key to determining precisely where and when convection will be triggered. (Browning et al., 2007). Localized lifting in the column of rising air that moves from the surface into the atmosphere is called thermal. Several studies have investigated many kinds of thermal. Thermal in the form of plumes that extended into the boundary layer height have an important role in the mixed layer condition (Rio and Hourdin, 2008). In a single cell cloud simulation, thermal presence could change circulation by increasing the updraft strength. Thermal could trigger the formation of cloud cell structure and then develop larger clouds (Klinger et al., 2017). A complete study on the air motion, especially the vertical velocity, is needed in this case.

In a convective parameterization scheme, the possibility for convection is assessed based on a set of rules, collectively known as the trigger function. The trigger function activates the convection parameterization scheme if it detects a potential for deep convection. One of the trigger function convective schemes was done by Donner scheme (Donner, 1993). One of the most difficult aspects of convection is its initiation. This difficulty is due to the many atmospheric processes influencing the vertical thermodynamic structure in which convection occurs and how it is initiated (Trier S B, 2003).

Another essential parameter is the cloud type itself. Not all clouds could generate into GHR. From WMO (World Meteorological Organization), there are ten genera which consist of cloud “species” and “varieties” that describe the cloud shape – structure, and transparency – arrangement, respectively. However, only several types of these clouds could generate precipitation. The cumulus cloud type is one of these types that has a significant part in generating precipitation. Cumulus cloud is the primary source of precipitation in the low latitude region. Meanwhile, the cumulus cloud in the warm season is the primary source of precipitation in the higher latitude region (Wang et al., 2009). Several studies have been investigating the properties of the cumulus cloud, starting from its geometry properties (Sengupta et al., 1990), microphysics inside of it (Hudson and Noble, 2021), and the transition from shallow cumulus into moderate deep cumulus cloud (Wang et al., 2009).

The early initiation of a cumulus cloud is a relatively difficult topic to analyze. The main reason is the rapid process of the initiation stage in a short duration. Several studies have used numerical simulation to observe this early process (Klinger et al., 2017). One parameter already confirmed as an important factor of the cumulus cloud initiation is the increased updraft from the convective plume on the surface (Lopez, 1977; Mecikalski et al., 2015; Tian et al., 2021). The early process of the cloud initiation, especially the cumulus cloud type that could combine or generate into a cumulonimbus cloud, is essential for revealing the early stage of GHR.

2.2. Multiple observation for cloud observation

In order to observe the mechanism of this early stage of cumulus cloud, multiple data from different instruments are needed. The mechanism depicted in Fig 2.1 showed several indicators that should be investigated to understand more about the mechanism of the cumulus cloud initiation. The first indicator is the local uplift force in the form of thermal. Vertical profile observation, such as wind profile radar, is a suitable instrument to observe the condition of the updraft in the boundary layer. Not only observe the updraft structure vertically, but a wind profile with a particular setting could derive the wind profile horizontally (Fukao and Hamazu, 2014). However, to capture small scale variations of the coherent structure of updraft (thermal plume) in a short period as a representation of the thermal activity, it is essential to utilize a more advanced high-resolution wind profiler.

Another instrument that could obtain vertical structure is lidar. Doppler lidar has a similar principle to radar, but instead of using electromagnetic energy pulses, it uses infrared pulses (Newsom and Krishnamurthy, 2020). Doppler lidar can become a validator for the occurrence of the updraft, have a higher sensitivity, and observe convergency.

Other researchers have utilized various instruments (Lopez R.E, 1977; Zhang and Klein, 2012; Iwai et al., 2017; Misumi et al., 2017; Romps and Öktem, 2018) to obtain more detailed information on the early stage of cloud. There is some similarity with the previous study in that they utilize cameras to observe the cloud process. A Time lapse camera can be utilized to capture the cloud image and quantize some information about the cloud properties, such as cloud height (Misumi et al., 2017) and cloud thickness (Romps and Öktem, 2018).

2.3. Wavelet utilization in atmospheric research

A wavelet is a tool that can be utilized in various research fields, including research in atmospheric study. Terradellas et al. (2000) use a wavelet to study the atmospheric boundary layer in non-stationary conditions. Wavelet could obtain the spectral content of the non-stationary time series data and its evolution in time. Since the evolution of certain characteristics of wave-like events can be observed, the displacement characteristic of a coherent moving structure could also be observed.

Wavelet results can also analyze qualitatively and quantitatively. Torrence and campo (1998) introduced a wavelet analysis toolkit that includes statistical significance testing. The significant comparison between the peak of the wavelet power spectrum and the background spectrum can be used as a significance level in the form of confidence level percentage. This percentage can be used as a qualitative measurement of the actual feature of the certain or localized characterized structure.

The localized structure could be quantitatively analyzed using a wavelet regarding time and frequency. Yano and Jakubiak (2016) have investigated the wavelet method application to quantify the localization and scale of the QPF (Quantitative Precipitation Forecast) errors. The coherent structure is represented by the significance level area consisting of coordinated wavenumbers of the peak wavelet power spectrum. This study uses the wavelet ability to locate and extract certain localized features quantitatively.

The importance of the type of wavelet used also needs to be considered. Grinsted et al. (2004) choose morlet wavelet in their study since it balances the time and frequency localization. Yano and Jakubiak (2016) selected the meyer wavelet because of its smooth function form that suits the solitary waves shape type. Meanwhile, Cohn and Angevine (2000) use haar wavelet to investigate the boundary layer height and entrainment zone thickness using lidar and wind profile data. Haar wavelet is considered appropriate for analysis of a step function shape type. However, the wavelet method lacks since it is conducted in a finite-length time series. Errors will appear at the start and the end of the wavelet power spectrum. In order to overcome these errors, a boundary is introduced with the outside area where the wavelet power starts to drop, which is considered an error and can be ignored (Torrence and Campo, 1998; Wiebe et al., 2010).

Another ability of the wavelet method is to find the relationship between two variables based on the changes in frequency scale and time intervals (Ng, Eric and Chan, 2012). The wavelet method in the form of wavelet coherence gives a quantitative relation and the information of the phase angle between these two variables. Phase angle information can be useful for obtaining the confidence value of the relationship between two variables. Two time series variables with a certain relationship would be suspected to have consistent or gradual changes in the phase lag (Grinsted et al., 2004). The phase lag would give information on the relationship between the two variables.

More improvement on these methods is to use two variables and the ability to use multiple independent variables on a dependent variable (multiple wavelet coherence). Ng, Eric and Chan (2012) explore the connection between variables such as the ratio number of typhoons and tropical cyclones, relative vorticity, vertical wind shear of zonal wind, and moist static energy. Their study provided examples of the phase angle relationship (in this study is the in-phase relationship), which corresponds with the positive correlation coefficient results in the simple correlation method. Multiple wavelet coherence is useful in exploring the coherence of multiple independent variables towards a dependent variable (Ng, Eric and Chan, 2012).

2.4. Scientific novelty

The developing mechanism before baby-rain cell generation (in this term is the first echo from Ka-band radar) still lacks information. Understanding the mechanism will fully comprehend the process, which will gain more valuable time for early mitigation. This study analyzes the cumulus cloud initiation process concerning the thermal plume and vorticity factor. Utilizing high resolution observation data from multiple instruments gave detailed information on the cloud initiation process. This study reveals the pair of vorticity and vortex tube detected before and during the early generation of a cumulus cloud. This study also showed the utilization of wavelets to gain more information from the high-resolution data. The wavelet method will give another point of view of the mechanism process of the cumulus cloud initiation observed by several instruments.

Chapter 3. Instrument, method, and target area

3.1. Multiple Instrument

3.1.1 BLR

Wind profiler radar is utilized in several applications, such as measuring a vertical profile of horizontal wind for numerical weather prediction (Ishihara et al., 2006; Liu et al., 2020) and observing severe turbulence in the surface wind at the airport (Hisscott, 2019). This study uses an advanced BLR with a different performance than other wind profile radars. This advanced BLR can gain a high-resolution vertical profile of vertical wind velocity in the lower atmosphere.

The BLR in Figure 3.1 was installed in an urban area of Kobe, Japan. The Coordinate location is 34°39'56.87"N and 135°8'34.66"E, with an elevation of 47 meters above mean sea level. The distance from the nearest coastline is 2.24 km, on the south side of BLR. This instrument is equipped with range imaging (RIM) and oversampling (OS) capabilities. RIM with OS is a technique for enhancing the vertical resolution.

RIM aims to improve the range resolution by establishing sub gates using a steering vector in a sample volume based on range direction. RIM uses adaptive signal processing at each sub gate to generate time series with a wide range of precision. In order to overcome the range-weighting effect that causes the decrease in RIM accuracy, OS is then used. OS will sample the received signal (based on range direction) with a smaller interval than the transmitted pulse width-based interval. RIM with OS can resolve vertical wind perturbations with a vertical scale as small as 100 meters (Yamamoto et al., 2014).

This BLR also has the capability of adaptive clutter suppression (ACS). ACS is a technique for mitigating clutter contamination in the received signal (Yamamoto et al., 2017). ACS system composed of three subarray antennas was installed in the BLR. This subarray antenna was designed to be omnidirectional in a horizontal plane to detect clutter existing on or near the ground. Echo power and vertical wind velocity collected by the BLR are used in this study. Both of them are collected with a range sampling of 30-m intervals and a time interval of 8.192 s to resolve small-scale vertical wind variations.

Figure 3.1. BLR with ACS installed in Kobe city, Japan

BLR specification and observation parameters are briefly described in tables 3.1 and 3.2, respectively. The comparison between advanced BLR with conventional Wind Profile Radar (WPR) is that WPR is not equipped with the setting mentioned above. The disadvantage of advanced BLR is the reduced Nyquist speed and the decrease of Signal to Noise Ratio, although, in this study, this weakness is not affected the data analysis.

Table 3.1. BLR specification

Frequencies	
Center Frequency	1357.4 MHz
Maximum Number	5
Switch mode	Pulse-to-pulse basis
Main Antenna	
Type	Active phased array antenna composed of 7 Luneberg lenses
Gain	29.6 dBi
3-dB beam width	5.1°
Beam Direction (Azimuth, Zenith)	(0°, 0°), (0°, 14°), (90°, 14°), (180°, 14°), (270°, 14°)
Transmitter	
Peak Power	2.8 kW
Pulse Compression	Phase-modulation using binary codes
Receiver	
Noise Figure	1.7 dB
Gain	> 70 dB
Digital Phase Detection	Executed by the ACS System (Yamamoto et al,2017)
Real-time Signal Processing	Executed by the ACS System (Yamamoto et al,2017)
Location	
Latitude	34°39'57"N
Longitude	135°08'35"E
Sea Level Altitude	45 m

Outlier removal is conducted towards the BLR data to identify and remove the outlier. Hampel filter is used in order to execute this task. If the original signal value is declared an outlier in the Hampel filter, a moving window outlier detector will replace it with the median filter response (Pearson et al., 2016). Hampel filter with moving window is considered a dynamic filter since it identified and removed the outlier method.

Table 3.2. Observation parameter

Frequencies	1356.65 MHz 1357.00 MHz 1357.40 MHz 1357.75 MHz 1358.15 MHz
Transmitted Pulse Compression	Spano code (8bit, 16 sequences)
Sub Pulse Width	1 μs
Inter Pulse Period	50 μs
Sample Start Range	300 m
Sampling Interval	0.2 μs
Number of Sampled Points in Range	180
Number of Time Series Points	512
Collection Interval for Vertical Beam	4.096 s (2.048 s for vertical beam and 2.048 s for oblique beam)
Nyquist Velocity	13.8 m/s
Horizontal Extent of Vertical Beam (at Height of 1 km)	62.9 m
Maximum Observation Range (Altitude)	5715 m

The hampel filter is applied to BLR data along with the height. Figure 3.2 shows an example of the hampel filter applied towards the BLR vertical velocity data in a single time (11:51 JST 20180905) along with height (represented by the red rectangle). Hampel filter identified four outlier based on the upper and lower bounds of the moving window. This identified outlier is then replaced with the median value based on the lower and upper bounds.

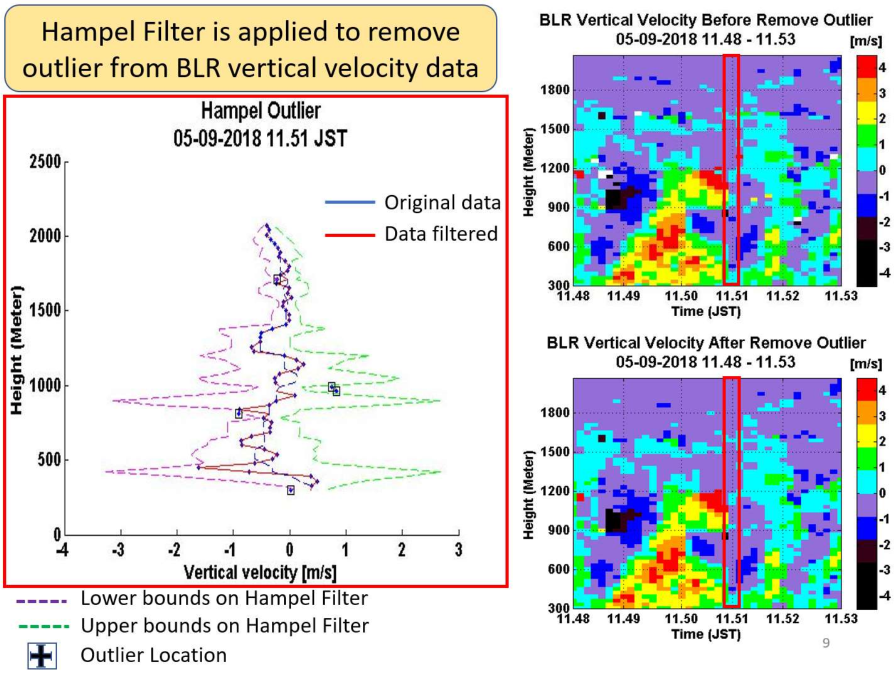

Figure 3.2. Example of Hampel filter on BLR data

3.1.2. Doppler Lidar

Doppler lidar windcube 200D is utilized in this study to observe the doppler velocity and vorticity. Doppler lidar transmits a laser pulse into the atmosphere, receives the light backscattered by aerosols, and analyzes the atmospheric properties using the received signal. The signals from moving objects have a Doppler shift proportional to their speed. Meanwhile, the time for the light pulse to travel to the target and return back to the Doppler lidar is thereby used to determine the distance of the target.

Doppler lidar is sensitive to aerosol backscattering due to its near-infrared light source. Aerosol backscattering could be used as a tracer of atmospheric wind, especially in the lower troposphere, where numerous amounts of aerosol exist. Doppler lidar has a big advantage compared with weather radar since it can observe wind conditions in the clear sky (RK Newsom and R Krishnamurthy).

Doppler velocity represents positive and negative values (unit in m/s). A positive value means the target particles move away from the Doppler lidar location. Meanwhile, a negative value indicates that target particles move towards Doppler lidar. Specification of the Doppler lidar is described in table 3.3.

Table 3.3. Doppler lidar specification

Name	Specification
Scan type	PPI and RHI
Azimuth observation range	220° - 20°
Elevation observation range	0 – 40°
Angular resolution	0.1°
Pointing accuracy	0.1°
Integration time	0.5 s
Range resolution	44.5 m
Max observation distance	7 km
Doppler speed measurement accuracy	< 0.5 m/s
Doppler velocity measurement range	-30 m/s ~ 30 m/s

The scan strategy that was applied throughout the observation period is arc scan. Arc scan is a scan configuration where Doppler lidar scan with a fixed elevation angle (focused on the lower angle) and with limited azimuth range. The advantage of this scan configuration is to increase the time sampling rate and reduce the inhomogeneity from large scale data that could impact the doppler velocity retrieval (Schwiesow et al., 1985). The advantage of a lower elevation angle is to measure doppler velocity condition near the surface (above the ground clutter) to give more information on the lower part of the wind properties, especially vorticity.

Before utilizing Doppler velocity data, it is essential to conduct quality control of the data. In previous research by Wang et al. (2015), there are three criteria in Doppler lidar Quality control; 1) Checking whether there is the carrier to noise ratio (CNR) below -20dB on the interest area, 2) Checking whether there are CNR above 10 dB that have Doppler velocity below 0.25 ms^{-1} (represent ground clutter), 3) Remove outliers from the Doppler velocity data. In this study, we used a threshold of -27 dB for criteria 1) since the Doppler lidar uses the same type of Doppler lidar as the study by Cheliotis et al. (2020).

The data that fulfilled criteria 1) and 2) are flagged as error data and are not considered for the next calculation. Outlier detection is applied using an interquartile range with the upper and lower outlier threshold based on the 25% and 75% percentiles of the Doppler velocity data in each beam (Wang et al., 2015). In order to handle the Doppler ambiguity due to the aliasing effect, a bandpass filter is used in the Doppler lidar to cancel out the doppler shift outband.

3.1.3. Ka-band radar

Ka-band radar is a radar that uses a millimeter wavelength radio wave to detect clouds. Since it uses high frequency to obtain millimeter wavelength, Ka-band radar could obtain smaller particles such as cloud droplets (Maesaka T, 2018). Ka-band radar also has a narrow beam width, so it is suitable to observe the microstructure of the cloud (Ohigashi et al., 2021).

This study uses Ka-band radar as the first echo indicator of a baby rain cell. Baby rain cell is a term used to describe the first precipitation genesis that forms inside the cloud. Several studies utilize Ka-band radar first echo to observe the early stage of cumulus cloud (Nakakita et al., 2017a; Knight et al., 1993) as a convective initiation indicator. Previous research also showed a relationship between the first echo height and the LCL (Lifting Condensation Level) (Nakakita et al., 2017b). This Ka-band radar belongs to Nagoya University and is installed at Kobe International University. Specification of the Ka-band radar is listed in table 3.4.

Table 3.4. Ka band radar specification

Name	Specification
Frequency	34.87 GHz
Wavelength	8.6 mm
Coverage area	30 Km
Location coordinate	34.68°N, 135.27°E
Height location	24 m
Range resolution	75 m
Azimuth resolution	0.35°
PRF	1980 Hz
Radar position Latitude Longitude Elevation	 35.1519 136.9719 91.7 meter

The scan strategy of the Ka-band radar is set with a total elevation angle of 11. An illustration of the scan strategy of the Ka-band radar is depicted in Figure 3.3. Equations 3.1 until 3.4 are used to estimate the Ka-band radar echo height.

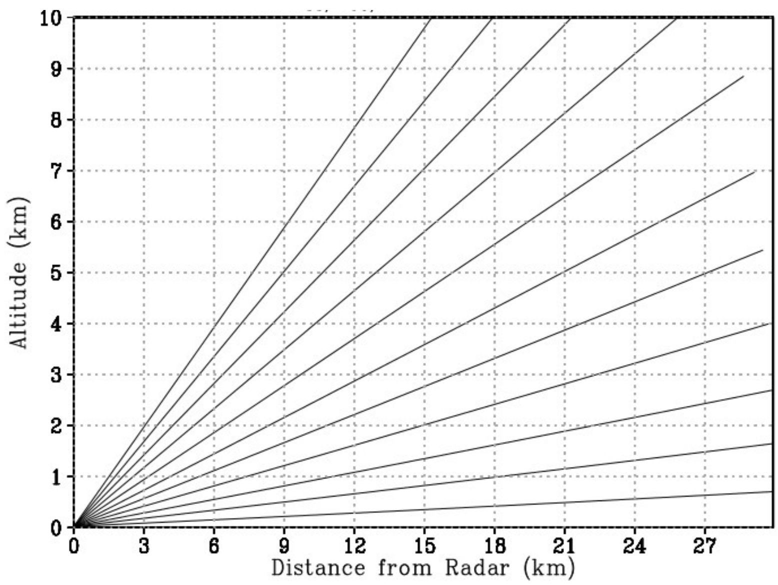

Figure 3.3. Scan strategy of Ka-band radar

$$L_d = kR_e \tan^{-1}\left(\frac{\mathrm{r}\cos\varphi_e}{kR_e + h_r + r\sin{}_{e}}\right) \quad (3.1)$$

$$H = \frac{r\,\mathrm{si}\quad {}_e+h_r+kR_e}{\cos\,\frac{L_d}{kR_e})} - kR_e \tag{3. 2}$$

$$x = L_d \sin\alpha \tag{3. 3}$$

$$y = L_d \cos\alpha \tag{3. 4}$$

Where L_d is the distance from the radar site to the point directly below the radar beam, x and y are the longitude and latitude of the target point, α is radar beam azimuth, H is the beam altitude, and r is the directional distance measured by the radar beam, R_e is the earth radius, φ_e is the observation elevation angle, and h_r is the altitude of the radar site. An illustration of how the height is estimated is illustrated in Figure 3.4 (Nakakita et al., 2017b).

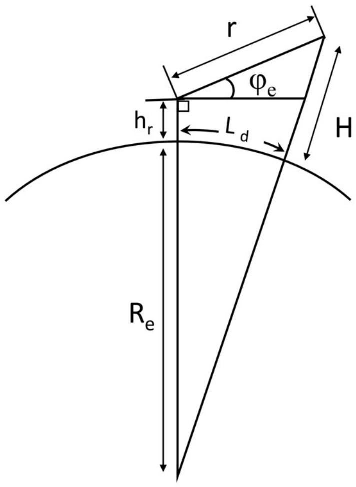

Figure 3.4. Illustration of the estimated height of Ka-band radar echo

3.1.4. Time lapse camera

Time lapse camera is an important instrument in this study. The intention of using time lapse camera is to observe the cloud evolution from time to time. Another intention is to estimate the cloud height based on the combination of several cameras. The type of time lapse camera is Brinno TLC200 pro. Three cameras are used in this study. Time synchronization is conducted within this three-camera using the NICT timestamp as the time reference. The frame rate of each camera is 10 frames per second (fps).

The location of the first camera is placed in the same location as the BLR. The setting of this camera is pointing upward to capture the cloud above BLR. Meanwhile, the other two cameras are installed 2.01 km from the BLR location. The two cameras are placed on the rooftop of a building where Doppler lidar is installed. The camera position is on the edge of the building, with a distance between each other at 76 m. The setting of this camera is pointing towards the BLR location to capture the cloud development vertically. A camera cover (weather resistant housing) is used on each camera to prevent water leakage and other outdoor effects (dust, insect, etc). An image of the time lapse camera from the Doppler lidar location is depicted in Figure 3.5.

Table 3.5. Time lapse camera specification

Name	Specification
Model	TLC200 pro
Sensor type	1/3” HDR sensor
Resolution	1.3 Mega pixel
Field of view	112°
Focal length	19 mm
Size (Depth x Width x Height)	64 x 52 x 107 mm
Weight	140 g (without batteries)
Video Format	AVI
Resolution	1280 x 720
Pixel size	4.2 µm

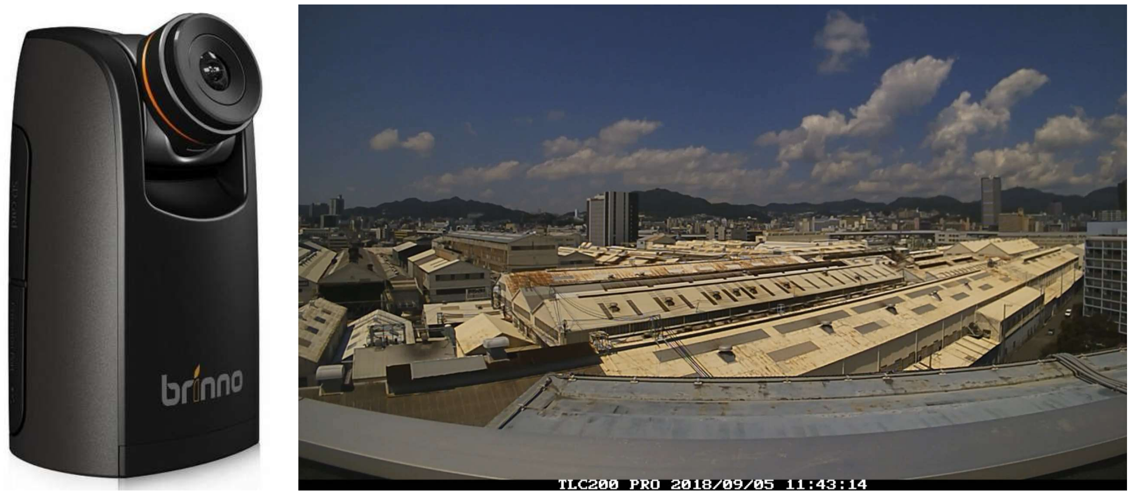

Figure 3.5. Time lapse camera and image example

3.1.5. Radiosonde

Radiosonde is a device carried by a weather balloon so that it can fly from the ground into the atmosphere. Radiosonde is equipped with a device for measuring one or more variables meteorology (pressure, temperature, humidity, etc) and a radio transmitter to transmit this information to the observation station. Some of the functions of the radiosonde are atmospheric profile research, aviation weather data, weather prediction, etc. Atmospheric parameters in every layer of the atmosphere can be identified using radiosonde.

The type of radiosonde used in this study is the RS-11G GPS radiosonde from Meisei Electric Co., Ltd. Modification on the sensor boom and high response sensor increases the accuracy of the measured temperature and humidity. Measured data are transmitted using a 400 – 406 MHz radio wave toward the ground receiving system. This type of radiosonde measure wind speed, direction, and pressure from the altitude and traveling speed of the GPS. SBAS receiver is equipped to improve the GPS positioning performance. The radiosonde is also equipped with a parachute to prevent damage when descending. Radiosonde also has an automatic rope cutter to limit the ascending height. Table 3.6 is the radiosonde specification.

Table 3.6. RS-11G GPS radiosonde specification

Temperature	Measurement range Resolution Response time Uncertainty *(a)	-90ºC to +60ºC 0.1ºC <0.4 s (1000 hPa, 5 m/s) Day time 0.5º C: Troposphere 0.8º C: Stratosphere Night time 0.4º C: Troposphere 0.4º C: Stratosphere
Humidity	Measurement range Resolution Response time Uncertainty *(b)	0% RH to 100% RH 0.1% RH < 0.2 s (Absorbing: 1000hPa. 6 m/s, 0º C) < 14 s (Absorbing: 1000hPa. 6 m/s, 60º C) 5% RH: Lower Troposphere 7% RH: Upper Troposphere
Pressure	Measurement range Resolution Uncertainty *(c)	1050 hPa to 3 hPa 0.1 hPa 0.5 hPa: 15 km 0.2 hPa: 30 km
Geopotential height of significant level	Measurement range Resolution Uncertainty *(c)	-500 m to 40.000 m 0.1 m 11 m
Wind Direction	Measurement range Resolution Uncertainty *(d)	0 deg to 359.9 deg 0.01 deg 2 deg
Wind Speed	Measurement range	0 m/s to 200 m/s

	Resolution Uncertainty	0.01 m/s 2 m/s : troposphere 3 m/s : Startosphere
Size and weight	Dimension Weight	85(W) x 67(D) x 155(H) mm 85 gr (including a battery)

Note :

*a) evaporative cooling effect emerge from a cloud is not considered

*b) Contamination due to rainy conditions is not regarded

*c) Under optimal conditions of GPS reception: PDOP=1

*d) Condition under moderate wind <5 m/s are not calculated.

(Source : https://archive.meisei.co.jp/english/products/rs-11g-e.pdf)

3.1.6. Himawari satellite

Himawari-8 is a satellite launched on 7 October 2014 and operated within seven years. Himawari-8 is equipped with advanced Himawari imagers (AHI) that have 16 observation bands that consist of three visible bands, three near infrared, and ten infrared bands). The specification of each band is described in table 3.7.

Himawari-8 satellite data in this study is used for verification of the cloud condition around BLR location. Himawari-8 satellites have three temporal and spatial resolutions of 0.5, 2, 2.5 minutes and 0.5, 1, and 2 km, respectively. For cloud indicator, the cloud albedo, data from visible band 03 of the Himawari-8 satellite are used. This spectral band has the highest resolution, which is 500m. Figure 3. 6 is the example of the cloud albedo data with a red rectangle in the BLR location.

Table 3.7. Specification of AHI Himawari-8 spectral bands

Himawari-8 / AHI				
Band		Wavelength (μm)	Spatial resolution (km)	Description
Visible	01	0.47	1	Vegetation, aerosol
	02	0.51	1	Vegetation, aerosol
	03	0.64	0.5	Vegetation, low clouds, fog
Near-Infrared	04	0.86	1	Vegetation, aerosol
	05	1.6	2	Cloud phase
	06	2.3	2	Particle size
Infrared	07	3.9	2	Low cloud, fog, forest fire
	08	6.2	2	Mid and upper level moisture
	09	6.9	2	Mid level moisture
	10	7.3	2	Mid and lower level moisture
	11	8.6	2	Cloud phase, SO_2
	12	9.6	2	Ozone content
	13	10.4	2	Cloud imagery, cloud top information
	14	11.2	2	Cloud imagery, sea surface temperature
	15	12.4	2	Cloud imagery, sea surface temperature
	16	13.3	2	Cloud top height

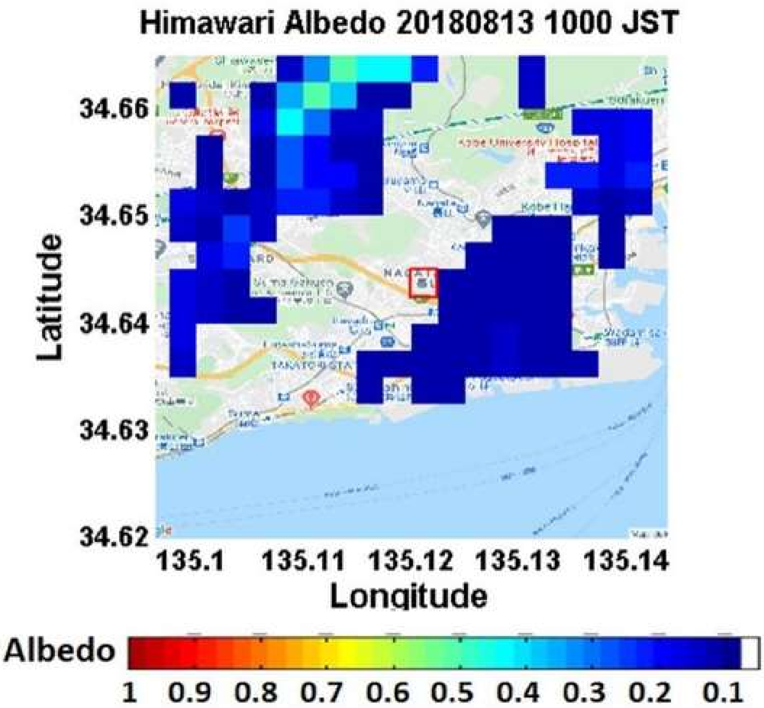

Figure 3. 6. Cloud albedo from Himawari 8 satellite

3.2. Method

3.2.1. Pseudo vorticity

The pseudo vorticity method is used in this study to calculate vorticity. The nearest two mesh grid Doppler velocity in the azimuth direction will be used in this study (Figure 3.7). The different values of these two mesh grids will determine the vorticity feature of the airflow structure. Using the difference from two mesh grids of Doppler velocity data in the azimuth direction (V_3 and V_4), divided by the azimuth difference between the two mesh grids (Δx), we could calculate the vorticity as represented by Equation 3.5. Other variables such as α (azimuth resolution) and slant range (beamline range distance) are needed to calculate the Δx.

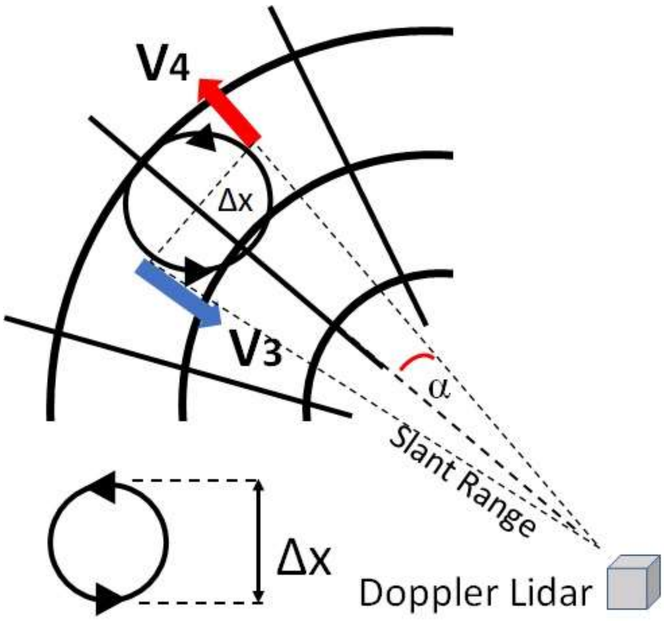

Figure 3.7. Pseudo vorticity illustration

$$\zeta = \frac{V_4 - V_3}{\Delta x} \qquad (3.5)$$

3.2.2. Convergence – divergence

Divergence and convergence usually represent a flow structure converging or expanding at one point. The calculation of divergence – convergence is referred from previous research by Katayama et al. (2015) utilizing Doppler velocity data. If the positive Doppler velocity value meets with the negative doppler velocity value from its nearest Doppler velocity along the beamline, we could estimate that airflow convergence occurs in this region (Figure 3.8). Meanwhile, airflow divergence occurs when the opposite direction of Doppler velocity is met. Using these principles, calculating the difference between those two values of the nearest Doppler velocity data along the beamline and divided by the distance of these two values, we could estimate divergence - convergence using Equation 3.6.

$$DIV \mid CONV = \frac{V_1 - V_2}{\Delta y} \qquad (3.6)$$

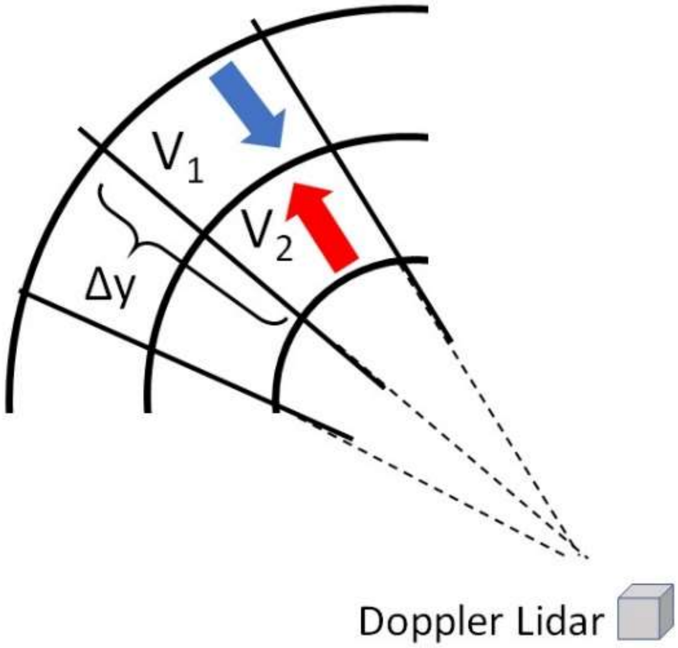

Figure 3.8. Convergence divergence illustration

3.2.3. Boundary layer height calculation

The depth of the boundary layer (BL) also plays an important role in cloud generation. BL height is calculated using SNR BLR based on Angevine et al. (1994) method. The first step of this method is to locate the peak value of the SNR. This procedure is conducted in time-series data of the center beam of the BLR that has already been filtered using outlier removal.

The next procedure is to compute the height using the median within a certain period (in this study, on each 24 s). The boundary layer height is then overlaid into the vertical velocity data of the BLR. Doing this will distinguish the boundary layer height from the free atmosphere layer.

3.2.4. Cloud image processing

In order to utilize the image data from the time lapse camera, we utilized image processing to quantify the information. An image analysis software is utilized to quantize this information. Digimizer is software often used in several research fields that need image analysis (Chenari and Mottaghian, 2020). This study uses Digimizer software (Figure 3.9a) to extract the information and calculate the pixel area from a cloud image retrieved by the camera. The term cloud pixel area represents the area of the individual cumulus cloud observed by the time lapse camera located at the BLR site. The calculated cloud pixel area from the start of appearance until it disappears is represented in the cloud pixel area time series (Figure 3.9b).

Adjustment is made for the image that will be used in the analysis. The original image from the camera is 1980 x 1080 pixels. However, since the coverage of the BLR beam is only 14°, the image pixel needs to be limited. The calculation of how much limit of the image pixel is conducted by noticing the camera focal length, the camera view angle, and the zenith angle of BLR. A 500 x 500 pixel is used as a threshold to limit (crop) the image.

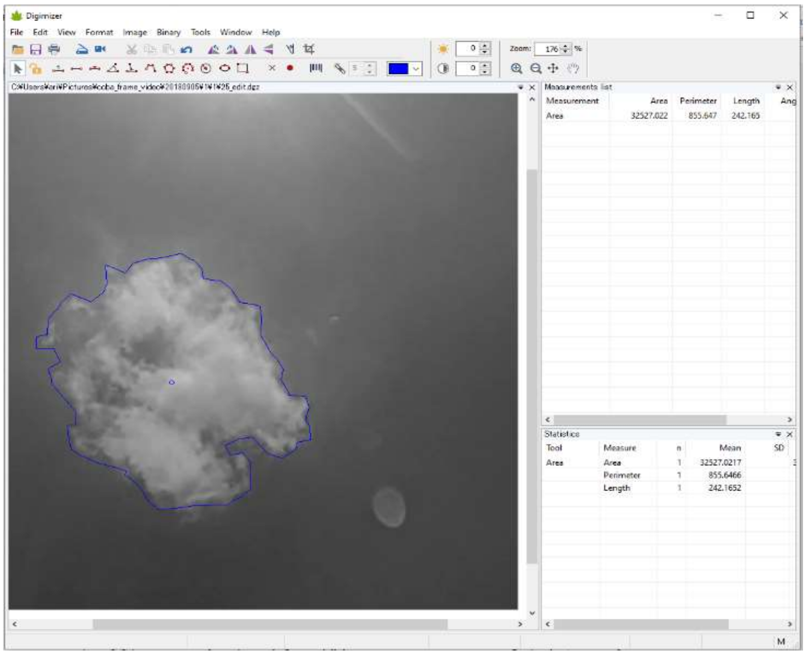

(a)

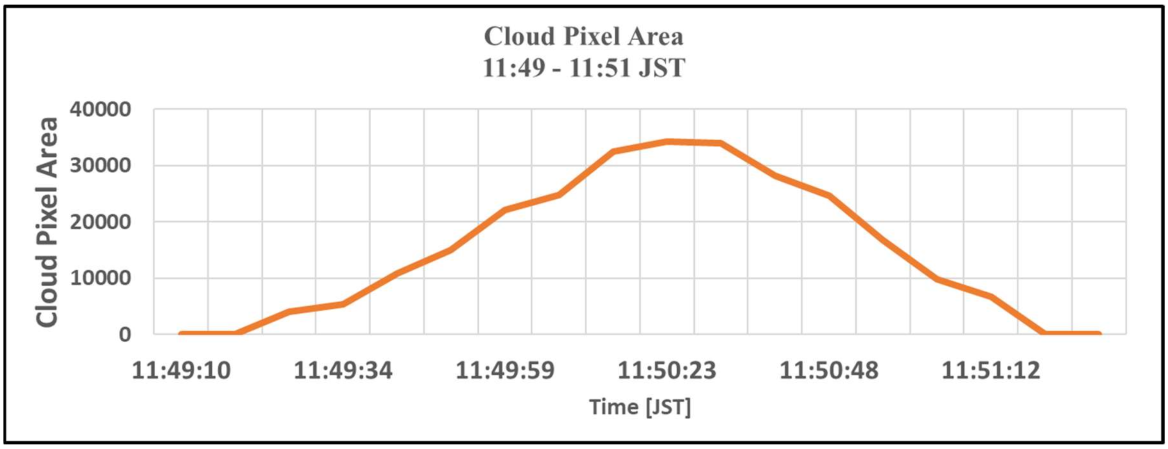

(b)

Figure 3.9. Cloud pixel area, a) Digimizer software, b) Time series

In order to estimate the cloud height of this newly developed cloud, a stereo photogrammetry method (Misumi et al., 2017) is used. The method uses two images from two time-lapse cameras located in the Doppler lidar site. The schematic of this method is depicted in Figure 3.10 .

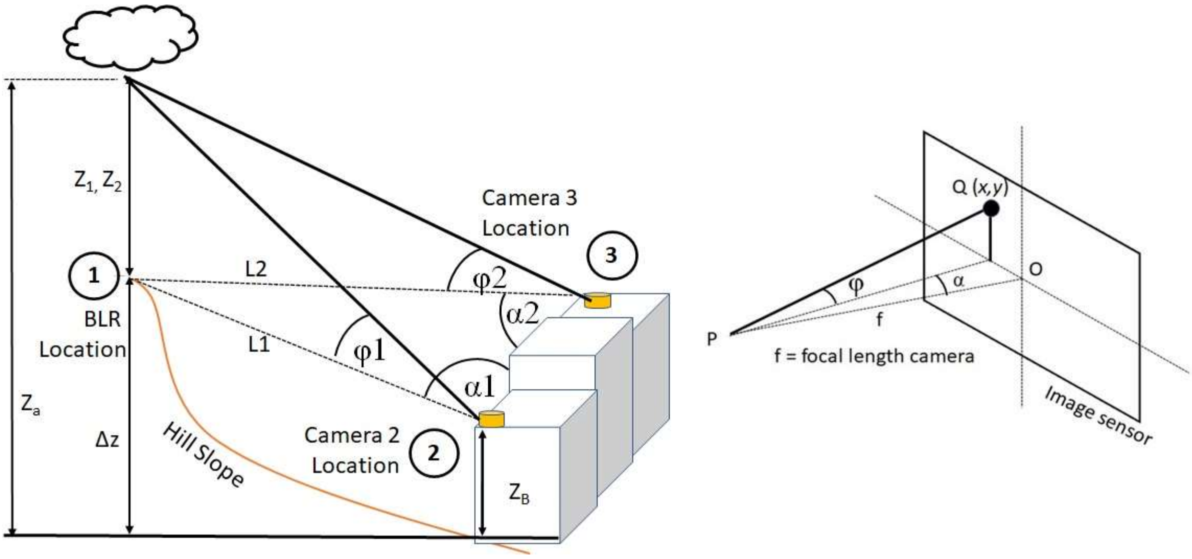

Figure 3.10. Stereophotogrammetry

In this method, the first step is to find the cloud location in pixel coordinate from both images. The time reference to locate the cloud uses the timestamp from the cloud pixel area. However, there is a slight difference in time between these two cameras on location B. Using NICT time as a reference, the time difference between these two cameras could be retrieved as follows; 4.5 s and 2.5 s. The timestamp of each camera always leads ahead of the NICT time reference. This information is used as a reference for selecting images for the cloud pixel coordinate location.

After finding each image cloud pixel coordinate (x,y), the second step calculates cloud estimated height (Za) using equations 3.7 through 3.11. Z_B is the height of the Doppler lidar building where the location of two time lapse camera take place. Δz is the height of the BLR calculated from the mean sea level, φ_1 and φ_2 are the elevation angle, α_1 and α_2 are the azimuth angle, and L_1 and L_2 are the distance between time lapse camera and BLR. In previous research conducted by Misumi et al. (2018), the variable of L_1 and

L_2 are estimated values using the calculation of α and distance between the two cameras. However, in this study, the focus of the cloud is only above the BLR location. Furthermore, it is assumed that the L_1 and L_2 did not change significantly. In this study, L_1 and L_2 values are fixed based on the real distance value instead of an estimated value.

$$\tan\alpha = \frac{x}{f} \tag{3.7}$$

$$\tan\varphi = \left(\frac{y}{f}\right)\cos\alpha \tag{3.8}$$

$$Z_1 = L_1 \tan\varphi_1 \tag{3.9}$$

$$Z_2 = L_2 \tan\varphi_2 \tag{3.10}$$

$$Z_a = 0.5(Z_1 + Z_2 + \Delta Z) + Z_A \tag{3.11}$$

In order to examine the accuracy of this method, a comparison was conducted using a static object (Takatorisancho hill). This object is located 3.52 km northwest of the BLR location. The calculated height of this hill is 307 m. Meanwhile, the original height of this hill is 329 m. The discrepancy between the original and estimated height is 22 m, which is still sufficient compared with the vertical height sampling of BLR of 30 m. However, in a non-static object such as a cloud, the discrepancy could change and increase due to the changing position of the object (Misumi et al., 2017).

3.2.5. Doppler Beam Swinging

DBS (Doppler Beam Swinging) method is used to estimate the wind vector by utilizing three (or more) beam directions from wind profiler data (Fukao and Hamazu, 2014). In this study, three non-coplanar beam direction is used. Table 3.8 showed the setting of the BLR during the observation. The observation sequence is as follows, beam

1-beam 2-beam 1- beam 3. The repeated beam 1 is used for the calculation of the vertical velocity.

Table 3.8. BLR beam setting

No beam	Azimuth (α), Zenith (θ)	Direction
1	0° , 0°	Vertical direction
2	0° , 14°	North direction
3	90° , 14°	East direction

In order to determine the horizontal component in each azimuth, equation 3.12 is used:

$$V_H(\phi) = \frac{V_R(\theta,\phi) - w\cos}{\sin\theta} \tag{3.12}$$

V_R is the radial velocity, w is the vertical velocity, and V_H is the horizontal velocity

Before utilizing the DBS method to observe the horizontal wind condition, a comparison test is conducted. A comparison test is conducted to reassure that the DBS method has a reliable result in representing the horizontal wind condition. Radiosonde data from the nearest launch site is utilized as a comparison. The launch location is on top of the building of the Kansai supermarket. The distance between the launch location and BLR is approximately 2 km northeast. The radiosonde campaign was conducted in 2018 and 2019. However, in this study, only the dataset on 18 and 19 August 2019 is used for comparison. Figure 3.11 compares zonal and meridional wind from BLR and radiosonde data. Both comparisons showed a coefficient correlation of more than 0.5, which shows a good correlation.

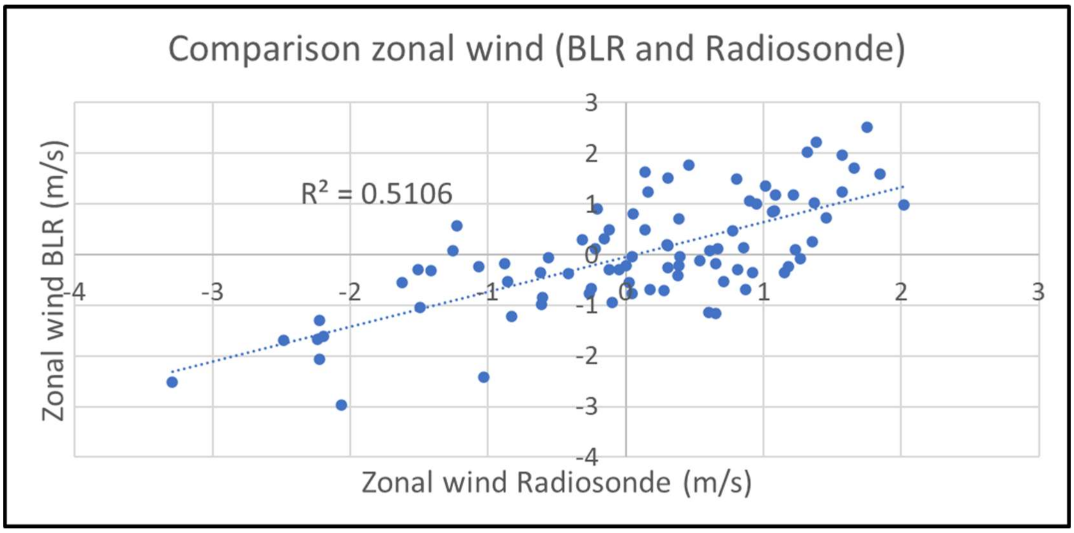

(a)

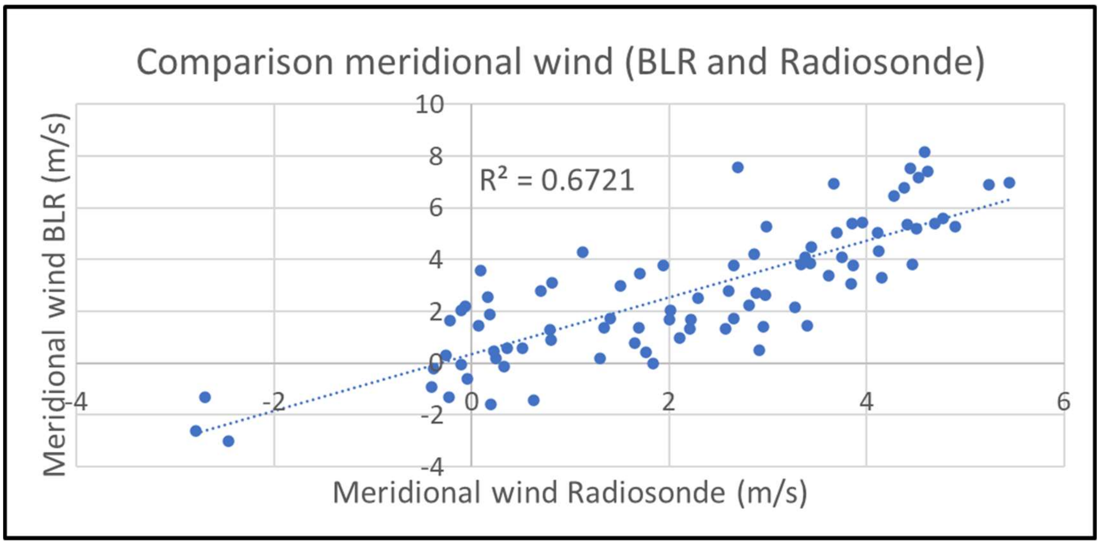

(b)

Figure 3.11. Comparison between BLR and radiosonde, a) Zonal wind, b) Meridional wind.

3.2.6. Radial velocity variance

Variance calculation from Doppler velocity is used to strengthen the analysis result on the condition of the updraft location. The variance of the Doppler velocity value is caused by the velocity fluctuation of the aerosol particle. There are many possible reasons why the velocity fluctuates. One possible reason is the updraft existence. Variance is calculated from the two-dimension (2D) Doppler velocity data series. Moving window variance with the Welford approach is used in this study to calculate the variance over a certain window grid across neighboring Doppler velocity data (Eq. 3.13). A comparison of the variance result with the divergence-convergence result is conducted to observe the relation between them.

$$S_n = S_{(n-1)} + \left(\frac{n-1}{n}\right)\left(x_n - \bar{x}_{(n-1)}\right)^2 \qquad (3.13)$$

3.2.7. CAPE and CIN

CAPE (Convective Available Potential Energy) and CIN (Convective Inhibition) are calculated from radiosonde data. The purpose of this calculation is to analyze the atmospheric instability condition. In this study, self-calculation is conducted by referring to a script program file from George H. Bryan (NCAR, USA). CAPE calculation is Eq. 3.14, meanwhile, CIN is using Eq. 3.15.

$$\text{CAPE} = \text{PSUM}\ (\ \text{Dz} \times (\ \text{TP} - \text{TE}\ ) / \text{TE}\ ) \qquad (3.\ 14)$$

$$\text{CIN} = \text{NSUM}\ (\ \text{Dz} \times (\ \text{TP} - \text{TE}\ ) / \text{TE}\ ) \qquad (3.\ 15)$$

Where PSUM is the sum within the sounding area from LFC (Level of Free Convection) to EL (equilibrium level) where (TP - TE) is greater than zero, NSUM is the sum within sounding area from top of the mixed layer to LFC where (TP - TE) is less than zero, Dz is the increment depth, TP is the temperature of a parcel from the lowest height, raised dry adiabatically to the LCL and moist adiabatically thereafter, and TE is the environment temperature.

The comparison is conducted by using a reference of the CAPE and CIN calculation from Wyoming University (http://weather.uwyo.edu/upperair/sounding.html). The comparison uses radiosonde launch data in Shionomisaki, Wakayama prefecture (ID station 47778). Figure 3.12 shows the Skew T diagram comparison in 16 August 2019 from the Wyoming calculation and self-calculation. Twenty two radiosonde data in August 2019 is used for the CAPE and CIN comparison. Figure 3.13 show the comparison using the coefficient correlation of CAPE and CIN. The coefficient correlation showed a value of strong correlation (larger than 0.7) that shows the value of self-calculation can be reliable to use for the analysis.

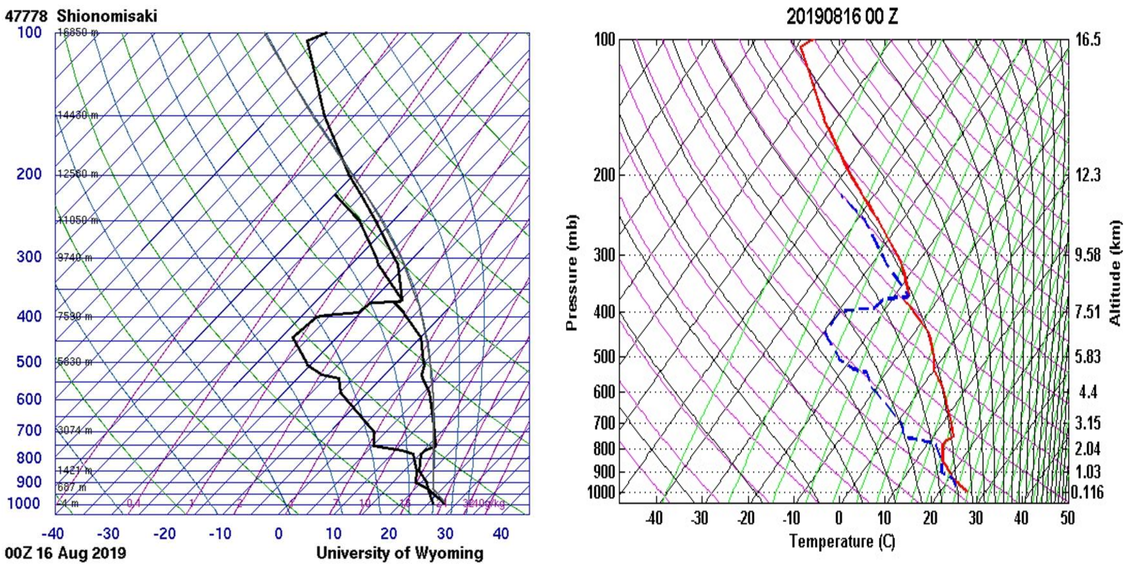

Figure 3.12. Skew T diagram of radiosonde using self calculation and from Wyoming website.

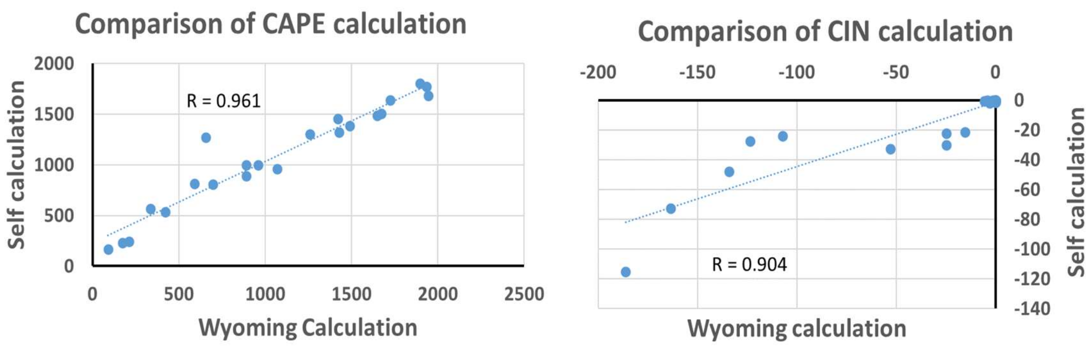

Figure 3.13. Comparison of the CAPE and CIN calculation between Wyoming calculation and self calculation.

3.3. Target area

The observation is taken place in the Kobe urban area, Japan. The observation took place during the summer season (from July until September) in 2018 and 2020. We only focused on the daytime from 5 am until 4 pm JST. The reason is that the probability of thermal occurrence is high only during those periods. Each instrument is located in a different area, depicted in Figure 3.14. The location of Kobe city is surrounded by sea (Osaka bay) in the east-south direction and mountain (Mount Rokko) in the north-west direction. Numerous water vapor sources from the south with obstruction in the north make a higher probability of cloud initiation in this location.

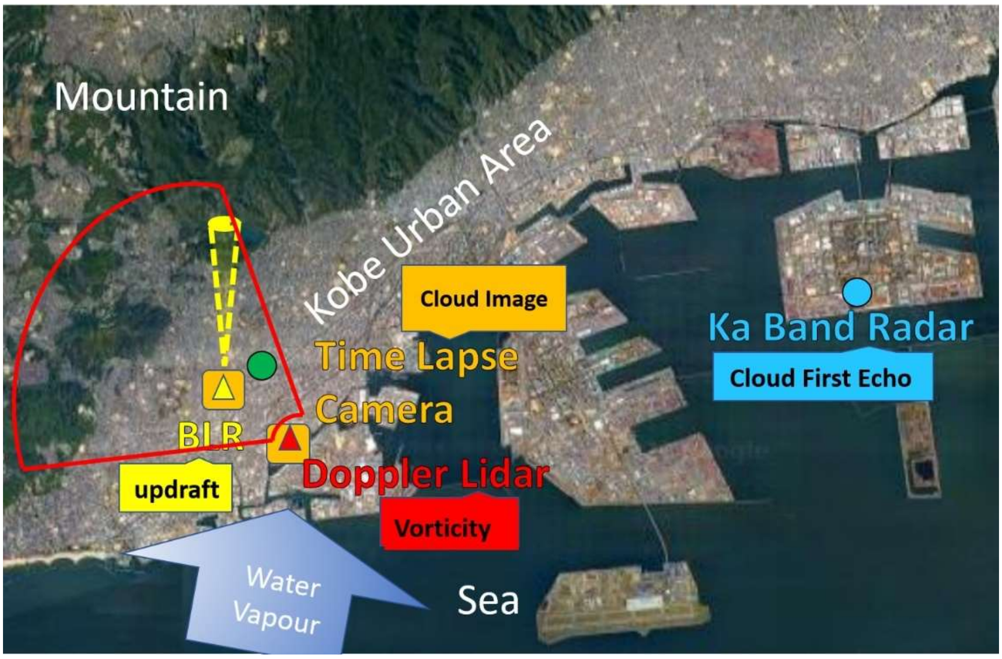

Figure 3.14. Location of each instruments

Several radiosonde launches are also conducted in 2 km southeast direction from BLR. The radiosonde launch intends to collect meteorological data during the observation.

3.4. CReSS

CReSS (Cloud Resolving Storm Simulator) model is used in this study to substitute the atmospheric profile data that could not be obtained due to the lack of radiosonde data. CReSS is intended to simulate the high impact weather system (heavy rainfall, typhoon, baiu front, etc). CReSS can simulate the weather condition in a large domain but with a very fine grid system. This performance will be able to clarify a more detailed structure of the weather in a large domain area. CReSS can perform high-resolution simulations in both horizontal and vertical directions. This study utilizes the CReSS model to obtain the atmospheric profile needed to calculate the CAPE and CIN. The setting of the CReSS model is listed in table 3.9 below.

Table 3.9. CReSS setting

Parameter	Setting
Resolution	Horizontal : 600 meter Vertical : 150 meter (average)
Numbers of grid	Horizontal : 300 x 300 Vertical : 61 layer
Height	Lowest level : 58 meter Top level : 8.638 meter
Calculation time	09 – 16 JST, 11 September 2018 and 18 August 2019
Initial and Boundary data	JMA-MSM

From several CReSS products, three parameters (temperature, pressure, and dew point temperature profile) are derived for CAPE and CIN calculation. The sum of base state pressure (pb) and pressure perturbation (pp) from CReSS is used to calculate pressure (prs). The sum of base state potential temperature (ptb) and potential temperature perturbation (ptp) are used to calculate the potential temperature (pt). Temperature (tt) is calculated using Equation 3.16 based on information from potential temperature, pressure, gas constant of air (R) and specific heat (c_p). Meanwhile, dew point temperature (td) is estimated from the relation between vapor pressure (e) and saturation vapor pressure (e_s) (equation 3.17 – 3.18). The water vapor mixing ratio (qv) calculates the vapor pressure. Equation 3.19 estimates the dew point temperature using actual vapor pressure instead of saturation vapor pressure from equation 3.18. Variable t_0 is 273.15 K, L is the latent heat of vaporization (2.5 x 10^6 J/Kg), and R_v is the gas constant for dry air (461.5 J/Kg. K).

$$tt = \frac{pt}{(1000/prs)^{(R/c_p)}} \qquad (3.16)$$

$$e = \frac{qv\ x\ prs}{0.622 - qv} \qquad (3.17)$$

$$e_s = e_0 \exp\left[\frac{L}{R_v}\left(\frac{1}{t_0} - \frac{1}{tt}\right)\right] \qquad (3.18)$$

$$td = \left[\frac{1}{t_0} - \frac{R_v}{L}\ln\left(\frac{e}{e_0}\right)\right]^{-1} \qquad (3.19)$$

In order to test the response of the vertical profile of the CReSS model, a comparison between CReSS and radiosonde is conducted. Root mean square error (RMSE) and MAE (Mean Average Error) are used to investigate the performance of numerical model performance (Bilal et al., 2016; Chai and Draxler, 2014). RMSE and MAE equations are described in Equations 3.20 and 3.21. Table 3.10 shows the comparison of the RMSE between CReSS and Radiosonde.

$$RMSE = \sqrt{\frac{1}{n}\sum_{i=1}^{n} e_i^2} \qquad (3.20)$$

$$MAE = \frac{1}{n}\sum_{i=1}^{n} |e_i| \qquad (3.21)$$

Table 3.10. CReSS and radiosonde comparison

	RMSE			MAE		
Time	Temperature	Dew point	Pressure	Temperature	Dew point	Pressure
09:00	0.337	2.319	0.245	0.261	1.978	0.188
10:00	0.694	2.399	0.248	0.568	1.954	0.177
11:00	0.868	2.360	0.178	0.695	1.827	0.140
12:00	1.141	2.662	0.177	0.962	2.141	0.135
13:00	2.009	4.061	0.205	1.793	3.355	0.151
14:00	2.833	4.387	0.150	2.486	3.673	0.107
15:00	3.470	4.237	0.361	2.622	3.096	0.235
16:00	1.397	3.783	0.139	1.084	3.150	0.110

The RMSE and MAE results showed that two parameters (temperature and pressure) have a good comparison between CReSS simulation and radiosonde measurement. Based on this comparison, we use the CReSS model data for the CAPE and CIN calculation in periods where radiosonde data is unavailable.

Chapter 4. Wavelet : theoretical background

4.1. Continuous wavelet transform (CWT)

A wavelet is a tool that can be used to examine non-stationary signal characteristics at various frequencies within a time series of data (Daubechies, 1990). Using the wavelet, we can obtain the periodicity of the increased amplitude (wavenumber) when the increased amplitude occurs and how long (how much time) thus the increased amplitude occurs. Continuous wavelet transform (CWT) is one wavelet type applied as a bandpass filter towards a time series data. The wavelet function will be stretched in time with the varied scale of the wavelet function.

This study describes how to utilize wavelets in the observation data, choose the appropriate mother wavelet, and other wavelet applications to observe the coherence between two time series data. The wavelet transforms absolute squared value is the wavelet power spectrum that expresses the correlation information between the wavelet function and the time series data. CWT applications are based on Torrence and Campo (1998) algorithm expressed as follows.

$$W_n(s) = \sum_{n'=0}^{N-1} X_{n'} \Psi^* \left[\frac{(n'-n)\delta t}{s}\right] \tag{4.1}$$

$$s_j = s_0 2^{j\delta j} \tag{4.2}$$

$$j = \left(\log_2(N\delta t/s_0)\right)/\delta j \tag{4.3}$$

where $X_{n'}$ is the data of vertical wind velocity time series, N is the length of the data, Ψ^* is the complex conjugate of the wavelet function, δt is the sampling interval, and s is the wavelet scale. It is necessary to define the scale and determine the smallest (s_0) and largest (s_j) resolvable values of the scale, the number of scales used (j), and also its interval (δj).

Eq. 4.2 is used to determine the scale with a convenient scale as a power fraction of two. Normalization is needed to ensure that the wavelet transform can be comparable to each other scale or other wavelet transforms. Normalization is intended to create a unit of energy for the wavelet transform.

4.2. Properties of CWT

CWT will produce an error at the edge at the start and the end of the wavelet power spectrum. Wavelet does not completely localize in time. That is why it needs a boundary to separate which data area consists of error. COI (Cone of Influence) region is applied by padding the end of the time series with zeroes before repeating the wavelet transform cycle. COI separates the wavelet power spectrum from unrelated values due to the decrease in wavelet power.

A significant level is defined as the condition where the peak of the wavelet power spectrum is significantly above the average (background) power spectrum. A certain percentage of confidence defines the significance. For example, if the significance is at a 5% level, it is equivalent to a 95% confidence level. The 95% confidence level is considered the best fit in this study and was later used for the wavelet calculation.

Smoothing could be performed toward the wavelet power spectrum. Smoothing is intended to observe the power spectrum average variance over time or a scale period. The average variance could become important information about the general condition of the object target.

The Mother wavelet is the basis wavelet function that is scaled and shifted into the projected time series data in the wavelet transform. These properties allow the wavelet to capture a local structure in space and time. Since different mother wavelets have their own interpretation of the localized structure, choosing the correct mother wavelet according to the desired target is essential.

4.3. Mother wavelet : how to choose the correct type

In order to determine which wavelet function that appropriate, four criteria need to be considered :

a) Complex or real. A complex wavelet function returns amplitude and phase information, making it better suited to capture oscillatory phenomena. Meanwhile, real wavelet function produces just one component, which can be utilized to separate peaks or discontinuities. Fig 4.1. is an example of the difference between complex and real parts of the wavelet function.

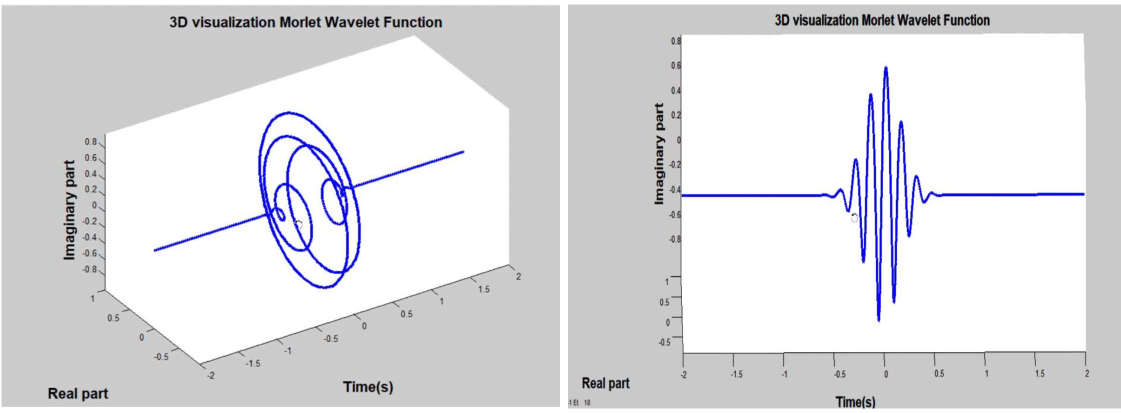

a) b)

Figure 4.1. Example of the difference between complex and real part in morlet wavelet function, a) Complex, b) Real part

b) Orthogonal or non-orthogonal. In Orthogonal, at each scale, the number of convolutions is proportional to the width of the wavelet basis. Unfortunately, a periodic shift in the time series results in a distinct wavelet spectrum, which is problematic for time series analysis. Meanwhile, non-orthogonal is highly redundant at large scales, with the wavelet spectrum at adjacent times highly correlated. The non-orthogonal transform proves useful when smooth, continuous fluctuations in wavelet amplitude are expected.

c) Shape. The wavelet function should represent the characteristics of the time series.

d) Width. A narrow (in time) function has excellent time resolution but poor frequency resolution, whereas a broad (in time) function has poor time resolution but high frequency resolution.

There are several types of the mother wavelet. This study only showed three types and their properties in table 4.1.

Table 4.1. Example of mother wavelet function

Type	Morlet	Paul	Derivatives of Gaussian (DOG)
Shape	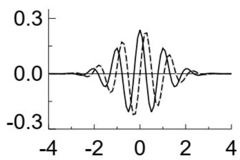	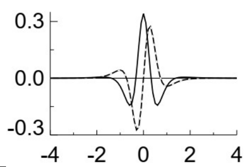	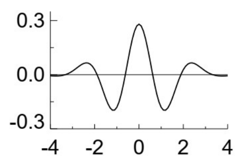
Factor for scale averaging	0.60	1.5	0.97
Fourier wavelength	$\frac{4\pi s}{\omega_0 + \sqrt{2+\omega_0^2}}$	$\frac{4\pi s}{2m+1}$	$\frac{2\pi s}{\sqrt{m+\frac{1}{2}}}$

4.4. Wavelet coherence

Previous research by Torrence et al. (1998) has shown wavelet coherence as an extension of the wavelet analysis. The wavelet coherence method is often used to find the relationship between two variables (Ng. Eric, and Chan, 2012). There are certain steps to execute the wavelet coherence. The first step is normalizing the two variables to overcome the different units. The next step is to calculate the wavelet power spectrum for each dataset, then calculate the cross wavelet using conjugation from these two wavelet power spectrums. Afterward, wavelet coherence level and phase coherence could be calculated using Eq. 4.4 and 4.5 are based on the wavelet power spectrum and cross wavelet result.

$$R_n^2(s) = \frac{\left[W_n^{xy}(s)\right]^2}{[W_n^x(s)]^2\left[W_n^y(s)\right]^2} \tag{4.4}$$

$$\phi = \tan^{-1}\frac{\text{imaginary}(W^{xy})}{\text{real}(W^{xy})} \tag{4.5}$$

$R^2{}_n$ is the wavelet coherence level. Meanwhile, ϕ is the phase coherence. W^x and W^y are the wavelet power spectrum of each variable, and W^{xy} is the cross wavelet between these two power spectrums. This process's algorithm is based on Grinsted et al. (2004), which has been modified. The result of the wavelet coherence is the level between 0 and 1, and the phase coherence is represented by radian. The mother wavelet type used in the wavelet coherence analysis depends on the target.

The phase coherence is calculated based on the significant value of R^2n outside the COI (cone of influence) at every wavelet time scale. The phase coherence result can be classified to simplify the relationship result. Four phased can be defined to simplify the analysis. Phase one is the in-phase coherence ($\Delta\phi = 0\pm\pi/4$), phase two is the anti-phase coherence ($\Delta\phi= \pi\pm\pi/4$), phase three is the lagging phase coherence ($\Delta\phi= \pi/2\pm\pi/4$), and phase four is the leading coherence ($\Delta\phi= -\pi/2\pm\pi/4$). Furthermore, the four-phase classification can be represented by color, for example, in-phase coherence (cyan), anti-phase coherence (blue), leading phase (yellow), and lagging phase (green). This modification intends to make it easier to analyze. An illustration of the phase classification is depicted in Fig 4.2.

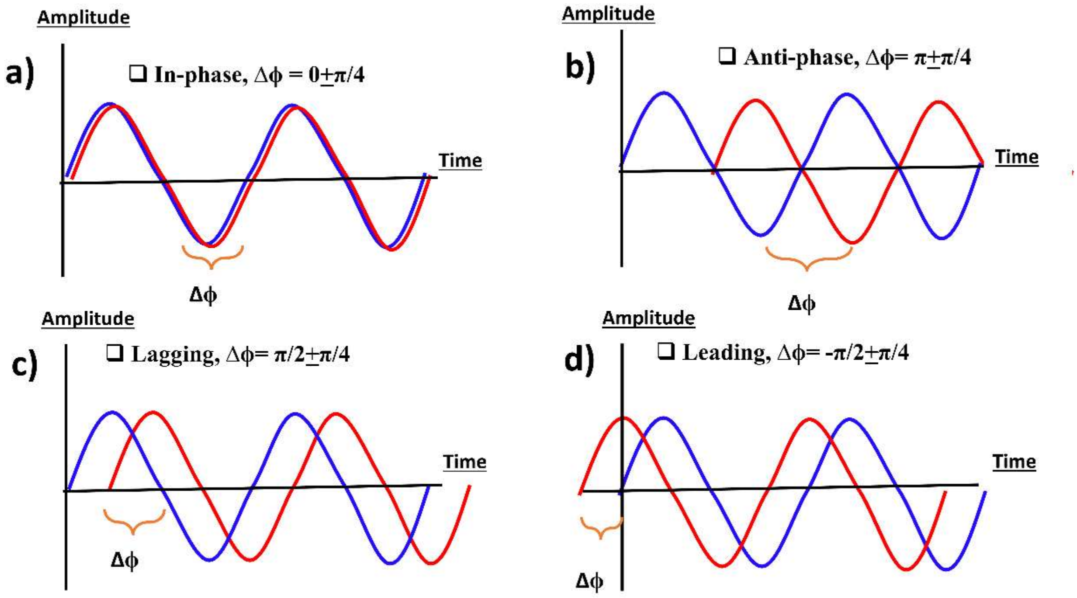

Figure 4.2. Illustration of the phase classification

Chapter 5. Thermal Plume and downdraft-updraft combination using wavelet approach

5.1. Thermal

The rising air column that moves from the surface into the atmosphere is called thermal. The shape of this thermal is similar to the smoke plume and can be expressed as a thermal plume. Thermal plumes extending into the boundary layer height have an important role in the mixed layer condition (Rio and Hourdin, 2008). The advanced BLR used in this study can capture the coherent structure of positive vertical air velocity representing the column of rising air or thermal. In this chapter, an example of thermal will be discussed more detail.

5.1.1. Thermal structure identification

Using BLR, the thermal plume structure in the form of the thermal plume can be identified in more detail. The high thermal plume was observed during the incoming large cumulus cloud on 11 September 2018, from 14:00 until 15:00 JST (Figure 5.1). A positive value represents the upward motion of the vertical air velocity (updraft). Meanwhile, the negative value represents the downward motion of the vertical air velocity (downdraft). There are several coherent updrafts from the BLR lower height (300m) until a certain height. This figure also shows very high thermal with a maximum updraft value of more than 5 m/s. This thermal elongated from 300 m until reaching up to 1.7 km height. Doppler lidar in the RHI scan also detects the coherent structure of the thermal plume at almost the same location as the BLR site (Figure 5.2).

By observing the height, the thermal surpasses the atmospheric boundary layer height estimated at around 1.2 - 1.5 km (Figure 5.3a). This estimated height is also supported by the variance of the vertical velocity profile (Figure 5.3b), where the minimum variance value in this period is located at 1.5 km height.

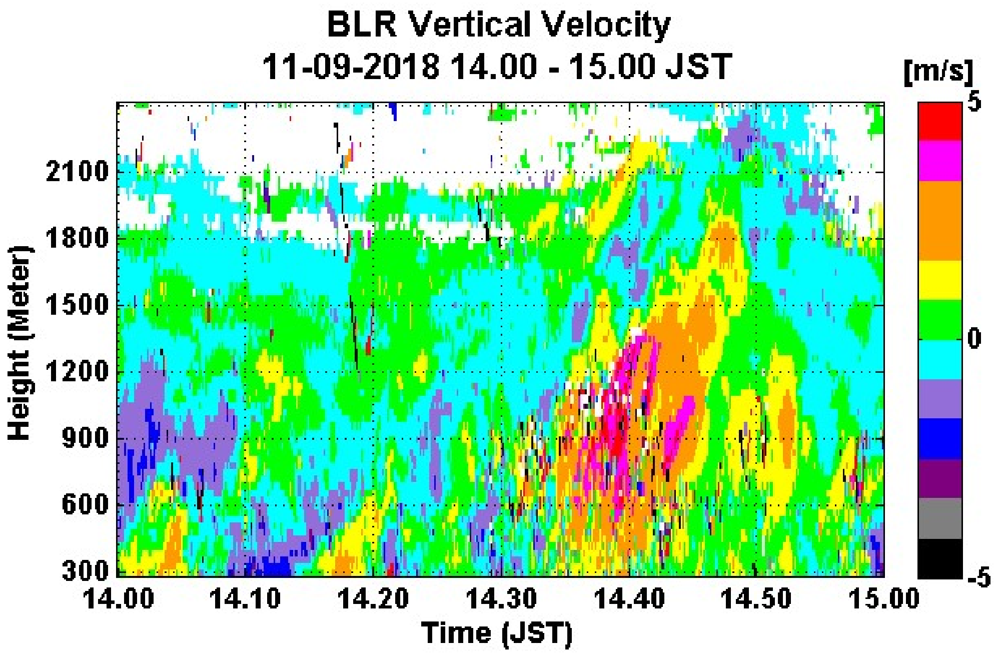

Figure 5.1. High thermal plume observed by BLR

.

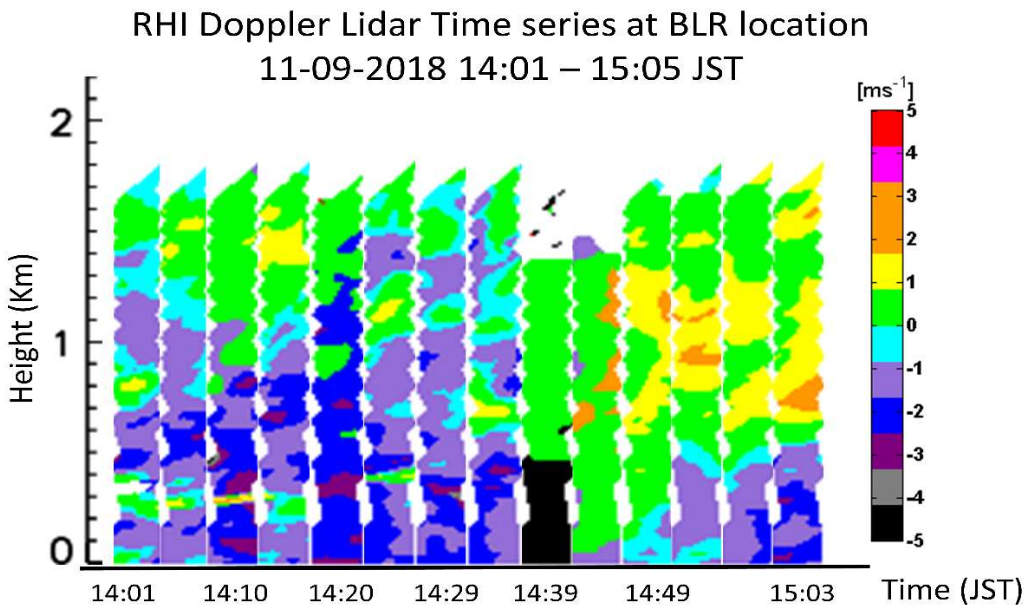

Figure 5.2. Doppler lidar observation using RHI scan at the direction of the BLR location. Black dashed line is the BLR location

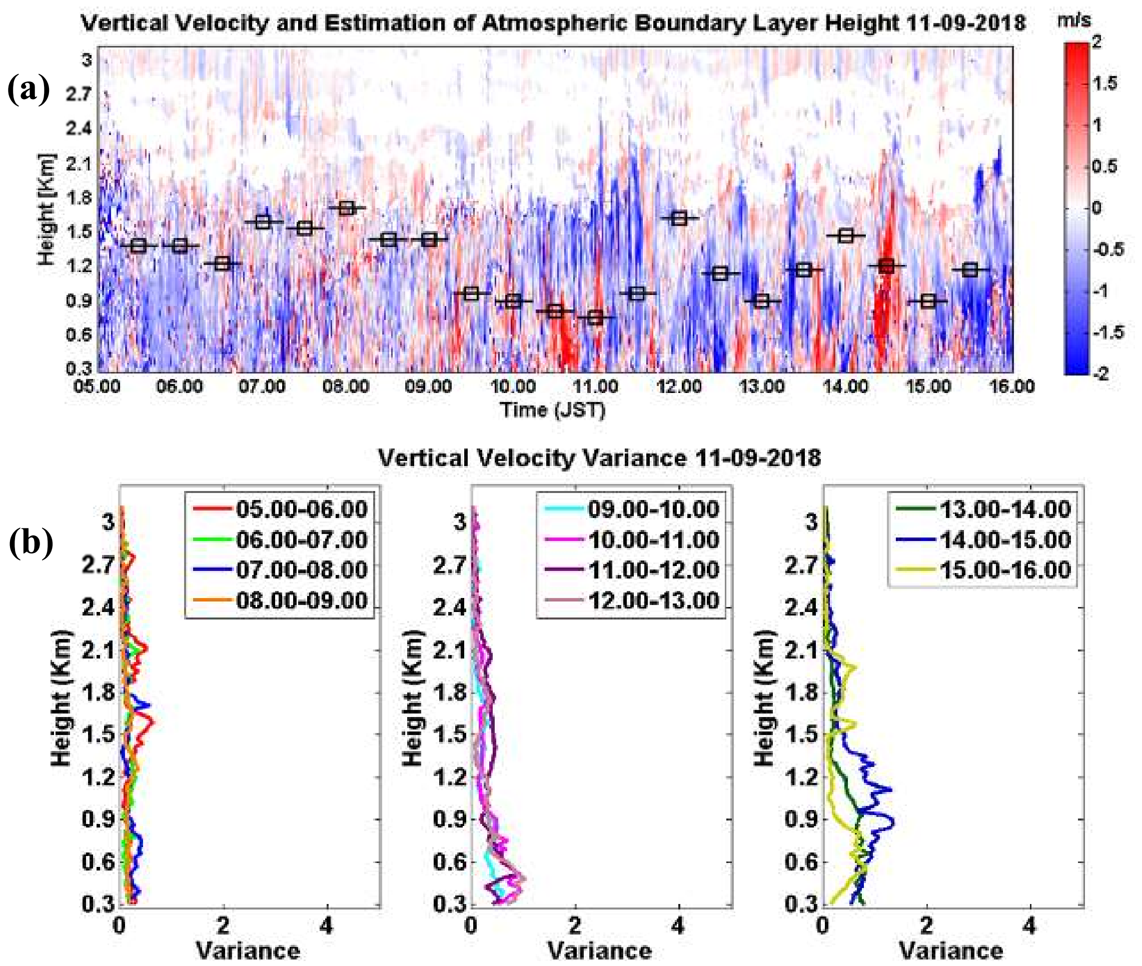

Figure 5.3. Boundary layer height estimation, a) Angevine method, b) Variance method.

However, the thermal did not penetrate or break the boundary layer. The echo power shows this from the BLR in Figure 5.4. The high thermal only pushes the boundary layer based on the strong echo power (105 – 110 dB), but it did not break its layer structure.

The meteorological factor is inspected in three days between 9 – 11 September 2018 from two nearest AMeDAS AWS. Figure 5.5 shows the temperature observation every 10 minutes, where from 14.00 – 15.00 JST is the highest temperature (27^0 C) on 11 September 2018 and two days before. Based on temperature observation, it is reasonable if the thermal activity is very active during this period.

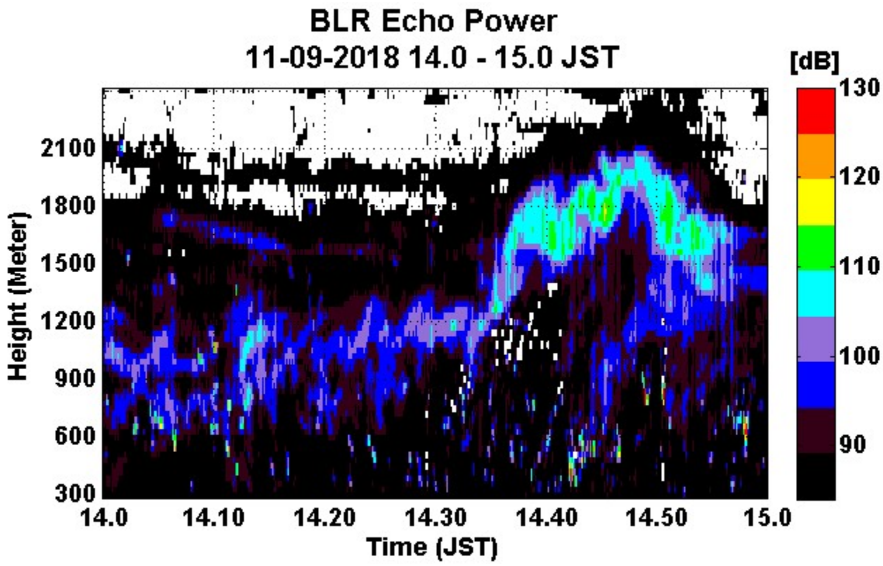

Figure 5.4. BLR echo power on September 11th 2018.

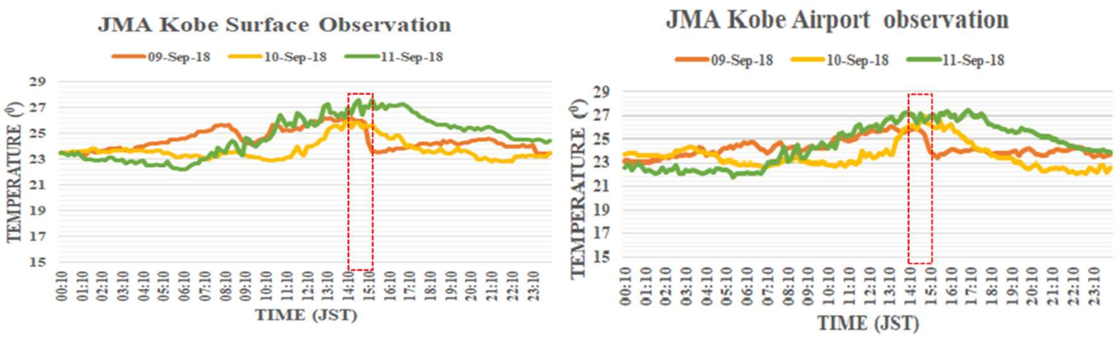

Figure 5.5. Temperature observation from nearest JMA AMeDAS in Kobe area.

5.1.2. Wavelet application toward the thermal data

The wavelet tool was then used to analyze the time series of BLR vertical velocity data height. Figure 5.6 shows the CWT result from the BLR time series at three heights (0.3, 0.6, and 0.9 km).

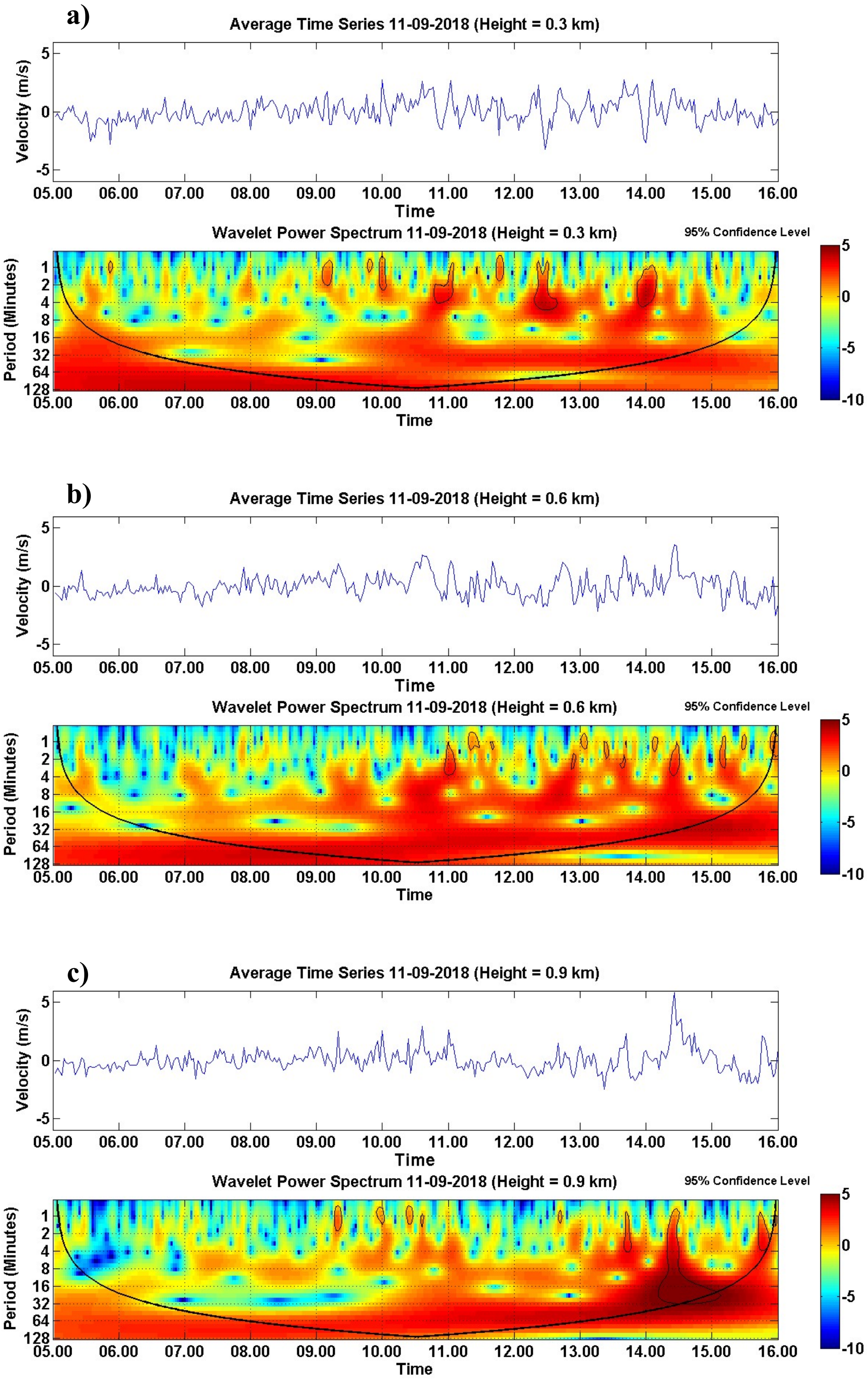

Figure 5.6. CWT results during high thermal plume at three different heights, a) 0.3 km, b) 0.6 km, c) 0.9 km. The upper figure on each height represents the vertical velocity time series. Meanwhile, the lower figure represents the wavelet power spectrum. 95% confidence value is marked in the thick black area.

In order to investigate the relationship between thermal and the incoming cloud, wavelet coherence was used. The time series of the cloud pixel area in Figure 5.7 showed a decreasing pattern from 14.28 until 14.34 JST. The increase is started after 14.34 JST – 14.36 JST that will be focused on for the transition phase. Unfortunately, the cloud becomes darker after 14.36 JST and gives a decreased pattern, although the cloud size is bigger and wider. The dataset from 14.34 JST – 14.36 JST is then calculated again using wavelet coherency (Figure 5.8), with the result summarized in table 5.1. From this table, from 0.3 km - 0.7 km the phase is the same as the previous WTC result (vertical velocity-Cloud albedo), but the phase is then variated. This result showed that the thermal is generated first before the cloud appears in the lower part.

Two WTC results showed a relationship between the high thermal and the convective cloud that passed above the BLR site. The lower part of the thermal is not affected by the cloud. Meanwhile, the upper part has the same pattern (in-phase) as the cloud existence. The upper part of the thermal seems to be affected by the cloud.

Time-lapse of the cloud image showed the cloud condition before, during, and after the high thermal occurrence (Figure 5.7). During maximum thermal value in 14.40 JST, the cloud image is become darker and shows some rotation in 14.44 JST. However, the high thermal did not support the incoming cloud to develop into precipitation clouds.

The cloud image can probably describe the effect of the upper thermal on the convective cloud after 14.36 JST (Figure 5.7). The cloud became darker in 14.40 JST, showed some rotation from the image sequence in 14.44 JST, and dissipated in 14.58 JST. This result showed that high thermal could affect the convective cloud condition, although it seems not to increase the convective activity of the cloud towards precipitation.

Figure 5.7. Time lapse image from the camera during high thermal.

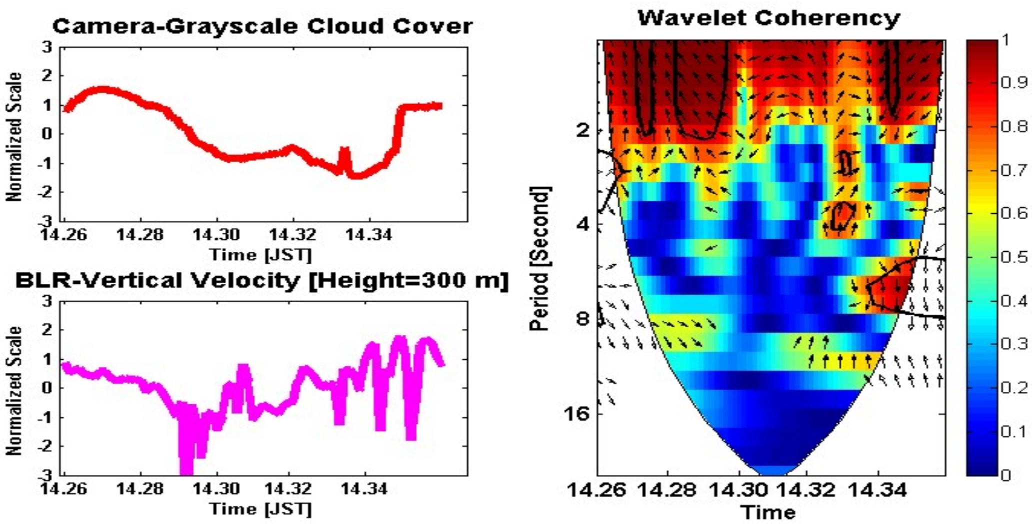

(a)

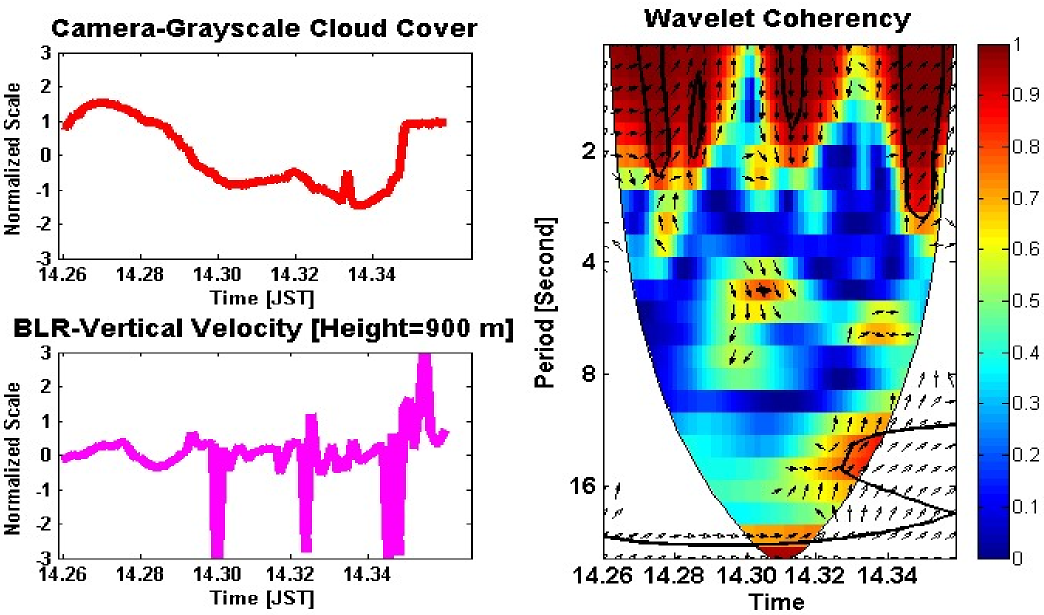

(b)

Figure 5.8. Wavelet coherence of thermal and incoming clouds on September 11th. 2018.

Table 5.1. Phase Angle (Vertical velocity - Grayscale cloud image)

Height (km)	Phase Angle	Height (km)	Phase Angle
0.3	Down	1.2	Right
0.4	Right	1.3	Down
0.5	Down	1.4	-
0.6	Down	1.5	Up
0.7	-	1.6	Right
0.8	Down	1.7	Down
0.9	Right	1.8	-
1.0	Up	1.9	Left
1.1	-	2.0	-

5.2. Downdraft-updraft combination

While updrafts are essential in transporting momentum, energy, and mass from the surface into the atmosphere, downdraft also has a unique role in the atmospheric process. The downdraft in the lower troposphere can increase the possibility of low-level convergence, enhancingnother convective development (Kain 2004). Downdraft also impacts the production of vertical vorticity at the ground level. A mesoscale simulation showed that the downward parcel changes its orientation under high pressure and produces vertical vorticity (Parker and Dahl, 2015). This vertical vorticity is important because a pair of positive and negative vertical vorticity in the cumulonimbus cloud can indicate a localized heavy rainfall occurrence (Nakakita et al., 2017).

A combination of the updraft - downdraft process could be generated by thermal forcing of solar heating, vertical wind shear, and its combination (Huang et al., 2020). Previous numerical simulation studies showed that updraft-downdraft generated by thermal have a temporal scale of less than a few minutes and a vertical scale of less than 100 m (Yamaguchi et al., 2019).

Another possible combination is the reversed downdraft-updraft process. In mesoscale phenomena, an additional downdraft-updraft circulation is essential for recharging and maintaining the cycle of energy, mass, and moisture budgets in the atmospheric boundary layer and developing new deep convective elements (Gray 2012). In microscale studies, this reversed downdraft-updraft process is still relatively unknown and difficult to observe due to the absence of a high-resolution instrument to observe this kind of combination.

This section aims to verify the existence of the microscale downdraft-updraft process within a certain height during the summer season during the observation in the urban area of Kobe, Japan. This section also discusses the analysis of microscale downdraft-updraft structure in different weather conditions (clear sky, cloudy, and convective).

This section uses CWT to distinguish the downdraft-updraft structure from the vertical wind velocity data. Main data from the advanced BLR is introduced to measure vertical wind velocity with high temporal and vertical resolution. CWT is utilized to determine the downdraft-updraft structure from vertical wind velocity observed by BLR. The wavelet transform is suitable for this analysis since it gives time-frequency information simultaneously for non-stationary time series data (Terradellas et al., 2001). Also, CWT is used because of its ability to extract particular characteristics (Wiebe et al., 2011), which in this case is the downdraft-updraft combination.

5.2.1. Downdraft-updraft structure identification

BLR data are taken from the observation period from 05:00 JST to 16:00 JST within nine selected days from July until October 2018. This period is chosen because the probability of convection is highest due to sunshine duration. The data are then classified into three weather conditions; clear sky, cloudy, and convective condition. In this study, convective is related to dry convective conditions depicted by several clouds existing without precipitation above the BLR during the study period.

A time-lapse camera and Himawari-8 satellite (Figure 5.9) are used to confirm these classifications conditions. A time-lapse camera that points upward and records cloud images every five seconds is placed in the BLR location. Cloud albedo from band 03 of the Himawari-8 satellite (Shang et al., 2017) is used to confirm the cloud condition above BLR. Horizontal wind near BLR location from Meso-Scale Model (MSM) is also used as a supporting variable of wind direction and speed. The weather classification and wind properties are shown in Table 5.2. Although wind shear is not considered in this study, environment wind was mostly southerly or southwesterly from Table 5.2.

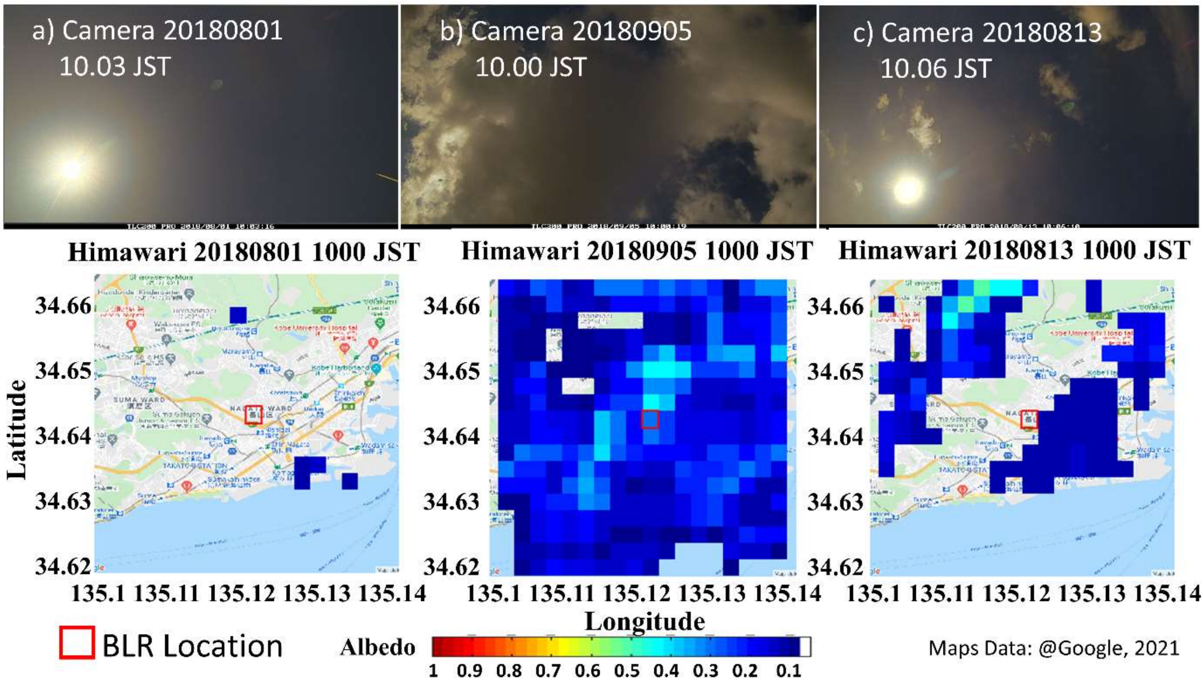

Figure 5.9. Example of three weather classification based on time-lapse camera and Himawari albedo. The classified results are (a) clear sky, (b) cloudy, and (c) convective conditions. The upper panels show the image from a time-lapse camera, and the lower panels show the albedo from Himawari-8. Red boxes represent the area where BLR is located.

The wavelet is calculated in the unit of minutes. The δt is achieved by calculating the amount of BLR data in one minute and dividing it by how many minutes in 11 hours (05:00 – 16:00 JST). The calculated δt is 0.0111. Then, using Eqs. 4.2 and 4.3 (from section 4.1) resulted in the s_0 and s_j values of 0.0444 and 46. The number of wavelet scales used is 41 scales. The scale period is calculated from the wavelet scale multiplied by Fourier factors that depend on the type of mother wavelet used (Torrence and Campo, 1998). The smallest scale period used is 0.25 min because it needs a minimum of two data to capture the downdraft-updraft combination.

Table 5.2. Classification of weather conditions and wind properties from MSM

Date	Classification	MSM							
		06 JST		09 JST		12 JST		15 JST	
		Dir	Spd	Dir	Spd	Dir	Spd	Dir	Spd
20180718	Convective	SSW	0.83	SSE	0.34	SE	0.55	WSW	0.64
20180719	Clear sky	E	0.63	ESE	0.75	ESE	0.41	SE	1.44
20180723	Convective	E	1.34	S	0.67	SSW	1.00	S	1.88
20180801	Clear sky	SSW	1.43	SSE	1.59	WSW	1.88	SW	2.44
20180804	Clear sky	E	2.07	W	0.46	SSE	1.14	S	1.15
20180813	Convective	ESE	1.31	E	1.20	SW	1.41	SW	1.97
20180830	Cloudy	W	1.43	WSW	1.53	WSW	1.97	W	2.58
20180905	Cloudy	SSE	1.4	SSW	2.26	SW	2.65	SW	2.3
20181013	Cloudy	SW	2.6	SW	1.1	WSW	1.2	S	0.5
Dir = wind direction Spd = wind speed (m/s) Height level = 1000 hPa									

Calculating a significant wavelet power spectrum with values above the background spectrum is needed to distinguish the physical feature of the real target (Torrence and Campo, 1998). The most significant value is then overlaid on the wavelet power spectrum in the form of a marked black region. Quality control is conducted by checking the significant value of the wavelet power spectrum and comparing them with the downdraft-updraft time series to verify that only the downdraft-updraft signature is collected.

Another constraint that needs to be considered is the missing data from BLR product. Wavelet is unable to calculate missing data or non-number values. Meanwhile, in the BLR observation, it is common to have an increased number of missing data throughout the height. Due to that reason, the wavelet calculation is only focused on the range height from 300 m to 1500 m. Nearest-neighbor interpolation is also used to handle the rest of the missing data that still exist.

5.2.2. Characteristic of downdraft-updraft combination

Figure 5.10 shows an example of July 23, 2018 data from 09:00 to 10:00 am JST. Figure 5.10b showed two significant updrafts; the first was at 09:17 JST and the second was at 09:25 JST, where the first updraft was not as strong as the second. Between these two updrafts, a strong downdraft occurred, lasting approximately 5 min at the height of 400 – 700 m. The second updraft seemed to push the observed stable layer above the enhanced echo power (Figures 5.10a and 5.10b).

A combination of the downdraft and the second updraft (downdraft-updraft) was observed below a height of 1100 m. The changing value of this downdraft-updraft combination started from a height of 500 m. Figure 5.10b shows this fine structure in a high temporal and vertical aspect, revealing the advanced BLR performance. The coherent structure of the second updraft is not affected by the horizontal wind at the surface (Figure 5.10c), which is likely due to the weak horizontal wind during that period.

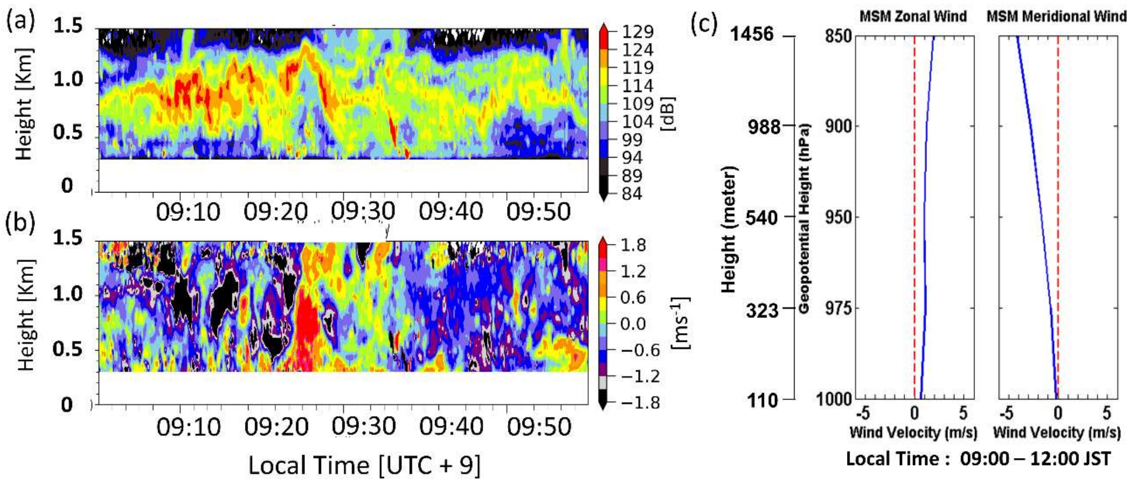

Figure 5.10. The time-height plot of (a) echo power and (b) vertical wind velocity measured by the BLR from 09:00 to 10:00 JST on 23 July 2018. (c) Vertical profile of MSM wind velocity during 09:00-12:00 JST on 23 July 2018. A positive value in vertical wind velocity represents updraft, while a negative value represents downdraft. The lowest height of echo power and that of vertical wind velocity are 300 m.

The wavelet method was applied to determine this type of downdraft-updraft pattern. The wavelet method is applied to the vertical wind velocity, and two main tasks need to be considered. The first task is to determine a method for distinguishing this downdraft-updraft pattern from other fluctuation patterns. The second task is to determine the characteristics of this structure under different conditions.

The first task is to use the wavelet approach to distinguish the downdraft-updraft pattern. The main important factor in distinguishing this pattern is the mother wavelet. There are various kinds of mother wavelet types, as explained in section 4.3. In this section, three different types of mother wavelets (Morlet wavelet, Paul wavelet, Mexican hat wavelet) were utilized via 1-dimensional CWT (CWT-1D) and applied to data on Figure 5.10b only from heights 500-1100 m, with the result is shown in Figure 5.11.

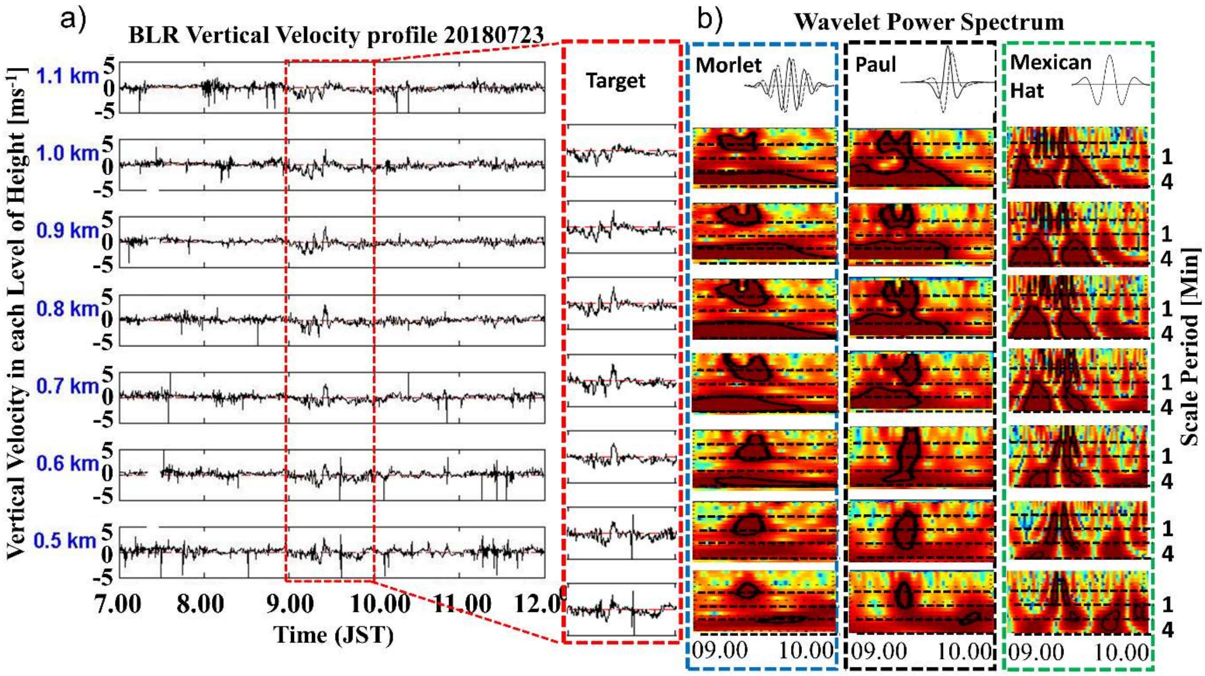

Figure 5.11. Comparison of the wavelet results using different mother wavelets. (a) Time series of vertical wind velocity. Red boxes show the target downdraft-updraft signal. (b) Wavelet results from each height of the target signal with different mother wavelets. See text for details of the mother wavelets.

The downdraft-updraft target is marked in the red dashed box. The wavelet power spectrum results using the Morlet wavelet, Paul wavelet, and Mexican hat wavelet are marked in blue, black, and green dashed boxes. Different shapes of each mother wavelet (in the time domain) are also added in the upper dashed boxes. The marked black region shows the signature representing the target (downdraft-updraft combination).

This result showed that the Morlet and Paul wavelets could identify the distinctive form of a downdraft-updraft combination. In contrast, the Mexican hat wavelet could not identify the downdraft-updraft combination because the Mexican hat tends to separate the downdraft and updraft. This characteristic is likely because the Mexican hat wavelet only calculates the real value. Meanwhile, the phase shift from downdraft and updraft is in complex value (De Moortel et al., 2004). Therefore, the Mexican hat wavelet was not used in this data analysis.

A detailed comparison between the Morlet and Paul wavelets showed that the Paul wavelet has a better signature pattern with a narrow shape throughout the time (horizontal axis), especially at the height between 500 and 700 m. This characteristic means the Paul wavelet could detect the very localized combination of downdraft-updraft. Another difference is the height of the signature in the scale period (vertical axis), where the Paul wavelet showed a much taller shape than the Morlet wavelet. This characteristic is correlated with the mother wavelet shape characteristic, where the Paul wavelet has less oscillation than the Morlet wavelet. A smaller number of oscillations will yield a very accurate time resolution but reduce the frequency resolution (De Moortel et al., 2004). The paul wavelet is considered the best option for distinguishing the downdraft-updraft combination due to its better signature pattern and less oscillation.

CWT 1D with the Paul wavelet is then applied to the data, with one example depicted in Figure 5.12 on July 23, 2018. Two criteria are used to define the downdraft-updraft structure; 1) wavelet power spectrum signature with a 95 % confidence level marked by a thick enclosed region, and 2) the signature must be located inside the COI area separated by a dashed black line. Based on these criteria, a signature of the downdraft-updraft structure can be collected.

Figure 5.12a shows a time variation of the vertical wind velocity at the height of 480 m. An example of the distinctive downdraft-updraft signature was detected from approximately 09:00 to 10:00 JST. The wavelet power spectrum in Figure 5.12b also shows a significant signature that conforms with these two criteria (thick enclosed region and COI).

Several thick enclosed signatures also appeared at various time occurrences and periods. The signatures are then counted on each scale period at every height with an increment of 90 m. This counted signature is defined in this study as the number of occurrences. The number of occurrences in three different conditions (convective, clear sky, cloudy) is analyzed to observe the characteristics to achieve more reliable results.

The two main results of the number of occurrences are based on the scale period and height. This study classified the period into eight classifications (0.25, 0.5, 1, 2, 4, 8, 16, 32 min). This period means the estimated duration of the downdraft-updraft combination based on the wavelet calculation. The quantified number of occurrences based on the period is shown in Figure 5.13a. The occurrences in all the weather conditions are counted. Six periods from this classification have more value, which is 0.25, 0.5, 1, 2, 4, and 8 min. The period of 0.25 min is more dominant than other periods. These six periods are probably because most of the downdraft-updraft combinations occur in a short duration.

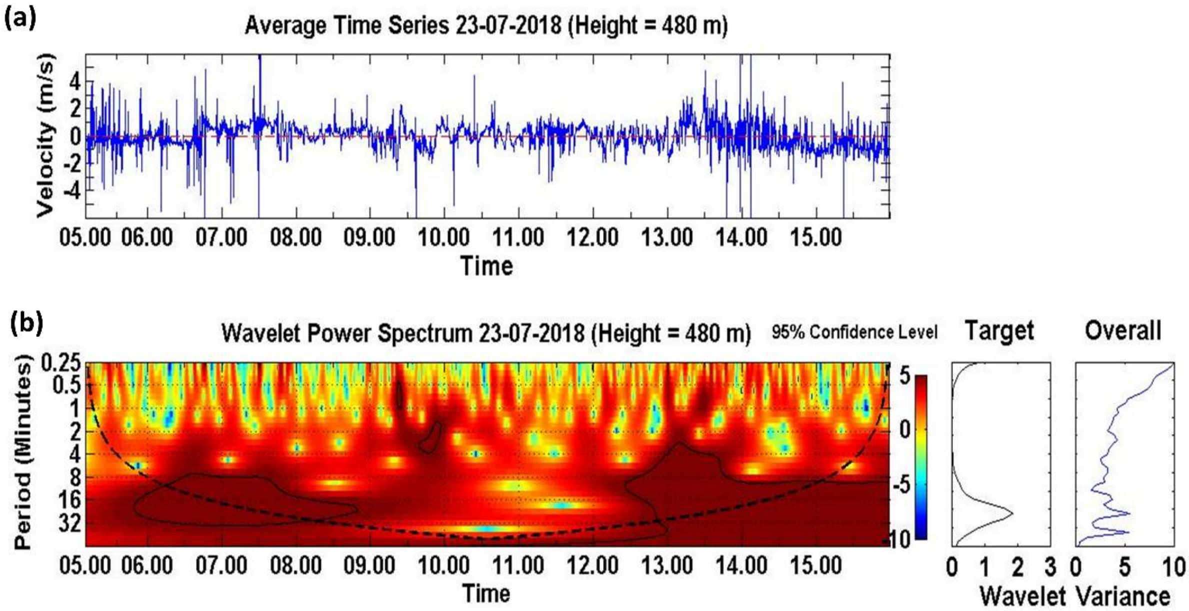

Figure 5.12. Wavelet result example using a Paul wavelet on July 23, 2018, at the height of 480 m. (a) Time variation of the vertical wind velocity and (b) wavelet power spectrum. The dashed line in Fig 4b is the COI, and the marked black curve is the downdraft-updraft signature extracted by a 95 % confidence level. The panel on the right side of (b) is the wavelet variance on each period of the downdraft-updraft signature and overall wavelet power spectrum, respectively.

Figure 5.13b shows the total number of occurrences at each height, represented by the yellow bar. This figure demonstrates that the maximum value in the convective and cloudy conditions is observed at a lower height of approximately 300 m and 400 m. Meanwhile, the colored line showed the six periods. As expected, the red curve (0.25 min period) is dominant among others. In cloudy conditions, the red curve decreases along with the height.

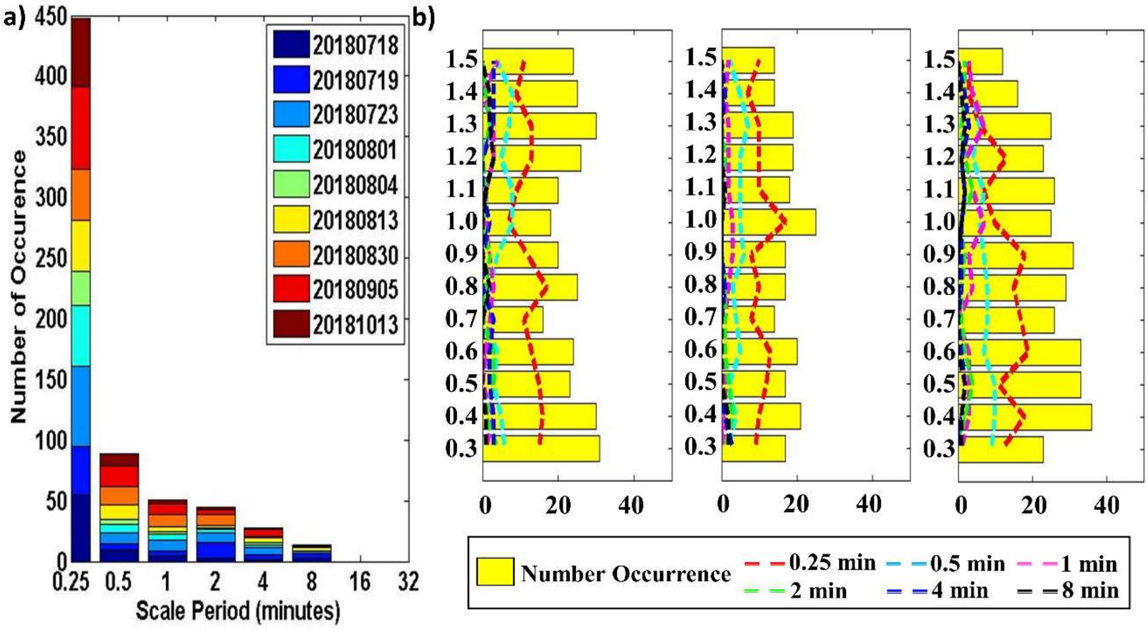

Figure 5.13. Downdraft-updraft number of occurrences, (a) based on period, (b) based on height. Fig 5b shows that only six scales of 0.25, 0.5, 1, 2, 4, and 8 min are shown.

Further analysis of the structure at six different scale periods using wavelet variance is shown in Figure 5.14. Wavelet variance is conducted by calculating a variance from the significant wavelet power spectrum over time series. This wavelet variance is shown in three different conditions (convective, clear sky, and cloudy) at three height classifications (lower: 300 - 480 m, middle: 510 - 1020 m, and upper:1050 - 1500 m), with a maximum scale period limited until 8 min refer to the result in Figure 5.13a.

Figure 5.14 showed that variance is more significant in the upper level in all weather conditions. In clear sky conditions, the variance is less than in other conditions (convective and cloudy). There are distinctive patterns in clear sky conditions in scale period 0 - 0.25 min and 2 - 4, 4 - 8 min. In the convective condition, this distinctive pattern is more and more apparent in each height classification.

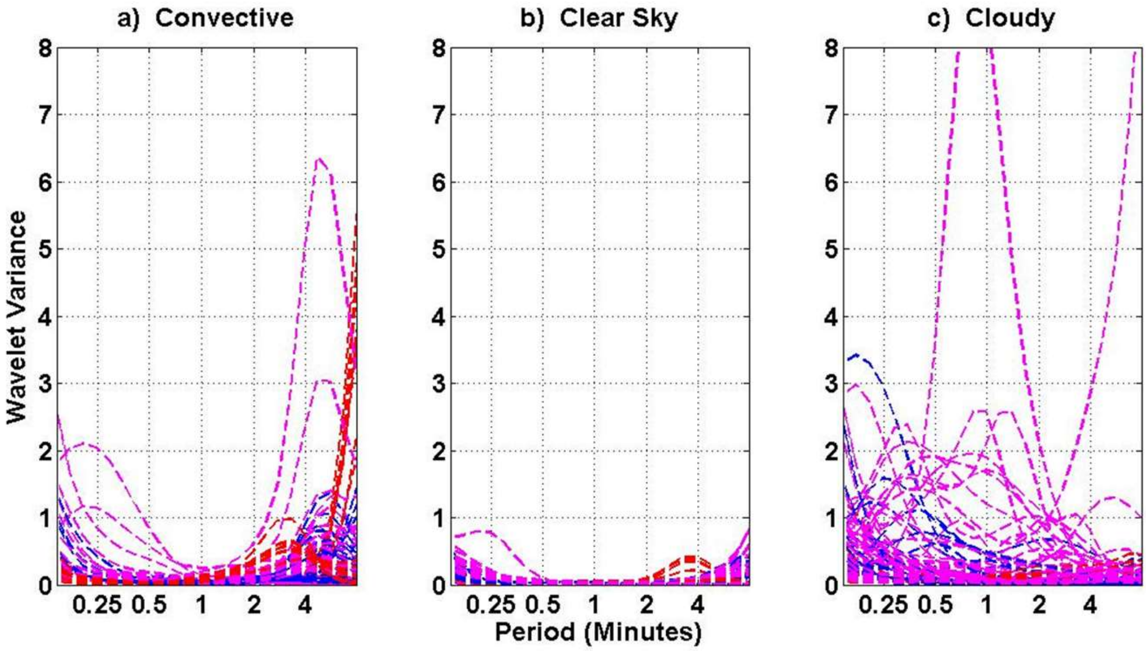

Figure 5.14. Wavelet variances based on scale periods from height 300 m to 1500 m in different weather conditions of (a) convective, (b) clear sky, and (c) cloudy. Red lines represent the variance in lower height (300 to 480 m), blue lines represent the variance in middle height (510 to 1020 m), and magenta lines represent the variance in upper height (1050 to 1500 m).

The similar pattern of downdraft-updraft along the height in the convective condition can be classified into two types: the characteristics of downdraft-updraft are always similar, and the other is that the downdraft-updraft went upward for a long distance of height so that the same downdraft-updraft showed less variance. Further analysis is required to solve this problem

Figure 5.13 and Figure 5.14 showed that the period suitable for the downdraft-updraft combination behavior is the 0-0.25 min, 2-4 min, and 4-8 min period in this study. The Paul wavelet method applied in the data can distinguish and calculate the downdraft-updraft combination. This method could help understand the downdraft-updraft behavior, especially in the convective condition, after evaluating many events.

This chapter described the advanced BLR ability to observe thermal and a combined downdraft-updraft structure around the thermal. CWT 1D is utilized to quantify and analyze the characteristics of this combined downdraft-updraft structure. Different mother wavelets and scales were compared to obtain a suitable detection of the combined downdraft-updraft structure. Vertical wind velocity measured by the advanced BLR in three different weather conditions is then examined using CWT 1D based on scale and height. The quantified number of occurrences and wavelet variance showed that the downdraft-updraft structure has a suitable period from 0 to 0.25 min, 2 to 4 min, and 4 to 8 min. Detailed analysis of the variance in every height is needed in future studies.

In this study, an appropriate mother wavelet combined with vertical wind velocity from high-resolution BLR can identify the downdraft-updraft combination on a nine-day dataset (different weather conditions). This technique, added with analysis of both power spectrum and variance, could determine the period and quantify the number of occurrences. This information is essential for understanding the downdraft-updraft behavior related to the boundary layer microscale condition, especially in convective conditions.

Chapter 6. New individual cumulus cloud observed by multiple instruments and wavelet

6.1. Cloud pixel area

The term cloud pixel area (CPA) is used in this study to represent the area of the newly developed cumulus cloud observed by the time lapse camera located at the BLR site. CPA is used to observe the cloud evolution from a camera image point of view. Since the cloud pixel area source is image data, image analysis software is utilized to quantize the cloud area. Digimizer is software often used in several research fields that need image analysis (Chenari and Mottaghian, 2020). In this study, Digimizer software calculates the pixel area from a cloud image retrieved by the camera.

Adjustment is made for the image that will be used in the analysis. The original image from the camera is 1980 x 1080 pixels. However, since the coverage of the BLR beam is only 14°, the image pixel needs to be limited. The calculation of how much limit of the image pixel is conducted by noticing the focal length of the camera, the view angle of the camera, and the zenith angle of BLR. A 500 x 500 pixel is obtained and used as a threshold to limit (crop) the image.

One event of the newly developed cloud is a sequence of cloud image that starts from the first appearance of the cloud image above the BLR site and ends until the cloud image disappear in the 500 x 500 pixel. Every cloud image of that sequence is manually calculated using Digimizer to obtain the CPA value and timestamp information from each image. Figure 6.1 is an example of one event of CPA

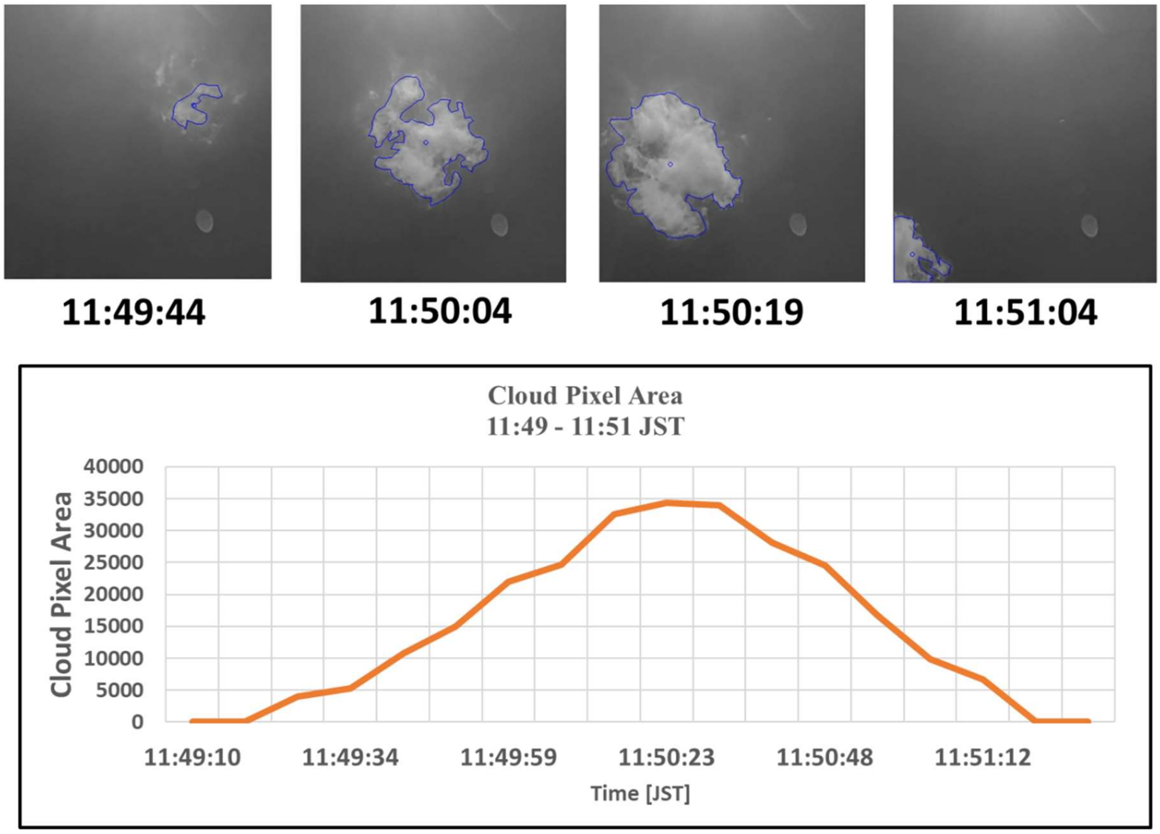

Figure 6.1. Cloud pixel area time series in a single event. The upper image is a time-lapse camera image located in BLR on September 5th, 2018 from 11:49 until 11:51 JST. The lower image is the quantized CPA time series in the same period.

A combination of several events with the nearest time is collected into one dataset. If there is an event with a longer time distance between the collected event, that event is considered a new dataset. Figure 6.2 is an example of CPA dataset. The observation was implemented during the summer season from July until September 2018 and 2020. The observation period only focused on daytime, where the high possibility of thermal occur. Fig 6.3 present the collected dataset of the CPA. A total of 40 time series of CPA from 14 datasets have been collected during observation.

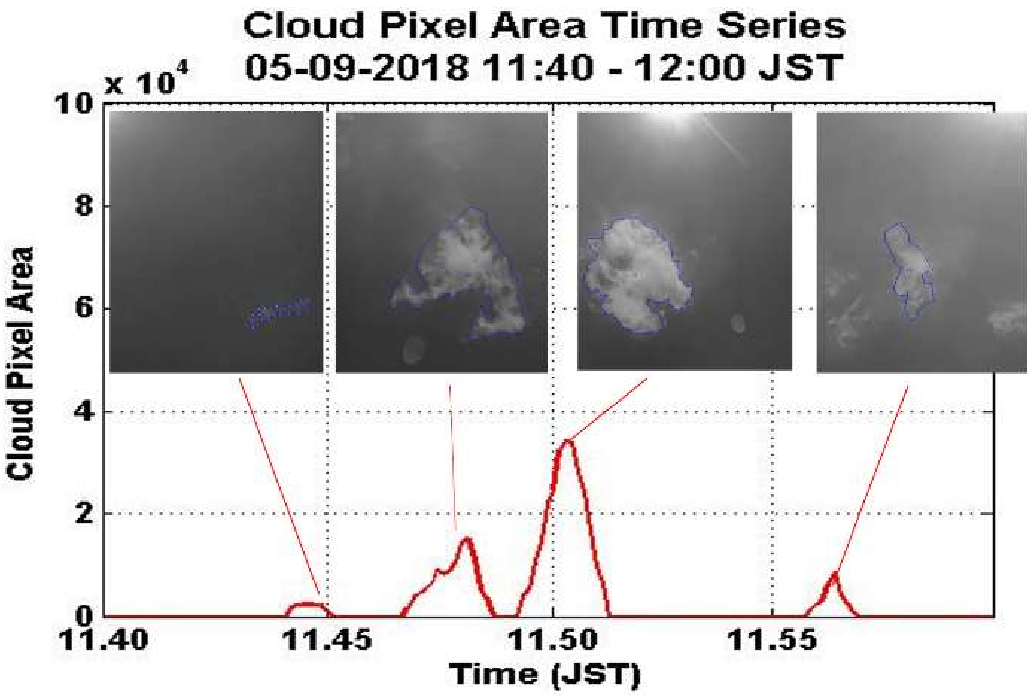

Figure 6.2. Cloud pixel area time series and cloud image on September 5th 2018 from 11:40 - 12:00 JST.

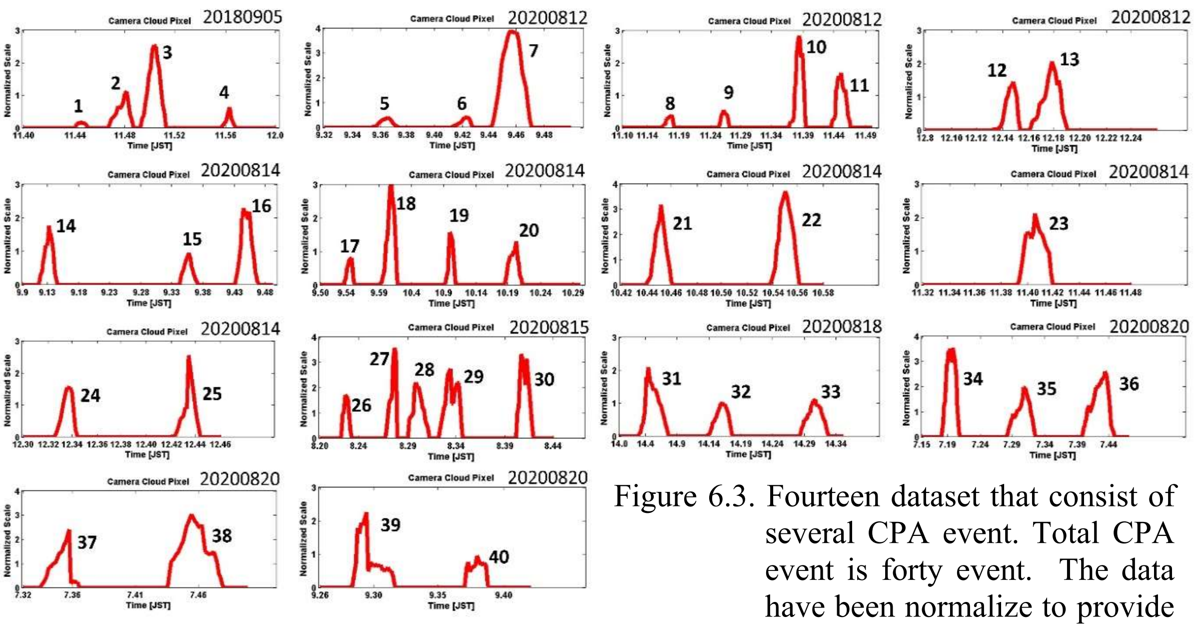

Figure 6.3. Fourteen dataset that consist of several CPA event. Total CPA event is forty event. The data have been normalize to provide comparison with other data with different unit.

6.2. Local thermal during CPA

Vertical air velocity (hereafter abbreviated to VAV) observed by the advanced BLR during the same period as the CPA observation is presented in Fig 6.4. The BLR maximum height is 5.7 km. However, we limit the height coverage from 300m to 1710 m of the BLR data since our target is in the boundary layer. The thermal structure can be observed by the positive VAV coherent structure along the height. The time series of positive VAV along the height represents the local thermal evolution.

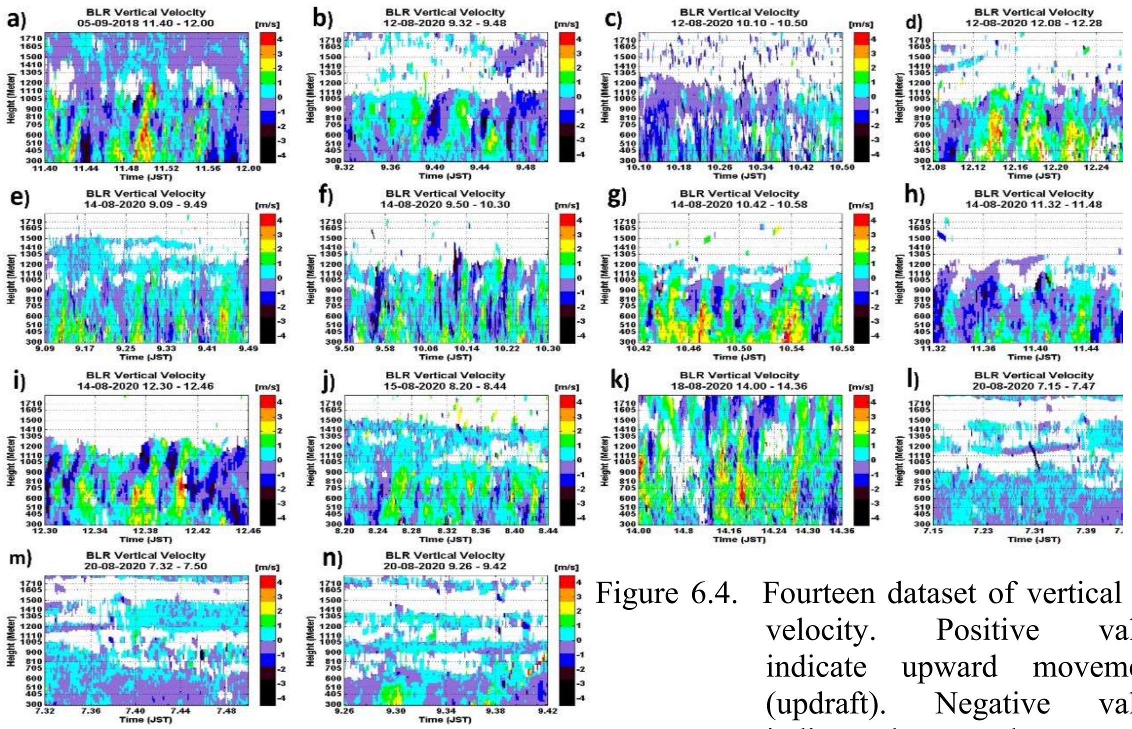

Figure 6.4. Fourteen dataset of vertical air velocity. Positive value indicate upward movement (updraft). Negative value indicate downward movement (downdraft).

Several datasets showed thermal in different duration and maximum heights. At least twelve datasets showed a clear signature of thermal observed by the BLR. Rapid observation data showed the updraft from the thermal stop at a certain height rapidly and spread horizontally in a short period before the downdraft displaced it. Several thermal try to penetrate the stable layer that keeps the further upward movement.

6.3. Wavelet coherence between local thermal and individual cumulus cloud

The relationship between individual cumulus cloud and thermal is quantified with wavelet coherence. Wavelet coherence calculates the connection between two-time series data (Ng. Eric, and Chan, 2012). The time series of CPA on each dataset indicates the individual cumulus cloud existence. Meanwhile, the time series of VAV indicates the local thermal presence. An example of these two-time series is depicted in Figure 6. 5a, with the height of the VAV being 600m. This example is taken from dataset A (September 5^{th,} 2018, 11:48 – 12:00 JST). The time-series data have already been normalized to neglect the different units. If we use a wavelet, it is important to choose the correct wavelet function (mother wavelet) based on the target signal (De Moortel et al.,2004). Morlet was selected in this study as the mother wavelet because it was well-suited to detecting changes in the cloud pixel area and the vertical air velocity.

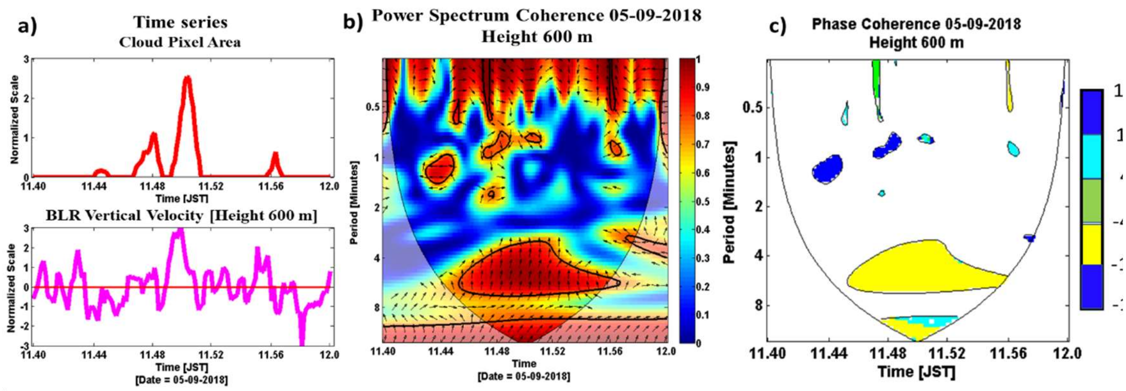

Figure 6. 5. Wavelet coherence between two time-series, a) CPA and VAV time series, b) power spectrum, c) phase classification. Color in 3c represents the phase classification. Cyan represents in phase, blue represents anti-phase, yellow represents a leading phase, and green represents the lagging phase.

Figure 6. 5b shows the power spectrum of the wavelet coherence. Colour represents the coherence level from 0 – 1, with the strongest coherence being the value near 1. The y axis represents the wavelet scale period. The appropriate result from this wavelet coherence is only chosen from the power spectrum covered with a thick black area. This covered area corresponds with the power spectrum with high coherence and high confidence level (95%) (Grinsted et al.,2004; Torrence and campo,1998). This information is picked up and later classified based on its phase classification in Fig 6.5c.

Fig 6.5c pictured the phase classification from the previous power spectrum. The color represents four classifications of the phase classification. However, this result is only at one level height of VAV, 600m. In order to analyze all the VAV heights, the same procedure is taken to every VAV from 300 to 1700 m. Furthermore, the phase classification is categorized into two types: based on heights and scale period. The average procedure is used to categorize the phase classification. Average phase classification on the x-axis represents the phase classification based on scale period. Meanwhile, the average phase classification on the y-axis represents the phase classification in one single height (Figure 6.6).

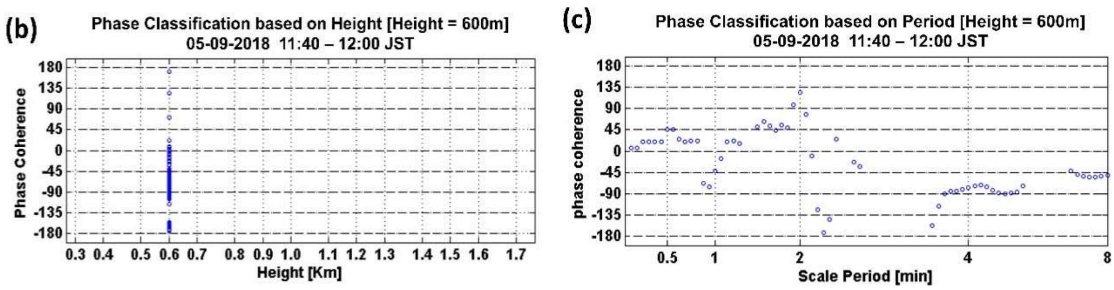

Figure 6.6. Results of phase classification for the wavelet coherence results are shown in Figure 6. 5c. a) Phase classification after averaging along the scale period at 600 m height, b) Phase classification after averaging along time at 600 m.

Figure 6.7a and Figure 6.7b depicted the result of these average procedures from 300 to 1700 m. The median calculation is conducted to find the distinct pattern from the collected phase classification. The Red dot represents the median calculation result. Focused on the leading phase (yellow region) in Figure 6.7a, a continuous leading phase is observed from height 510 until 870 m. This pattern showed the continuous leading phase of VAV towards the growth size of CPA, wherein physical meaning represents the thermal effect towards the generated cumulus cloud. The continuous leading phase also occurs in Figure 6.7b on the scale between 2 to 8 minutes. This pattern represents the possible time duration of thermal towards the generated cumulus cloud.

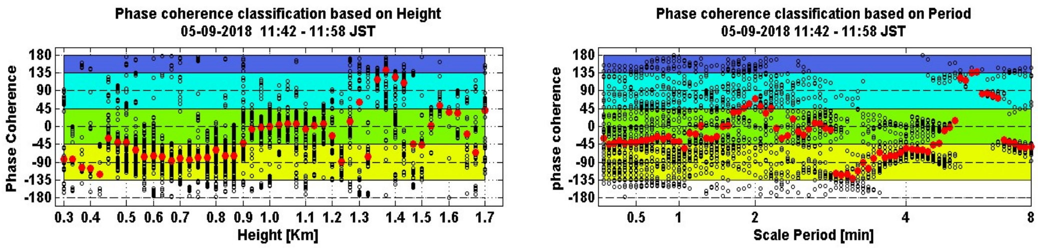

(a) (b)

Figure 6.7. Categorized phase classification, a) heights, b) scale period. The red dot represents the median calculation result. Colored areas represent different phase classifications

The next step is to apply the above procedure to other datasets. Consideration is needed only to choose the result of categorized phase classification with a continuous leading phase. Using this consideration, we retrieve 8 datasets (from a total of 14) with at least one continuous leading phase on their categorized phase classification. The 8 datasets in each category are depicted in Figure 6.8.

From 8 datasets, mostly continuous leading phase exists in the category based on the height, compared with the scale period. Focused on the height category, Only one dataset (A.8) showed that consistent phase coherence started from the lower height level. Two datasets (A.6 and A.8) showed a consistent phase coherence at 100 m intervals.

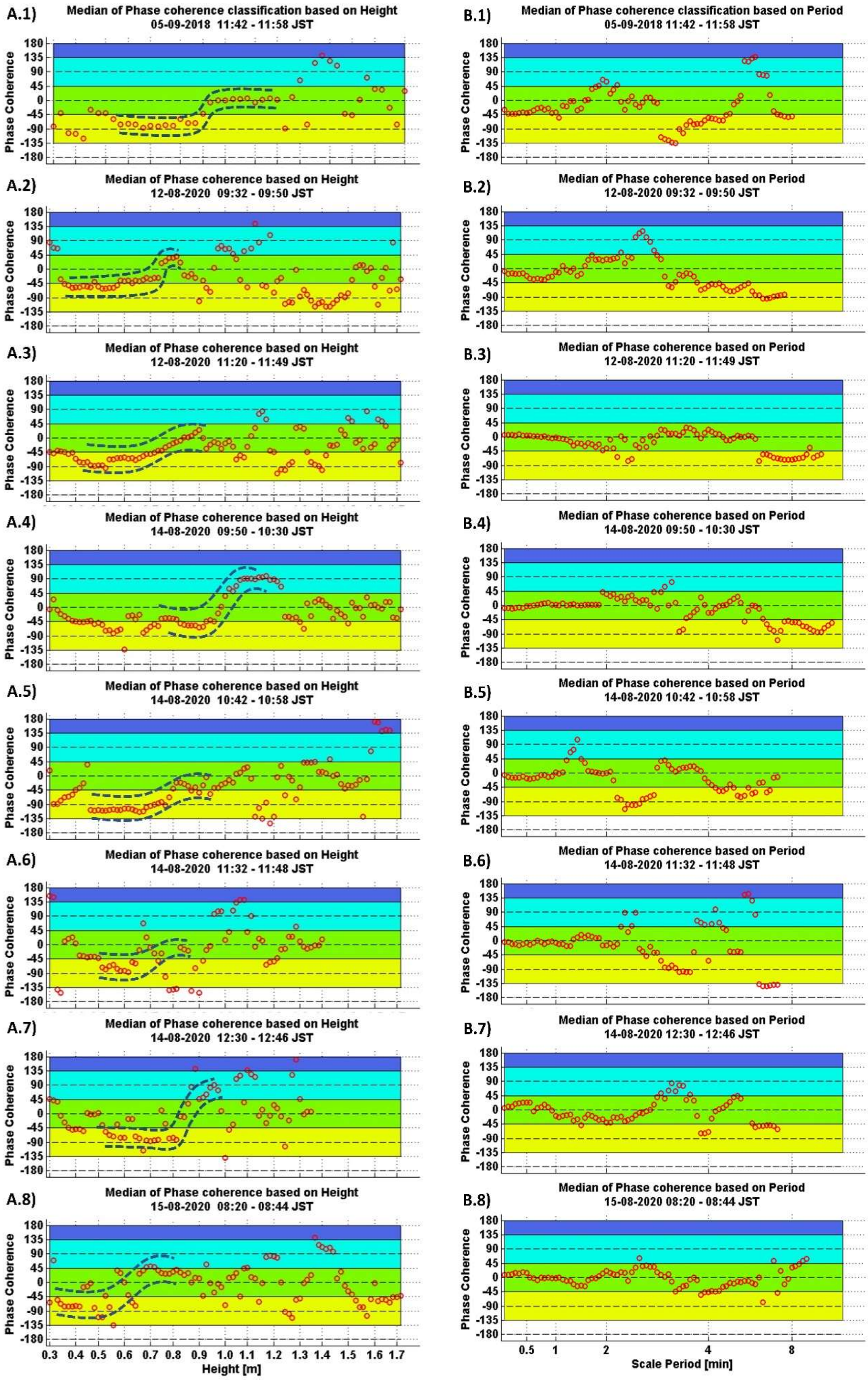

Figure 6.8. Phase classification of eight datasets in two categories, a) Height, b) Scale period. Thick dashed lines represent the continuous value from the median calculation.

Meanwhile, other datasets showed at least more than 300 m intervals. It seems there is a connection between the leading phase and in-phase in this height category. The transition from leading phased into in-phase (with further to lagging phased in a certain dataset) is shown in the form of dashed curved. The pattern is almost identical to an "S" shape with a gradient slope of change (no sudden change of phase coherence was found).

The scale period in the leading phased region did not show a significant pattern in the leading phased. However, the first phase coherence in this region is located at the scale period between 2 until 4 min. This result showed that the time needed for local thermal to have an impact on the generation of the newly cumulus cloud is at least more than 2 min. This is reasonable since the single cloud simulation by Klinger et al. (2017) showed that the first stage of cloud generation is 10 min. There is consistent phase coherence in the in-phased region, especially in the lower scale period until 1 min. However, the cloud pixel area existence is dominantly showed more than 1 min interval. Furthermore, the vertical air velocity in this in-phased region is mainly located when there is no cloud pixel area. Following this matter, this consistent phase coherence is considered noise.

6.4. Vertical vorticity during the local thermal and the individual cumulus cloud

Vertical vorticity is derived from Doppler lidar data using the pseudo vorticity method. However, Doppler lidar is highly sensitive to airflow. That is why it is necessary to have criteria for choosing the appropriate vorticity from doppler lidar-pseudo vorticity. Four criteria are then introduced in this study to determine the vertical vorticity. The criteria are adapted from the tilting process in the early stage of a supercell (Rottuno, 1981; Dahl, 2017; Nakakita et al., 2017).

The condition that could generate vertical vorticity is introduced with four criteria. The first condition is the source of horizontal vorticity. Horizontal vorticity is generated by the vertical shear condition along with the height. The presence of vertical shear of horizontal wind is the first criteria used in this study. The second criteria are the presence of updraft, which in this study is thermal. The updraft will tilt the horizontal vorticity into a vertical position if the horizontal vorticity interacts with thermal (vertical vorticity).

The third criteria are the direction of the vortex. The tilting of horizontal vorticity into vertical vorticity would cause a change of orientation of the vortex. The environmental wind influences these changes. The fourth criteria are the grid size of the data. In this study, the Doppler lidar mesh grid is only considered using a 9 x 9 mesh grid (approximately 400 x 400 m). This grid size represents the thermal effect it has on the vertical vorticity.

Fig 6.9 represents the example of vertical vorticity based on the four criteria mentioned above. Fig 6.9a showed two pairs of vorticity with different orientations (anticlockwise = red, clockwise = blue) around the black circle which is the BLR location. The horizontal wind profile showed wind speed at the lower height slightly smaller than at the upper height (Fig 6.9b). This condition could cause horizontal vorticity to generate in the lower level. The presence of updraft from thermal (Fig 6.9c) would cause the horizontal vorticity to lift vertically (tilted), which would cause a change of vorticity orientation.

Following the tilted mechanism in the supercell (Rottuno, 1989), the location of the anti-clockwise (clockwise) vorticity would be on the south (north) side of the located updraft, which is the BLR location. The reason is that the environment wind is towards the northeast direction. Three data in Fig 6.9a-Fig 6.9c showed that the pair of vorticity most suitable for vertical vorticity at the height of 480 m. Then we could retrieve the maximum and minimum vorticity values for the next analysis.

Another example is in Fig 6.9d – Fig 6.9i, where Fig 6.9e and Fig 6.9h showed almost the same horizontal wind behavior (higher wind speed at upper height than lower height). However, the wind direction is slightly different from Fig 6.9b, wherein in these two cases (Fig 6.9e and Fig 6.9h), the wind direction dominates towards the east-southeast direction. The updraft condition also exists during those periods. Using the same procedure, we could also determine the vertical vorticity located at the height of 480 m.

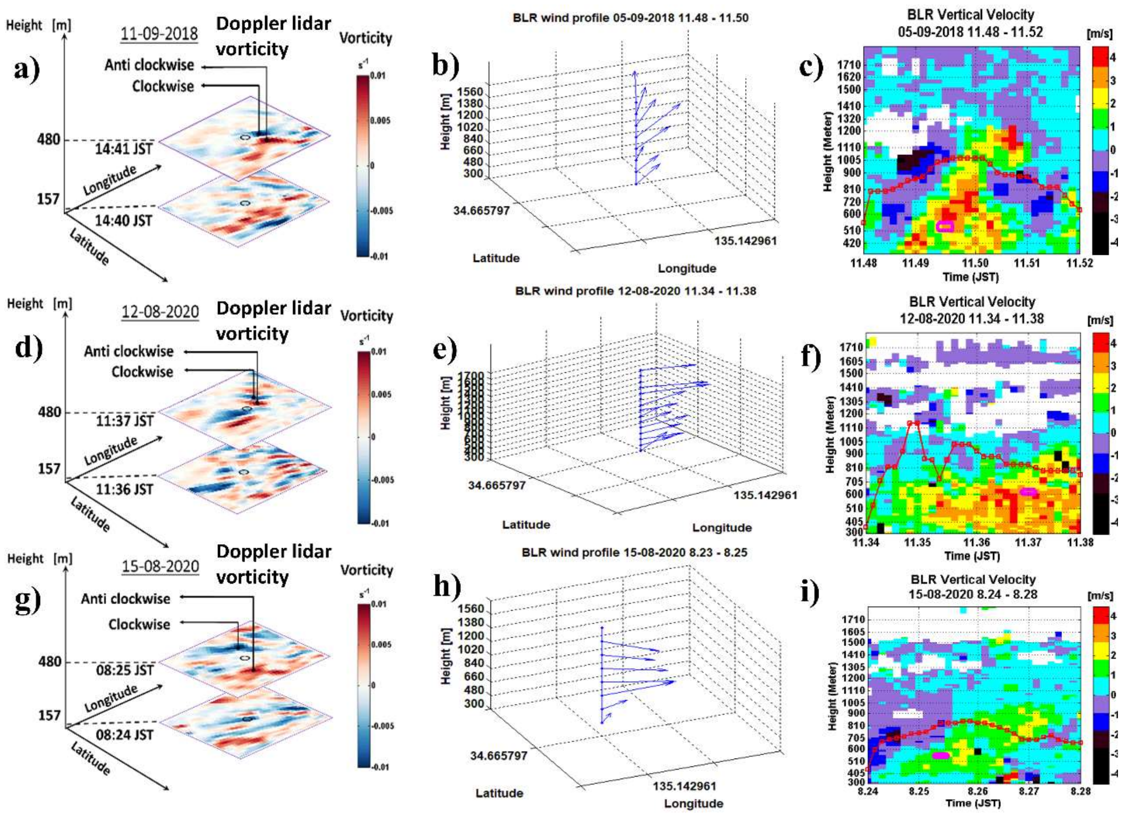

Figure 6.9. Example of vertical vorticity determination, a-d-g) vertical vorticity from Doppler lidar, b-e-h) horizontal wind derived from BLR, c-f-i) VAV from BLR. The anti-clockwise and clockwise arrows in a-d-g) represent maximum and minimum vorticity.

6.5. Correlation between vertical vorticity with vertical air velocity properties

Previous research by Nakakita et al. (2017) found that there is a vortex tube tilting process before the generation of a rain cell inside the cloud. This tilting process involves a combination of the updraft condition and vertical shear of the horizontal wind. Meanwhile, the vertical shear of horizontal wind is observed using the DBS method. A vortex tube tilting is indicated by the existence of pair of clockwise and anti-clockwise vertical vortex tubes along the updraft. Using the pseudo vorticity method, doppler velocity from a single radar or doppler lidar could identify this condition by deriving vertical vorticity.

After obtaining 8 datasets showing a strong relationship between local thermal and single cumulus cloud development, a detailed analysis of the cloud dynamics process is investigated. Vertical vorticity observation using Doppler lidar is observed during these eight datasets with 27 events of an individual cumulus cloud. Since the Doppler lidar scan strategy only has 2 PPI scans, only the upper PPI elevation angle (13.5°) with coverage area around BLR location was used in this study. The estimated height of vertical vorticity co-located with BLR is approximately 480m. Using the four criteria, only 13 events (from a total of 27 events) could pick up as vertical vorticity. A comparison of the vertical vorticity and the VAV condition is then conducted to find their correlation. Only maximum and minimum vorticity values were used for this comparison. Table 6.1 shows the 13 events that consist of vertical vorticity values and VAV properties.

The Pearson correlation coefficient measures the linear association between vorticity and the other two variables (VAV and vertical shear). Fig 6.10 shows the correlation coefficient result between vorticity and VAV. A moderate correlation was found between maximum vorticity from Doppler lidar with maximum VAV from BLR. This result showed a moderate relation between maximum vertical vorticity and thermal updraft presence. However, it is still unclear why only maximum vorticity has a moderate relation. It still needs further investigation.

Table 6.1. Properties of Vertical vorticity and VAV in 13 events.

Event	Date	Vorticity (10^{-3})			VAV (480 m height within 2 min data period)			
		time	max	min	period	mean	max	variance
3	20180905	11:49:42	7.93	-8.754	11:47:48-11:49:42	1.1317	4.493	2.7941
4	20180905	11:54:30	2.763	-4.192	11:52:26-11:54:29	0.131	1.892	0.716
7	20200812	09:45:12	2.013	-4.45	09:43:12-09:45:15	0.3264	2.151	1.3776
10	20200812	11:37:16	8.686	-9.179	11:35:17-11:37:12	2.565	4.495	0.9038
11	20200812	11:43:19	5.743	-6.201	11:41:19-11:43:21	3.3639	5.472	1.0444
14	20200814	10:09:54	6.525	-9.583	10:08:45-10:09:54	0.8881	3.253	1.3686
17	20200814	10:52:18	7.22	-7.326	10:51:05-10:52:11	0.8482	3.243	0.4686
18	20200814	11:37:44	5.167	-6.649	11:35:44-11:37:47	0.3557	2.442	0.6497
20	20200814	12:41:21	2.734	-4.909	12:39:13-12:41:16	0.8661	2.302	0.6634
22	20200815	08:25:40	8.76	-10.16	08:23:23-08:25:34	0.1087	1.928	1.6302
23	20200815	08:28:41	8.164	-5.229	08:26:31-08:28:34	0.0646	4.697	4.3008
24	20200815	08:31:43	1.009	-2.701	08:29:48-08:31:42	0.8286	2.136	0.4507
25	20200815	08:40:48	6.035	-6.027	08:38:40-08:40:43	0.5463	2.301	0.5466

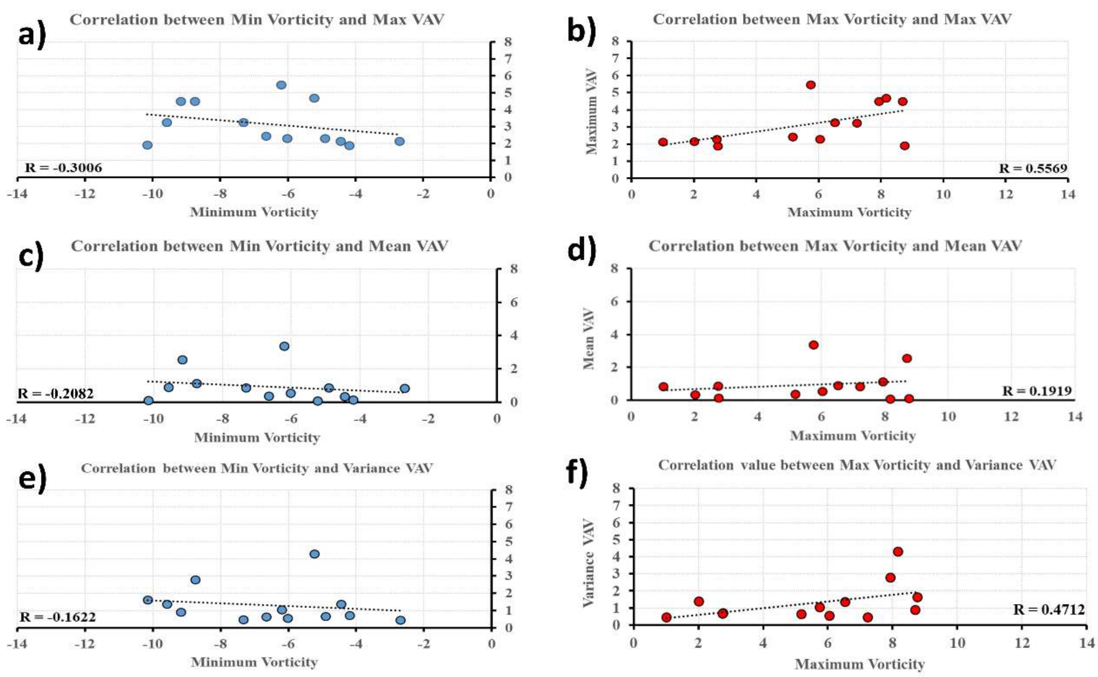

Figure 6.10. Pearson correlation coefficient between vertical vorticity and VAV properties, a) Min vorticity and max VA V, b) Max vorticity and min VAV, c) Min vorticity and mean VAV, d) Max vorticity and mean VAV, e) Min vorticity and Variance VAV, f) Max vorticity and variance VAV.

6.6. Correlation between vertical vorticity and vertical shear

The vertical wind shear of horizontal wind is calculated using several conditions. First, the calculation only uses 1 minute duration of VAV before the Doppler lidar data. (ex, if the vorticity data is in 08:25:34 JST, the 1-minute calculation would be 08:24:36 JST depending on the BLR data). The next condition is to retrieve zonal (U) and meridional (V) components from the horizontal wind observed by the DBS method. The next step is the time average on each U and V of 1 min duration. Then the wind speed and direction can be obtained using Equations 6.1 and 6.2. Vertical shear can be achieved by calculating the difference between wind speed at heights 480 m and 300m divided by 180m. Table 6.2 is the vertical shear result, with a correlation coefficient value in Fig 6.11.

$$\text{Wind speed} = \sqrt{U^2 + V^2} \tag{6.1}$$

$$\text{Wind direction} = \tan^{-1}\left(\frac{V}{U}\right) \tag{6.2}$$

Table 6.2. Properties of Vertical vorticity and Vertical shear in 13 events

event	**date**	**Vorticity (10^{-3})**			**Vertical shear of Horizontal wind (480 and 300m height)**	
		time	**max**	**min**	**Period**	**shear**
3	20180905	11:49:42	7.93	-8.754	11:48:38 – 11:49:42	11.8
4	20180905	11:54:30	2.763	-4.192	11:53:27 – 11:54:29	3.97
7	20200812	09:45:12	2.013	-4.45	09:44:10 – 09:45:15	3.88
10	20200812	11:37:16	8.686	-9.179	11:36:09 – 11:37:12	7.02
11	20200812	11:43:19	5.743	-6.201	11:42:19 – 11:43:21	8.22
14	20200814	10:09:54	6.525	-9.583	10:08:45 – 10:09:51	11.5
17	20200814	10:52:18	7.22	-7.326	10:51:05 – 10:52:11	6.17
18	20200814	11:37:44	5.167	-6.649	11:36:41 – 11:37:47	5.75
20	20200814	12:41:21	2.734	-4.909	12:40:19 – 12:41:16	2.62
22	20200815	08:25:40	8.76	-10.16	08:24:36 – 08:25:34	5.09
23	20200815	08:28:41	8.164	-5.229	08:27:37 – 08:28:34	7.53
24	20200815	08:31:43	1.009	-2.701	08:30:45 – 08:31:42	5.92
25	20200815	08:40:48	6.035	-6.027	08:39:46 – 08:40:43	6.44

Fig 6.11 shows the correlation coefficient result between vorticity and vertical shear. The strongest correlation is only a moderate coefficient correlation level (0.5 until 0.7). Moderate correlation is shown on both vorticities (maximum and minimum) with vertical shear of the horizontal wind. This correlation indicates that the vertical vorticity detected by the Doppler lidar moderately corresponds with the vertical shear detected by the BLR.

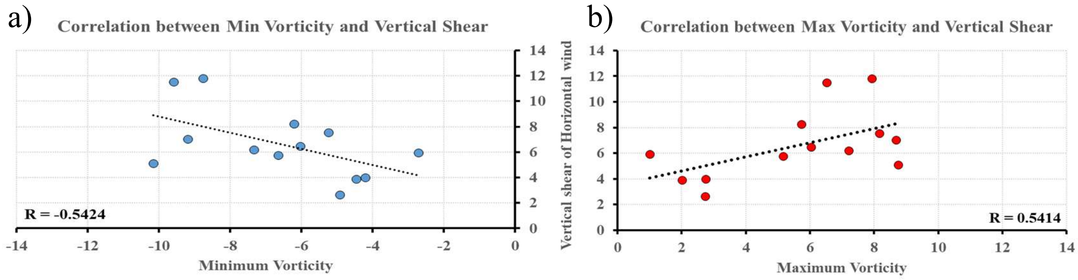

Figure 6.11. Pearson correlation coefficient between vertical vorticity and vertical shear, a) Min vorticity and vertical shear, b) Max vorticity and vertical shear.

Quantitative assessments on the relationship between local thermal and individual cumulus clouds using field observation have been conducted in this study. Using high-resolution instrument make this assessment possible to perform. This study gives more detailed information that supports the previous research using numerical simulation. We found that using the leading phase from wavelet coherence will show which height of thermal impacts the individual cumulus cloud growth size and the period when the impact is most likely significant. At least it needs more than two minutes for the thermal to impact the cumulus cloud initiation, based on field observation. The maximum height of the consistent leading phased proves quantitatively that the interaction between local thermal and the individual cumulus cloud occurs within the boundary layer.

This result is possible using a combination of detailed datasets from a high temporal resolution instrument and a wavelet coherence method. High temporal resolution from BLR and the time-lapse camera will provide a detailed time-series dataset that could capture the small and rapid process of cloud initiation. Wavelet coherence offers the tool to analyze the different thermal and cumulus cloud phases.

Several results from Doppler lidar showed that the thermal also could generate vertical vorticity. However, this study cannot provide significant proof (whether from the relation with vertical shear and maximum-minimum vorticity) that thermal generates the vertical vorticity. The vertical vorticity between the individual cumulus cloud and the vertical shear of horizontal wind only showed moderate correlation using Pearson coefficient correlation. The reason is related to the wind profile data bias, especially in the lower elevation. This bias would also affect even more for the wind shear. Furthermore, the relationship between vertical vorticity and VAV showed moderate correlation only on max VAV and max vorticity. The rest of the correlation showed a low linear correlation.

Detailed observation of the individual cumulus cloud has been observed by using advanced BLR, time-lapse camera, and Doppler lidar. Fourteen datasets that consist of forty events of an individual cumulus cloud are categorized as a forced cumulus cloud observed by its cloud evolution. One factor that triggers this cloud initiation is the local thermal effect. This showed by the quantification result of wavelet coherence between cloud growth from cloud pixel area and thermal from vertical air velocity. The leading phase from the wavelet coherence result indicates thermal impact toward the cloud. More than half of the total datasets (eight from fourteen datasets) showed a distinctive pattern of continuous leading phase.

This continuous leading phase appears at a certain height of the thermal, which shows the sustained updraft from the thermal also affects the cloud growth due to its elongated vertical thermal structure. Based on wavelet scale period information, the start of the impact of the local thermal on the cloud initiation needs at least more than two min duration. The local thermal also generates vertical vorticity almost the same period as the forced cumulus cloud. The average time difference between vertical vorticity existence and the start of the forced cumulus cloud is one minute. This vertical vorticity generation is supported by the horizontal wind condition observed by the advanced BLR using the DBS method. Vertical shear from the horizontal wind could generate horizontal vorticity, and with the help of an updraft from thermal, it will be tilted and generate vertical vorticity.

Pseudo vorticity was applied to Doppler lidar data to derive the vertical vorticity value. Four criteria (presence of vertical shear, presence of updraft, pair of vorticity orientation in relation to the horizontal wind condition, and coverage area by 400x400 m corresponding with the BLR location) are used to determine the exact vertical vorticity value. Within the previous eight datasets that have a total of twenty-seven events of forced cumulus clouds, thirteen events showed vertical vorticity observed by Doppler lidar.

Pearson correlation coefficients are used to analyze whether vertical vorticity comes from the tilted horizontal vorticity. A moderate correlation was found between maximum and minimum vorticity from Doppler lidar with vertical shear from BLR. This suggests that there is a moderate relation between vertical vorticity with the vertical shear of the horizontal wind. A moderate correlation is also found between maximum vorticity and the maximum updraft in relation to the updraft. Future studies are necessary to investigate why only maximum vorticity shows moderate relation with the maximum updraft. Future studies should be extended by observing the meteorology factor during the cloud initiation using a high-resolution instrument.

Chapter 7. Vortex tube during cumulus cloud initial stage

7.1. Early stage of cumulus humilis based on Ka-band radar first echo

This chapter describes the further observation of vorticity using Doppler lidar during the first echo of Ka-band radar. Previous research by Nakakita et al. (2017a) has achieved an early detection of GHR by detecting the “baby rain cell” observed using the first echo of X-band radar. Baby rain cell is a term used to describe the first precipitation genesis that forms inside the cloud. Detection of a baby rain cell with a vortex tube could give 10 – 15 min additional time before the GHR occurs.

Another type of radar, Ka-band radar, has higher sensitivity for baby rain cell detection than X-band radar. Several studies utilize Ka-band radar first echo to observe the early stage of cumulus cloud (Nakakita et al.,2017b; Knight and Miller, 1993) as a convective initiation indicator. Previous research also showed a relationship between the first echo height and the LCL (Lifting Condensation Level). However, the developing mechanism before baby-rain cell generation (in this term is the first echo from Ka-band radar) still lacks information.

The first echo from PPI Ka-band represents the baby rain cell inside the cumulus cloud, represented by horizontal reflectivity with a threshold from -20 until -15 dBZ (Nakakita et al., 2017b). This value is already projected in the cartesian coordinate, considering both radar distance and earth curvature radius. Ka-band radar scan strategy with a total elevation angle of 11.

The ideal case is to observe only the PPI with a lower elevation angle to get a better condition of the first echo. However, there are many grounds clutter available in the Kobe urban area. That is why only PPI with an elevation of 5° is considered suitable in this study. In order to check whether this first echo is genuinely from the cloud source (not noise), a cloud image from a time-lapse camera at the same period is used as a reference.

A time-lapse image from a two-time lapse camera is utilized to observe the cloud evolution. The two-camera are installed in the same building with a distance of 76 meters pointing towards the northwest direction. A wide field of view of 112° gives a broad coverage of the surrounding image. These two cameras are time-synchronized using NICT time reference, with a time difference of only 12.5 s and 4.5 s with the time reference. Image resolution is 1920 x 1080 pixels with a generated image every 10 s.

Ka-band radar detected the first echo from reflectivity data at 14:34 JST (Fig 6.4a) in PPI elevation 5° with an estimated echo height of 932 m (range distance 10.7 km from the radar location). This first echo only appears one time at 14:34 JST. Images from two cameras (camera A and B) are used to confirm that the first echo comes from the cloud. Two images at the same period of the first echo (Figure 7.1b and Figure 7.1c) showed a cumulus cloud in front of the Doppler lidar. This cloud had an elongated shape similar to the first echo structure (Figure 7.1a). From this comparison, it is confirmed that the first echo is coming from a cloud source. This cumulus cloud could be categorized as an isolated cumulus cloud since the image sequence (not shown here) between 14:20 JST until 14:40 JST showed the cloud location in almost the same area.

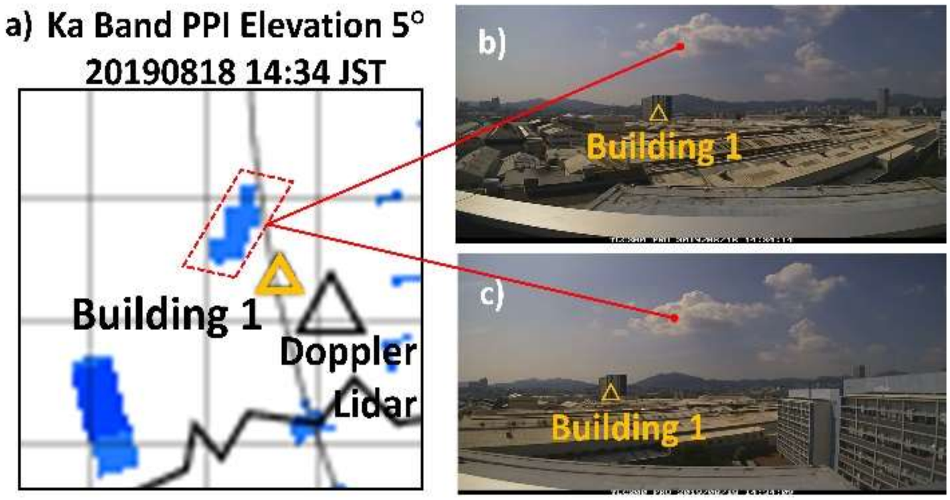

Figure 7.1. First echo and cloud confirmation, a) Ka-band radar First echo, b) Camera A, c) Camera B.

7.2. Doppler lidar point of view

7.2.1. Vorticity

The next step is to utilize Doppler velocity from Doppler lidar data based on aerosol particle movement. Doppler velocity represents positive and negative values (unit in m/s). A positive value means the target particles move away from the Doppler lidar location. Meanwhile, a negative value indicates that target particles move towards Doppler lidar.

Before utilizing Doppler velocity data, it is essential to conduct quality control of the data described in chapter 3.1.2. After data quality control, Doppler velocity data are processed to observe the divergence-convergence area, variance, and vorticity. Divergence-convergence and variance are used to analyze whether an updraft exists during the first echo. Meanwhile, vorticity is used to observe whether vorticity exists during the first echo.

7.2.2. Convergence-divergence

Figure 7.2 shows the divergence-convergence value before and during the first echo. The positive value represents divergence, and the negative value represents convergence. The black dashed area is the focused area location of the first echo. The horizontal wind direction observed from the nearest radiosonde launch showed south-easterly wind at the height of 100–200 m. This condition supports the probability of a perpendicular convergence line from the Doppler lidar point of view. A comparison between Figure 7.2a (before the first echo) and Figure 7.2b (during the first echo) showed that there is a significant amount of negative value (convergence) inside the focused area in Figure 7.2b. Continuous convergence area from height 100 m until 172 m is intensified during the first echo. From here, we could assume that an increase in updrafts occurs during the first echo.

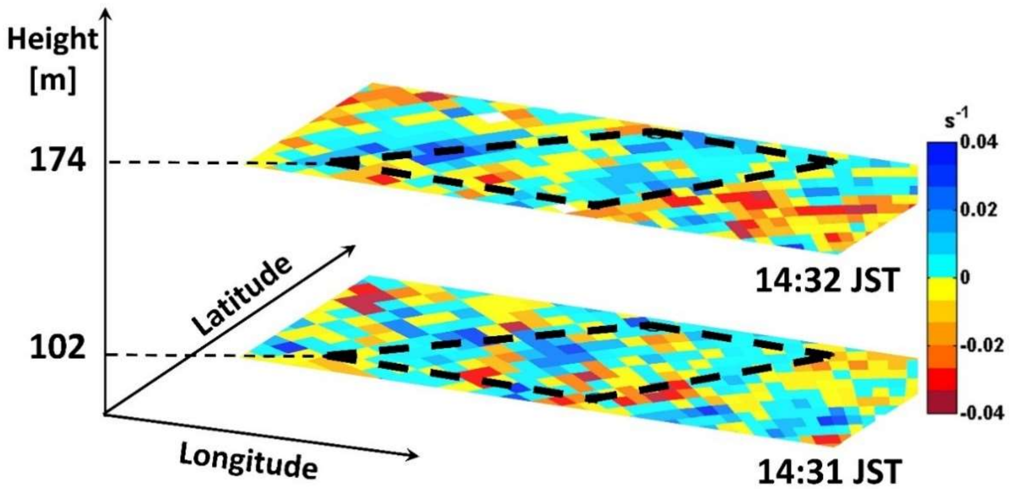

(a)

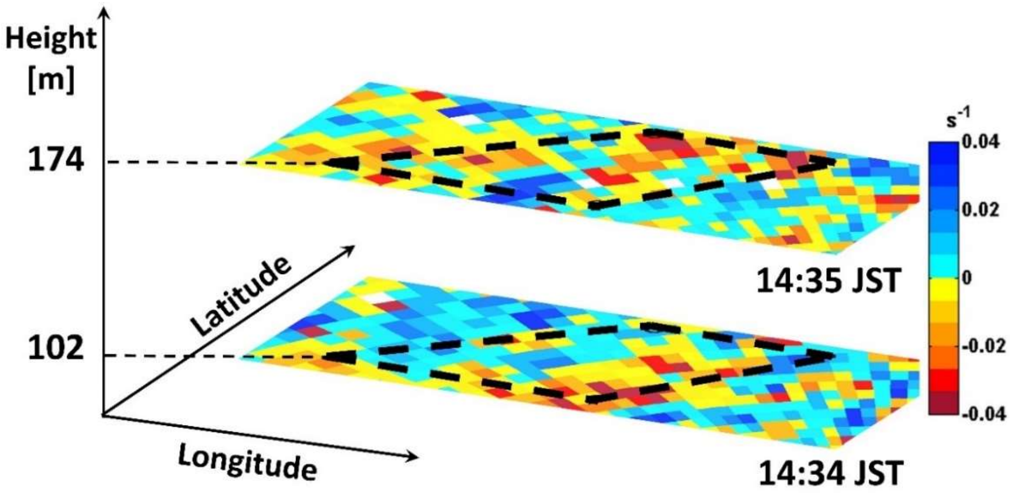

(b)

Figure 7.2. Divergence-Convergence, a) Before first echo, b) During the first echo.

7.2.3. Variance

In order to strengthen the updraft location analysis, variance results were used. Colour represents the variance value in the focused area of the first echo. Firstly, variance test performance during clear sky conditions is conducted to determine the appropriate window grid size. Varied window grid sizes are applied in the test to find the minimum variance value. A window grid size of 4 x 4 has a suitable minimum variance during the test. This window grid size is later used in the following calculation.

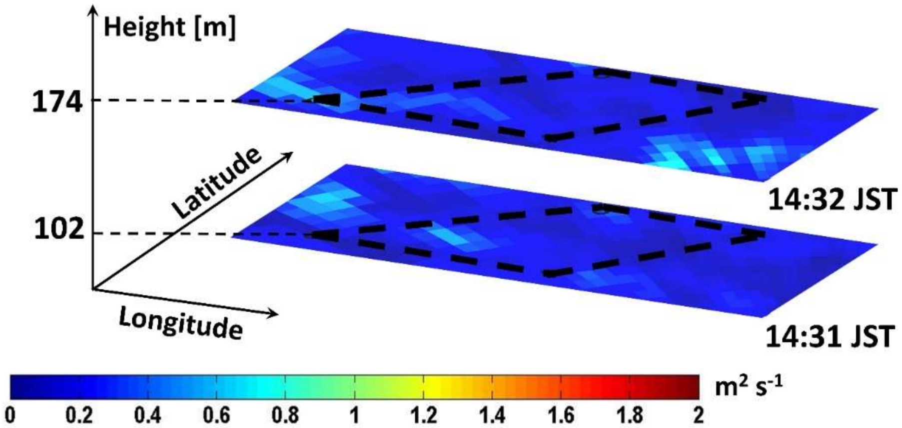

(a)

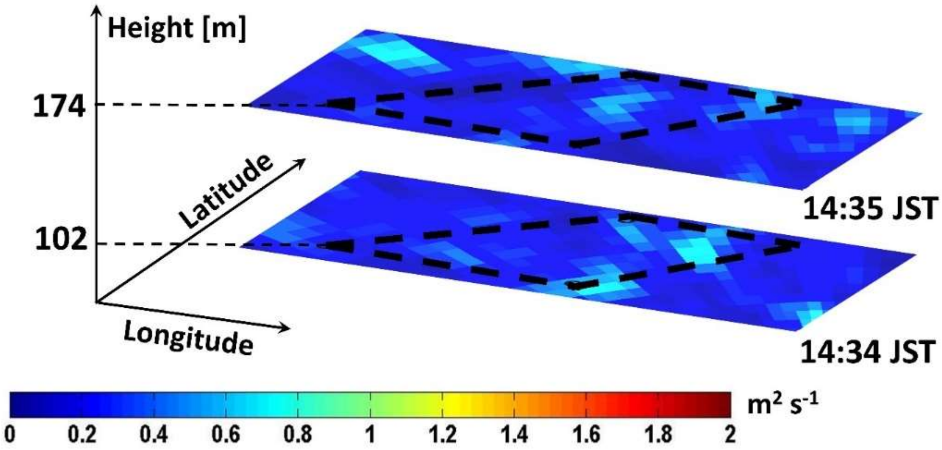

(b)

Figure 7.3. Variance, a) Before the first echo, b) During the first echo.

There is little significant variance inside the focused area before and during the first echo (Figure 7.3). However, there is still a variance value from 0.6 – 0. 8 m^2s^{-1} that exists on both heights. Higher variance seems co-located with the convergence location of Figure 7.2. In order to clarify this, a quantitative comparison between variance value and divergence convergence was conducted.

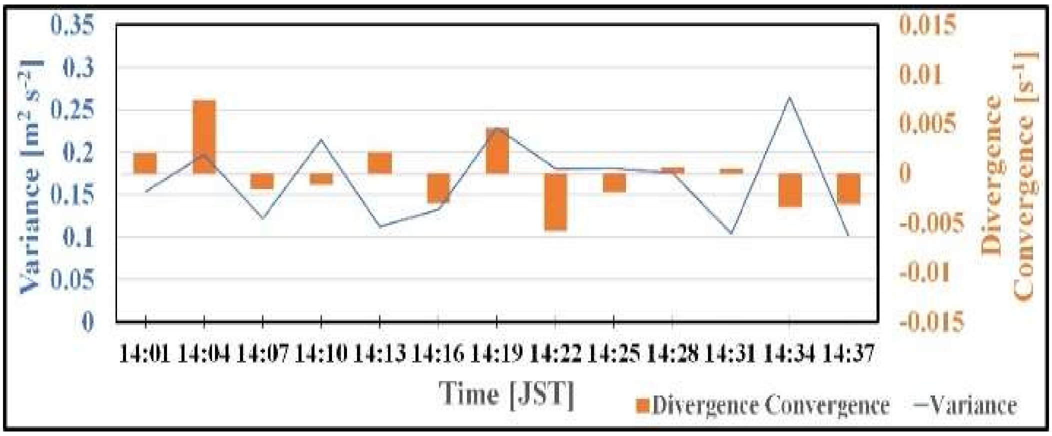

(a)

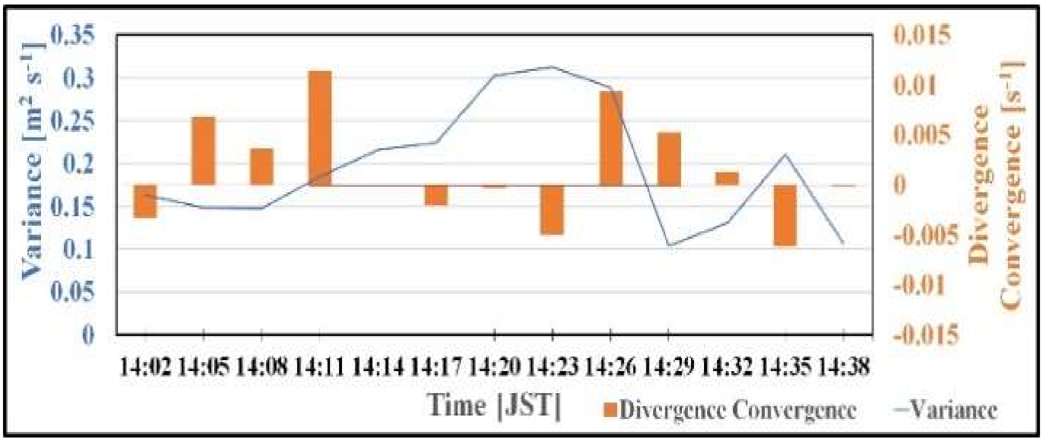

(b)

Figure 7.4. Quantitative comparison between variance and divergence convergence at different elevations, a) 4.5°, b) 9°.

The variance value only at the focused area of the first echo is calculated using the median value. The median value was used to find the reasonable variance within the area representing the variance. Meanwhile, the divergence convergence value at the same area is calculated using the average. Average is used because two values (positive and negative) represent the dominant characteristic (divergence or convergence) within the area. The comparison results from 14:00 – 14:38 JST (30 min before the first echo occurs) are shown in Figure 7.4. This figure showed that the variance fluctuation is more or less affected by the increase of divergence (positive value) and convergence (negative value).

Although the convergence increase is not linear with the variance fluctuation during the first echo (14:34 JST), the sharp increase pattern of variance is quite the same. We could notice that the variance during the first echo is well affected by the convergence value. Figure 7.4a and Figure 7.4b showed the continuous convergence value on both heights during the first echo (14:34-14:35 JST). These results indicate that updraft occurs during the first echo. Before this period, there was also a continuous convergence value on period 14:22-14:23 JST. Based on this result, we will use this period to limit the vorticity calculation only from 14:22 JST until 14:35 JST.

7.3. Identification of vortex tube

Calculated vorticity using the pseudo vorticity method (chapter 3.2.1) is shown in Figure 7.5a - Figure 7.5e. The colored vorticity value represents the vorticity direction (positive-anticlockwise, negative-clockwise). The vorticity value is smaller than the one found in the previous research using X-band (Nakakita et al.,2017a) and Ka-band radar (Nakakita et al.,2017b). This condition is reasonable since vorticity from Doppler lidar does not come from inside the cloud but at the lower height below the cloud. Twelve minutes before the first echo (Figure 7.5a), a pair of vorticity (A_1) at the height of 102 m was located inside the focused area. At the top of it, there is another pair of vorticity (B_1) one minute after. Pair of vorticity that is lifted vertically is called a vortex tube. Condition of A_1 and B_1 can be identified as a vortex tube. However, each maximum positive and negative vorticity of A_1 and B_1 are in different locations, where B_1 is tilted more to the northwest.

There is also a vortex tube nine minutes before the first echo (Figure 7.5b). In this period, the B_2 location is also slightly shifted to the northwest from the location of A_2. No vortex tube was found between 14:28 JST and 14:32 JST (Figure 7.5c and Figure 7.5d). Although, there are pairs of vorticity on either each height of A_3 (14:28 JST) and B_4 (14:32 JST). Meanwhile, during the first echo (Figure 7.5e), vortex tubes exist with the position of B_5 shifted to the northwest side from A_5.

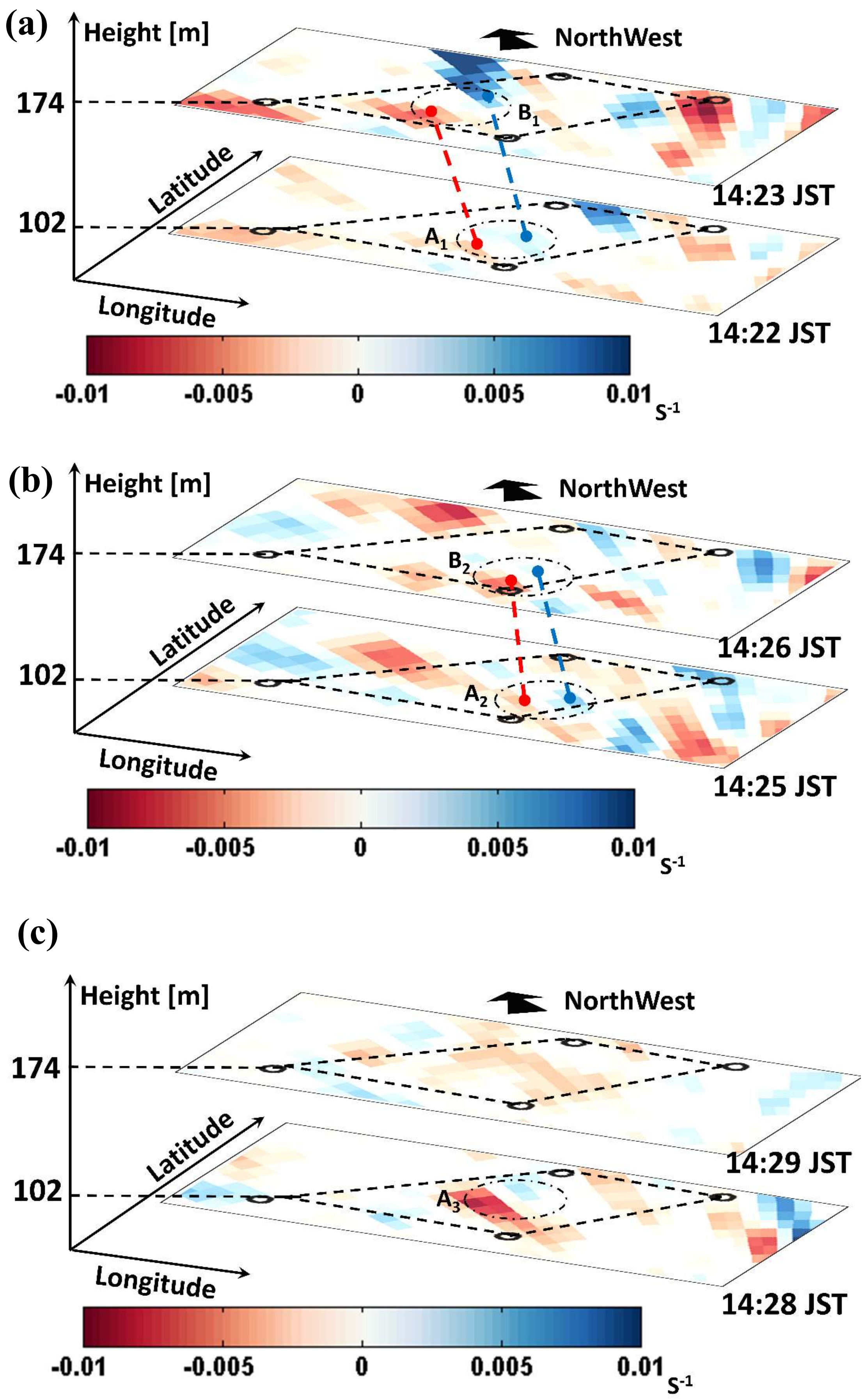
(a)
Height [m]
NorthWest
174
102
Latitude
Longitude
B_1
A_1
14:23 JST
14:22 JST
-0.01
-0.005
0
0.005
0.01
s^{-1}
(b)
Height [m]
NorthWest
174
102
Latitude
Longitude
B_2
A_2
14:26 JST
14:25 JST
-0.01
-0.005
0
0.005
0.01
s^{-1}
(c)
Height [m]
NorthWest
174
102
Latitude
Longitude
A_3
14:29 JST
14:28 JST
-0.01
-0.005
0
0.005
0.01
s^{-1}

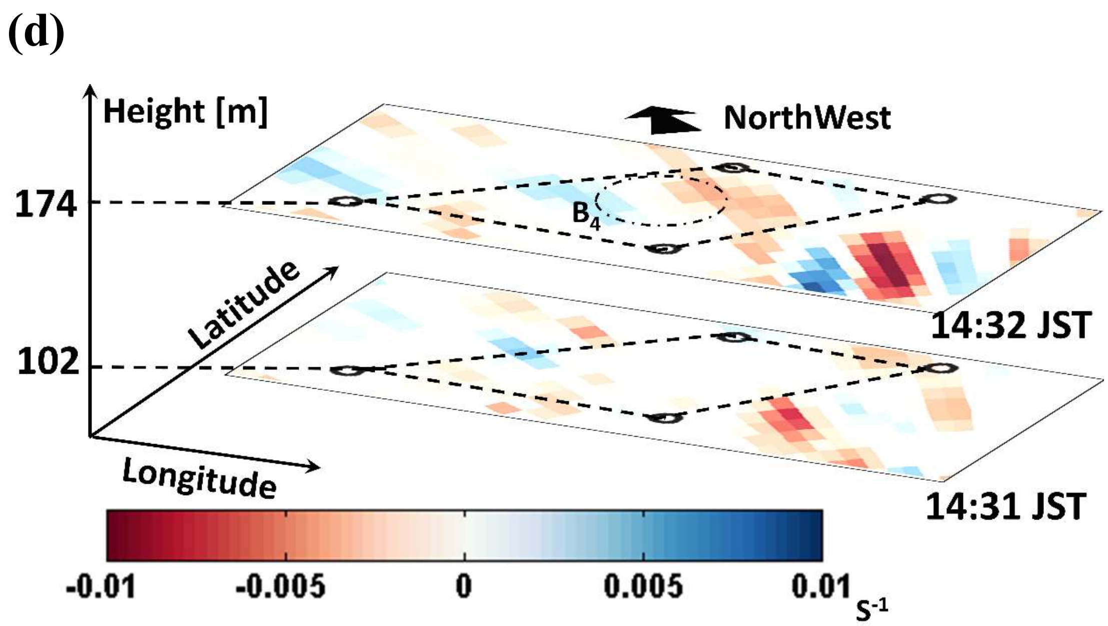

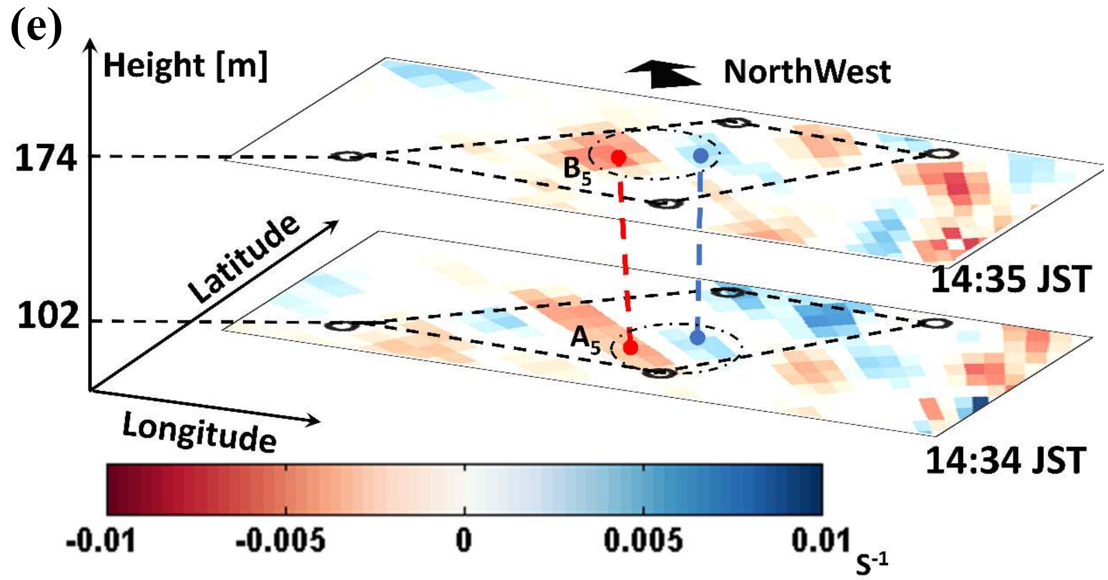

Figure 7.5. Vorticity, a) 14:22-14:23 JST, b) 14:25-14:26 JST, c) 14:28-14:29 JST, d) 14:31-14:32 JST. e) 14:34-14:35 JST.

The south-easterly environmental wind is a possible reason for the shifted location of B_1, B_2, and B_5. Wind direction profile from radiosonde at lower height from 30 m until 560 m (Figure 7.6a) showed 110° - 169°. The wind speed at those heights is from 0.5 – 3 m/s (Figure 7.6b), with the increased speed along the upper part supporting the tilted pairs of vorticity B_1, B_2, and B_5. This result showed that the vortex tube appears in the lower part of the cumulus cloud-baby rain cell stage before and during the first echo. Two of the three vortex tubes (14:22-14:23 and 14:34-14:35 JST) are inferred to have updraft existence (shown by continuous convergence area). Meanwhile, the shifted pair of vorticity at the upper height (B_1, B_2 and B_5) are inferred to the wind profile condition. Two early vortex tubes from Doppler lidar observation indicate that convective initiation already occurs before Ka-band first echo detection. This process relatively has a small value and comes from the flow structure below the cumulus cloud - baby rain cell stage.

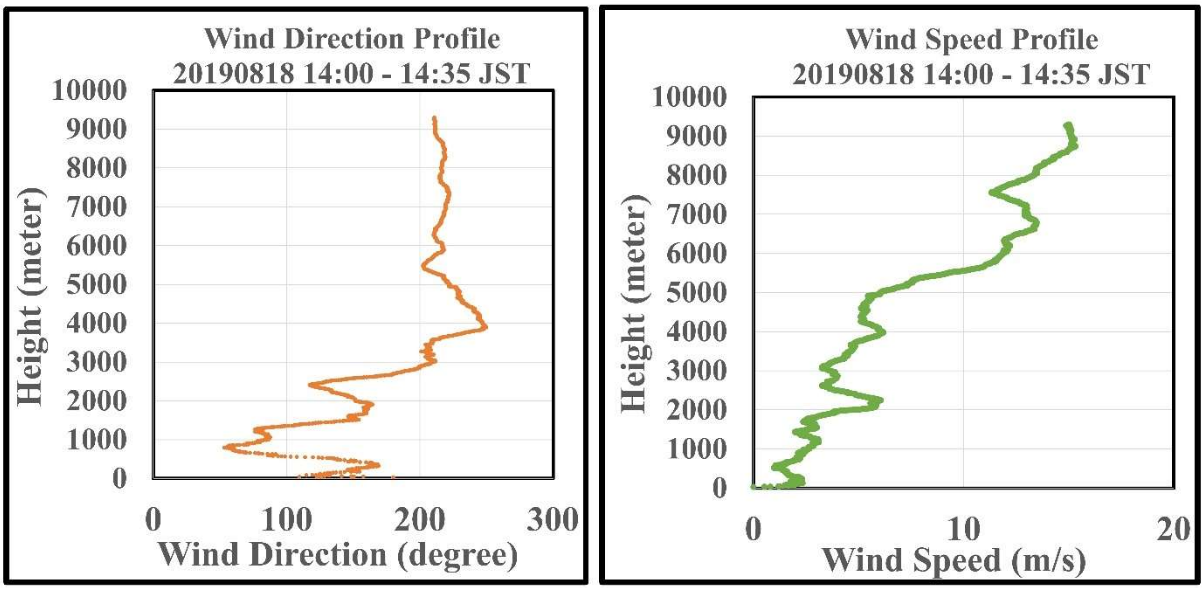

Figure 7.6. Radiosonde data, a) Wind direction, b) Wind speed.

This chapter showed the event where Ka-band radar detected the first echo from reflectivity data at 14:34 JST with an estimated echo height of 932 m. This cumulus cloud was categorized as isolated since from image sequence (14:20 JST until 14:40 JST) showed the cloud location in the same area. Doppler lidar observation showed a vortex tube at a lower height between 102 – 174 m at the same location during the Ka-band radar first echo (14:34-14:35 JST). Two early vortex tubes were also observed during the twelve minutes (14:22-14:23 JST) and nine minutes (14:25-14:26 JST) before the first echo. Two of the three vortex tubes are related to continuous convergence (strong updraft). Three of these vortex tubes have similar characteristics where the upper pair of vorticity is tilted to the northwest due to the environment wind profile at the lower level. The two early vortex tubes are related to the convective initiation process that Ka-band radar could not detect.

7.4. Meteorological analysis

Meteorological analysis during the small vortex tube was then carried out using radiosonde data. Radiosonde data was launched every one hour from 09:00 JST until 16:00 JST. CAPE and CIN are calculated on each radiosonde launch based on calculating the LFC, LCL, and EL. The skew T log P diagram is shown in the appendix to determine the CAPE and CIN calculation. Figure 7.7 shows the CAPE CIN time series data.

CAPE showed an increased value starting from 13:00 JST and reaching its maximum at 15:00 JST. This condition shows that the atmosphere is marginal to moderately unstable during the period from 13:00 – 15:00 JST. The moderately unstable condition occurs from 14:00 – 15:00 JST. However, the CAPE value is still less than the very unstable condition (2500 – 3500 J/Kg), so the isolated cumulus cloud did not develop even further into a cumulonimbus cloud.

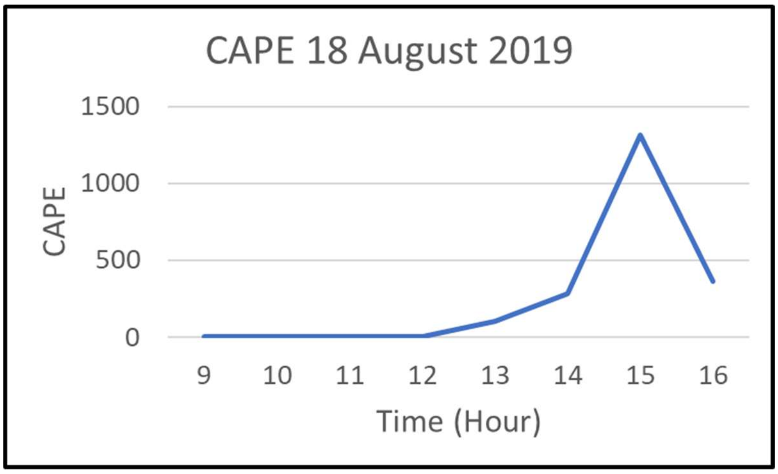

a)

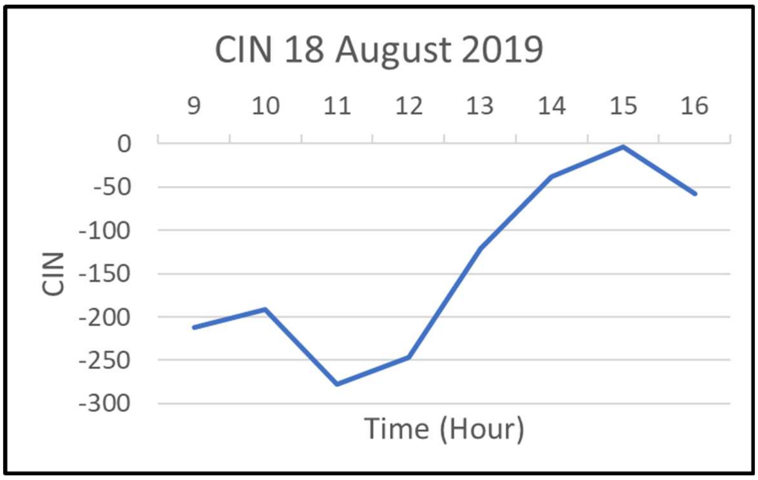

b)

Figure 7.7. Radiosonde calculation on August 18, 2019, a) CAPE, b) CIN

CIN value in Figure 7.7b decreases from 13:00 JST until 15:00 JST. The decrease in CIN negative value showed the decrease in the negative buoyancy energy that suppressed convective activity. This condition also supports the previous analysis by CAPE that the atmosphere is in an unstable condition. However, it is still not sure that CIN has a role in the undeveloped, isolated cumulus cloud.

CReSS simulation is also used to generate the vertical profile of temperature, pressure, and dew point, which are used to calculate the CAPE and CIN. Figure 7.8 compares CAPE and CIN from both radiosonde and CReSS. The pattern showed relatively the same, especially for CAPE. Meanwhile, CReSS cannot follow the radiosonde measurement pattern in CIN calculation. The reason is probably because of the lack of data on the lower height level from CReSS. If we increase the vertical resolution of CReSS, this will impact the time consumption of the simulation process. That is why we only calculate CAPE using CReSS data for another case study in a different period.

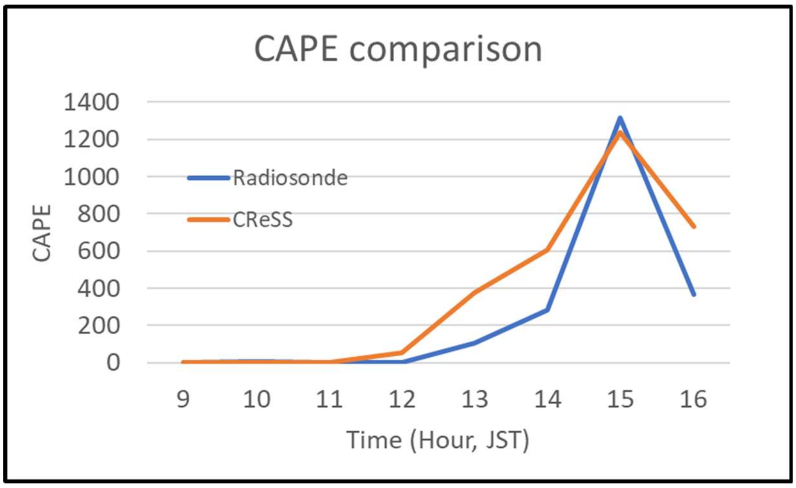

Figure 7. 8. Comparison between CReSS and Radiosonde for CAPE on case 1.

7.5. Comparison with other case studies

An additional case study for the vertical vorticity is added to observe these small vorticities in a different period. Table 7.1 compares the previous case study (case 1) with the additional case study (case 2).

Table 7.1. Comparison between two case study

Parameter	Case 1	Case 2
Date	2019-08-18	2018-09-11
Time of Ka-band radar first echo	14:34 JST	14:48 JST
Cloud estimated height from Ka-band radar	932 m	1078 m
Estimated distance: - from Ka-band radar location - from Doppler lidar location	 10.7 km 0.94 km	 11.27 km 1.55 km
Beam elevation angle where the first echo detected	5°	5°

Table 7.1 shows that the location of the cumulus cloud between case 1 and case 2 is different. Visual observation in Figure 7.9 using cameras showed the difference in the cloud position. In case 2, the cloud is located on the upper left side of the image. Meanwhile, in case 1 the position is more upper center.

a) b)

Figure 7.9. Camera cloud image in a different case study, a) case 1, b) case 2

Since there is no radiosonde data in case 2, horizontal wind comparison data is utilised from derived DBM BLR data on both case 1 and case 2 (Figure 7.10). In case 2, the condition of the lower dominant wind direction is toward the east direction. In theory, the horizontal vorticity is rolling in a clockwise direction. Once the uplift force exists, this will generate positive vorticity on the ride side and negative vorticity on the left side.

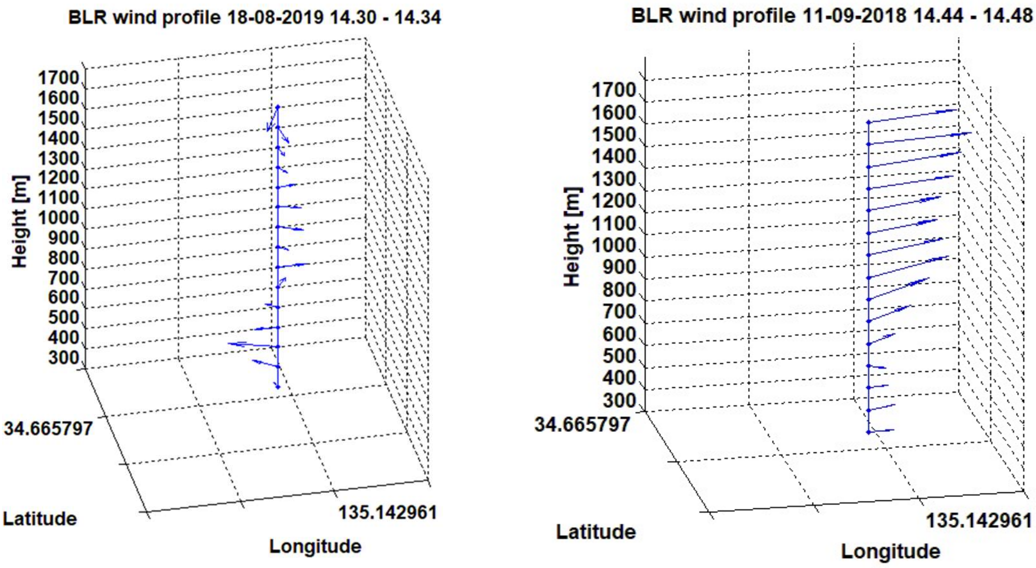

a) b)

Figure 7.10. DBM BLR horizontal wind profile, a) case study 1, b) case study 2.

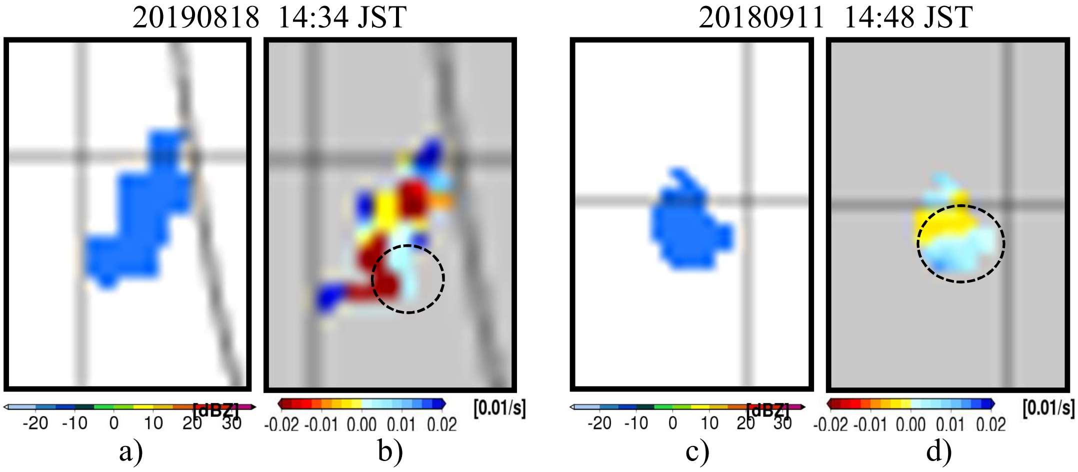

Figure 7.11. Ka band radar first echo, a) case study 1, b) case study 2.

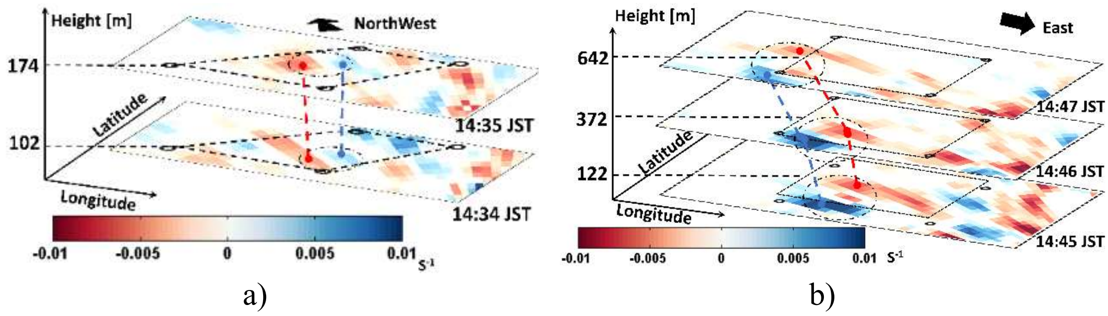

Figure 7.12. Doppler lidar vertical vorticity comparison during first echo, a) case 1, b) case 2.

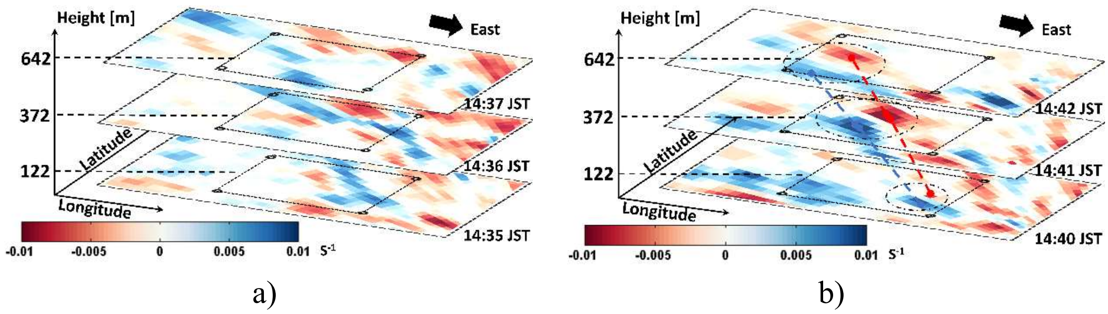

Figure 7.13. Case 2 of Doppler lidar vertical vorticity before the first echo, a) 14:35 until 14:37 JST, b) 14:40 until 14:42 JST.

Similar to Doppler lidar data case 1, in case 2 it is also found that the pair of vertical vorticity is located on each 122m, 372m, and 642m (vortex tube). This vortex tube is co-located with the area of the first echo of the Ka-band radar. In case 1, an early vortex tube is observed by Doppler lidar at 9 and 12 minutes before the first echo (Figure 7.5a and Figure 7.5b). In case 2, an early vortex tube is observed 5 minutes before the first echo (Figure 7.13b). Because of insufficient datasets, we could not calculate the relationship between Ka-band vertical vorticity and Doppler lidar vortex tube using wavelet coherence.

Observing the CAPE result using CReSS data showed that the CAPE value was not significantly high during the first echo in case 2 (102.4 J/Kg). This condition shows a marginally unstable condition (0 – 1000 J/Kg) during the Ka-band first echo. The maximum CAPE value occurs on 16 JST, which is 1741.6 J/Kg (Figure 7.14). The CAPE value in case 2 is still below the standard CAPE value for very unstable conditions (< 2500 J/Kg).

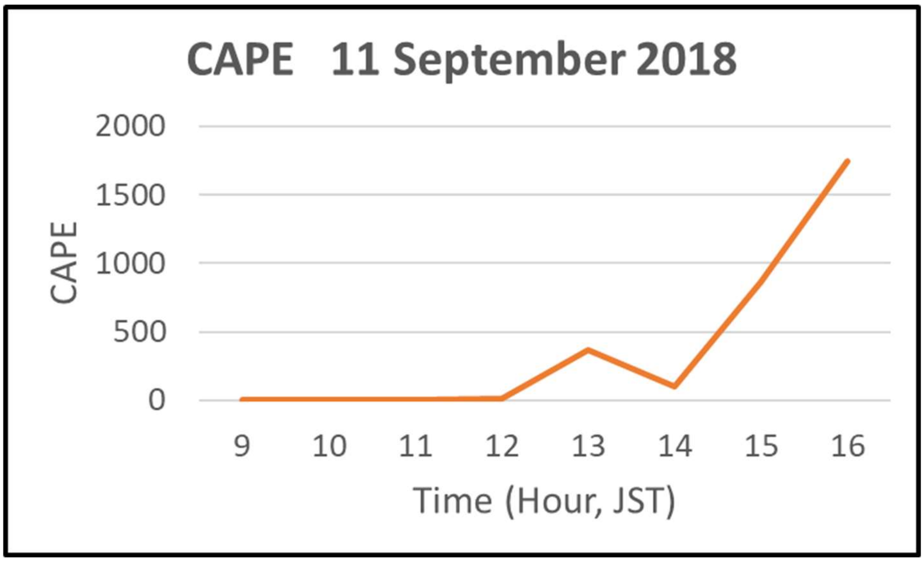

Figure 7.14. CAPE calculation based on CReSS data on case 2

This additional case study strengthens the analysis that a small vortex tube occurs during the early first echo of Ka-band radar. By comparing its location and orientation, this small vortex tube connects with the vertical vorticity inside the baby rain cell. Comparing the early vortex tube with the first echo showed that this small vortex tube has an early lead time of 5 to 9 min before the first echo. The strength of CAPE played a role in the cumulus cloud not developing even further.

Chapter 8. Summary and Conclusions

8.1. Summary of the cloud initiation process

A summary of our investigation of the cloud initiation stage is depicted in Fig. 8.1. In this figure, the cloud initiation stage is divided into two parts. The first parts describe the thermal plume interaction with the first cumulus cloud generated. Wavelet coherence showed a strong relationship between them, with thermal plume leading first before cumulus cloud appearance. The impact of thermal activity needs time to impact the cloud generation, at least more than two minutes. The investigation of the downdraft-updraft combination during convective conditions also added information on the thermal period pattern. During the impact of the thermal activity, there is a vertical vorticity with no vortex tube observed during this stage. However, there is no significant evidence that this vertical vorticity relates to the first cumulus cloud generation.

In the second part, in the cumulus humilis stage, we found a small vortex tube below the cloud location. This vortex tube is found several minutes before Ka-band radar detects the baby rain cell first echo. The range of the vorticity of this vortex tube is from $\pm$ 0.002 s^{-1} until $\pm$ 0.006 s^{-1}. This vortex tube orientation is very much affected by the environment wind. During the same period where the Ka-band detected the first echo, the small vortex tube detected by Doppler lidar has a relatively similar location and orientation regarding the vertical vorticity from Ka-band radar. This condition suggests that this small vortex tube is connected with the baby rain cell inside the cumulus cloud. One of many reasons why this baby rain cell did not develop significantly into GHR is that the condition of the CAPE is marginal to moderately unstable.

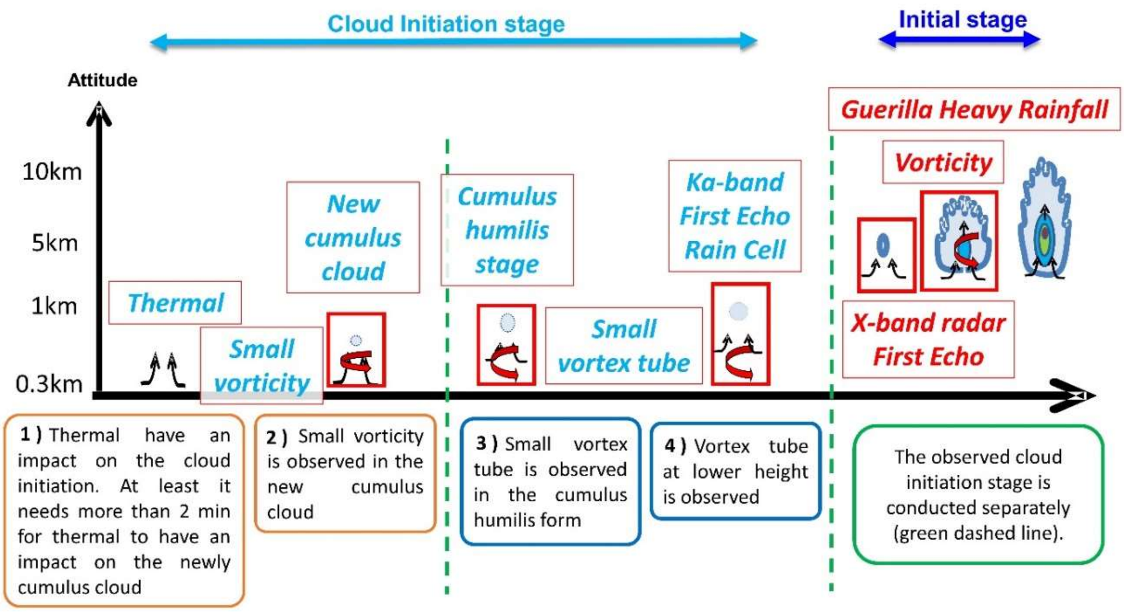

Figure 8.1. Schematic of the cloud initiation stage based on observation.

Practical implementation

8.2. Conclusion

This study aims to investigate the cloud initiation process to increase the lead time before the initial stage of GHR. We presented a comprehensive study from several aspects (physical, meteorological, measurement method, and dynamical aspect) concerning cloud initiation observation using several instruments. Chapter 5 found that advanced BLR combined with wavelet using appropriate mother wavelet could quantify the thermal plume coherent structure and the downdraft-updraft combination during this thermal plume. We also analyze the behavior of the downdraft-updraft combination in three different weather conditions (clear sky, cloudy, and convective condition).

The wavelet coherence proves that thermal activity leads to an individual cumulus cloud generation. This detailed analysis is presented in chapter 6. Thermal plume as the representation of the thermal activity has been compared with the cumulus cloud growth using wavelet coherence. The continuous leading phase coherence showed a strong relationship between these two variables. It takes at least more than two minutes for the thermal activity to impact the generation of the cumulus cloud.

We found another early indicator of the cumulus cloud stage that differs from a previous study by Nakakita et al. (2017). We found a vortex tube using Doppler lidar detected five to nine minutes before the Ka-band radar first echo. The vorticity value is small (less than $\pm$ 0.01 s^{-1}) than in the previous study. Due to its high sensitivity, this small vorticity could only be detected by Doppler lidar. A detailed explanation of this is described in chapter 7. Based on the sequence of study, we could illustrate the cloud initiation stage using three main instruments and a wavelet. Multi-instrument with wavelet could give detailed and new information on the cloud initiation process.

The clear mechanism of the cloud initiation stage directly related to GHR is still unresolved in this study. More extended observation is needed to catch the actual event of GHR at the same position as the co-located multiple instruments. An additional instrument and re-location of position also need to be considered to increase the probability of catching the GHR event.

In addition to future work, I will implement the pseudo vorticity method for the X-band radar data in Indonesia. Other methods such as stereo time lapse camera and CAPE-CIN calculation using radiosonde could also be included to observe cumulus cloud initiation in Indonesia.

Bibliography

Angevine, W.M., White, A.B., and Avery, S.K. (1994). Boundary-layer depth and entrainment zone characterization with a boundary-layer profiler. *Boundary-Layer Meteorology*, 68(4), 375-385.

Ahrens, C. D., & Henson, R. (2016). *Essentials of meteorology: An invitation to the atmosphere*. Cengage Learning.

Bilal, M, Solbakken, K, and Birkelund, Y. (2016). Wind speed and direction predictions by WRF and WindSim coupling over Nygardsfjell. *Journal of physics: Conference Series*, Vol 753, 8, p. 082018, IOP publishing.

Browning. K.A, A.M Blyth, P.A Clark, U Corsmeier, C.J Morcrette, J.L Agnew, S.P Ballard, D.Bamber, C.Barthlott, L.J Bennet, K.M Beswick, M. Bitter, K.E. Bozier, B.J.Brooks,C.G.Collier,F.Davies,B.Deny,M.A.Dixon,T.Feuerle,R.M.Forbes,C.Gaffard,M.D.Gray,R.Hankers,T.J.Hewison,N.Kalthoff,S.Khodayar,M.Kohler,C.Kottmeier,S.Kraut,M.Kunz,D.N. Ladd,H.W. Lean,J. Lenfant,Z. Li,J. Marsham,J. McGregor,S.D. Mobbs,J.Nicol,E. Norton,D.J. Parker,F. Perry,M. Ramatschi,H. M. A. Ricketts,N.M. Roberts,A. Russell,H. Schulz, E.C. Slack, G. Vaughan,J. Waight,D.P. Wareing,R.J. Watson, A.R. Webb, and A. Wieser. (2007). The convective storm initiation project. *Bulletin of the American Meteorological Society*, *88*(12), 1939-1956.

Chai,T., and Draxler,R.R. (2014). Root mean square error (RMSE) or mean absolute error (MAE). *Geoscientific Model Development Discussions*, 7(1), 1525-1534.

Chenari, H. M., and Mottaghian, F. (2020). Electrospun CuO/PVA fibers: Effects of heat treatment on the structural, surface morphology, optical and magnetic properties. *Materials Science in Semiconductor Processing*, 115, 105121.

Cheliotis, I., Dieudonné, E., Delbarre, H., Sokolov, A., Dmitriev, E., Augustin, P. and Fourmentin, M. (2020). Detecting turbulent structures on single Doppler lidar large datasets: an automated classification method for horizontal scans. *Atmospheric Measurement Techniques*, 13(12), 6579-6592.

Cohn, S.A., and Angevine, W.M. (2000). Boundary layer height and entrainment zone thickness measured by lidars and wind profiling radars. *Journal of Applied Meteorology*, 39(8), 1233-1247.

Cotton. W.R, Bryan. G, and Van den Heever. S.C. (2010). *Storm and Cloud Dynamics*, vol. 99, Academic Press.

Dahl, J. M. (2017). Tilting of horizontal shear vorticity and the development of updraft rotation in supercell thunderstorms. *Journal of the Atmospheric Sciences*, 74(9), 2997-3020.

Daubechies, I. (1990). The wavelet transform time-frequency localization and signal analysis. *IEEE Trans. Inform. Theory,* 36, 961–1004.

Davies, R., and Alves, A. R. (1989). Flux divergence of thermal radiation within stratiform clouds. *Journal of Geophysical Research: Atmospheres*, **94(D13)**, 16277-16286.

De Moortel, I., S.A. Munday, and A.W. Hood, (2004). Wavelet analysis: the effect of varying basic wavelet parameters, *Solar Physics*, 222(2), 203-228.

Donner, L. J. (1993). A cumulus parameterization including mass fluxes, vertical momentum dynamics, and mesoscale effects. *Journal of Atmospheric Sciences*, *50*(6), 889-906.

Fukao, S, and Hamazu, K. (2014). Radar for meteorological and atmospheric observations, Springer,

Gray, W.M., (2012). Fundamental importance of convective downdrafts and mass recycling within the tropical cloud cluster andhe typhoon-hurricane, *Tropical Cyclone Research and Review*, 1(1), 130-141.

Grinsted, A., Moore, J. C., and Jevrejeva, S. (2004). Application of the cross wavelet transform and wavelet coherence to geophysical time series. *Nonlinear processes in geophysics*, 11(5/6), 561-566.

Guan, H., Yau, M. K., and Davies, R. (1997). The effects of longwave radiation in a small cumulus cloud. *Journal of Atmospheric Sciences*, 54(17), 2201-2214

Huang, T., S.H.L. Yim, Y. Yang, O.S.M. Lee, D.H.Y. Lam, J.C.H. Cheng, and J. Guo. (2020). Observation of Turbulent Mixing Characteristic in the Typical Daytime Cloud-Topped Boundary Layer over Hng Kong in 2019. *Remote Sensing*, 12(9), 1533.

Hudson, J. G., & Noble, S. (2021). Cumulus Cloud and Drizzle Microphysics Relationships With Complete CCN Spectra. *Journal of Geophysical Research: Atmospheres*, *126*(15), e2021JD034966.

Iwai, H, Ishii, S, Kawamura, S, Sato, E, and Kusunoki, K. (2017). Case study on convection initiation associated with an isolated convective storm developed over flat terrain during TOMACS. *Journal of the Meteorological Society of Japan. Ser. II*.

Kain, J.S. (2004). The Kain–Fritsch convective parameterization: an update, *Journal of Applied Meteorology* ,43(1), 170-181.

Katayama, M., Yamaji, A., Nakamura, F., Morita, H. and Nakakita, E. (2015). Development of a system for early detection of a severe storm. *Advances in River Engineering*, Vol 21, 401-406 (Japanese).

Klemp, J.B. (1987). Dynamics of tornadic thunderstorms, *Annual Review of Fluid Mechanics*, vol. 19, no. 1, 369–402.

Klinger, C., Mayer, B., Jakub, F., Zinner, T., Park, S. B., & Gentine, P. (2017). Effects of 3-D thermal radiation on the development of a shallow cumulus cloud field. *Atmospheric Chemistry and Physics*, *17*(8), 5477-5500.

Knight, C. A. and Miller, L.J. (1993). First radar echoes from cumulus clouds. *Bulletin of the American Meteorological Society*, 74(2), 179-188.

Kollias, P., Albrecht, B. A., Lhermitte, R., and Savtchenko, A. (2001). Radar observations of updrafts, downdrafts, and turbulence in fair-weather cumuli. *Journal of the atmospheric sciences*, 58(13), 1750-1766.

Liu, B., J. Guo, W. Gong, L. Shi, Y. Zhang, and Y. Ma, (2020). Characteristics and performance of wind profiles as observed by the radar wind profiler network of China, *Atmospheric Measurement Techniques*, 13(8), 4589-4600.

López, R. E. (1977). The lognormal distribution and cumulus cloud populations. *Monthly Weather Review*, 105(7), 865-872.

Maesaka, T. (2018). Cloud radars. In C. Andronache (Ed.), *Remote sensing of clouds and precipitation* , 137–152).

Mecikalski, J. R., Jewett, C. P., Apke, J. M., and Carey, L. D. (2016). Analysis of cumulus cloud updrafts as observed with 1-min resolution Super Rapid Scan GOES imagery. *Monthly Weather Review*, 144(2), 811-830.

Misumi, R., Sakurai, N., Maesaka, T., Suzuki, S. I., Shimizu, S., and Iwanami, K. (2017). Transition process from non-precipitating cumuli to precipitating convective clouds over mountains: Observation by Ka-band Doppler radar and stereo photogrammetry. *Journal of the Meteorological Society of Japan. Ser. II*.

Nakakita, E., H. Sato, R. Nishiwaki, H. Yamabe, and K. Yamaguchi, (2017a). Early detection for baby-rain-cell aloft in a severe storm and risk projection for urban flash flood, *Advances in Meteorology* ,1-15.

Nakakita, E., Niibo, T., Sato, H. and Yamaguchi, K. (2017b). Preliminary analysis of cumulonimbus cloud structure using multi parameter information of Ka-band polarimetric Doppler radar. *DPRI Annuals*, No. 60 B (Japanese).

Nugroho, G. A., Yamaguchi, K., Nakakita, E., Yamamoto, M. K., and Kawamura, S. (2021). Utilization of High-Resolution Boundary Layer Radar and Wavelet to Detect Microscale Downdraft-Updraft Combination. *SOLA*, 17, 63-68.

Nugroho, G. A., & Sinatra, T. (2019, July). Comparison and Analysis of The First Signal Detection of Two X-Band Radar with RGB Himawari Satellite Data before Localized Heavy Rain March 17 2017 Bandung Basin Indonesia. In *IOP Conference Series: Earth and Environmental Science* (Vol. 303, No. 1, p. 012056). IOP Publishing.

Newsom, R. K., and Krishnamurthy, R. (2020). Doppler lidar (DL) handbook (No. DOE/SC-ARM/TR-101). *DOE Office of Science Atmospheric Radiation Measurement (ARM) Program (United States).*

Ng, E. K., and Chan, J. C. (2012). Geophysical applications of partial wavelet coherence and multiple wavelet coherence. *Journal of Atmospheric and Oceanic Technology*, *29*(12), 1845-1853.

Ohigashi, T., Tsuboki, K., Shinoda, T., Minda, H., Kyushima, M., Yamada, H., and Iwai, H, (2021). Mammatus-Like Echo Structures along the Base of Upper-Tropospheric Outflow-Layer Clouds of Typhoons Observed by Cloud Radar. *Geophysical Research Letters*,48, e2021GL094973.

Pearson, R. K., Neuvo, Y., Astola, J., and Gabbouj, M. (2016). Generalized hampel filters. *EURASIP Journal on Advances in Signal Processing*, *2016*(1), 1-18.

Romps, D. M., and Öktem, R. (2018). Observing clouds in 4D with multiview stereophotogrammetry. *Bulletin of the American Meteorological Society*, 99(12), 2575-2586.

Rotunno. R. (1981). On the evolution of thunderstorm rotation, *Monthly Weather Review*, 109(3), 577–586.

Rio, C., and Hourdin, F. (2008). A thermal plume model for the convective boundary layer: Representation of cumulus clouds, *Journal of the atmospheric sciences*, 65(2), 407-425.

Sengupta, S. K., Welch, R. M., Navar, M. S., Berendes, T. A., & Chen, D. W. (1990). Cumulus cloud field morphology and spatial patterns derived from high spatial resolution Landsat imagery. *Journal of Applied Meteorology and Climatology*, *29*(12), 1245-1267.

Shakti, P.C., Nakatani,T., and Misumi, R. (2019). The role of spatial distribution of radar rainfall on hydrological modelling for an urbanized river basin in Japan. *Water*, 11(8), 1703.

Schwiesow, R., Köpp, P., and Werner, C. (1985). Comparison of CW-lidar-measured wind values obtained by full conical scan, conical sector scan and two-point techniques. *J. Atmos. Oceanic Technol,* **2,** 3–14.

Terradellas, E., G. Morales, J. Cuxart, and C. Yagüe. (2001). Wavelet methods: application to the study of the stable atmospheric boundary layer under non-stationary conditions, *Dynamics of Atmospheres and Oceans*, 34(2-4), 225-244.

Tian, J., Zhang, Y., Klein, S. A., Wang, L., Öktem, R., and Romps, D. M. (2021). Summertime Continental Shallow Cumulus Cloud Detection Using GOES-16 Satellite and Ground-Based Stereo Cameras at the DOE ARM Southern Great Plains Site. *Remote Sensing*, 13(12), 2309.

Torrence, C., and Compo, G. P. (1998). A practical guide to wavelet analysis. *Bulletin of the American Meteorological society*, 79(1), 61-78.

Trier.S.B. (2003). Convective Initiation, *Encyclopedia of Atmospheric Sciences* , 560-570.

Wang, H., Barthelmie, R. J., Clifton, A., and Pryor, S.C. (2015). Wind measurements from arc scans with Doppler wind lidar. *Journal of Atmospheric and Oceanic Technology*, 32(11), 2024-2040.

Wang, Y., Geerts, B., & French, J. (2009). Dynamics of the cumulus cloud margin: An observational study. *Journal of the atmospheric sciences*, *66*(12), 3660-3677.

Welford, B. P. (1962). Note on a method for calculating corrected sums of squares and products. *Technometrics*, 4(3), 419-420.

Wiebe, A., Sturman. A., and McGowan, H. (2011). Wavelet analysis of atmospheric turbulence over a coral reef flat, *Journal of Atmospheric and Oceanic Technology*, 28(5), 698-708.

Yano, J. I., and Jakubiak, B. (2016). Wavelet-based verification of the quantitative precipitation forecast. *Dynamics of Atmospheres and Oceans*, 74, 14-29.

Yamaguchi, K., Tsuchihashi.T ., and Nakakita.E. (2018). Analysis of the Formation of Vortex Tube and Thermals Above Urban Area by Urban Meteorological Model Based on Large Eddy Simulation, *DPRI Annuals*, 62B (Japanese).

Yamamoto, M. K., Fujita, T., Aziz, N. H. B. A., Gan, T., Hashiguchi, H., Yu, T. Y., and Yamamoto, M. (2014). Development of a digital receiver for range imaging atmospheric radar. *Journal of Atmospheric and Solar-Terrestrial Physics*, 118, 35-44.

Yamamoto, M. K., Kawamura, S., and Nishimura, K. (2018). Facility implementation of adaptive clutter suppression to an existing wind profiler radar: First result, *IEICE Communications Express*, *7*(3), 107-107.

Zhang, Y., and Klein, S. A. (2013). Factors controlling the vertical extent of fair-weather shallow cumulus clouds over land: Investigation of diurnal-cycle observations collected at the ARM Southern Great Plains site. *Journal of the Atmospheric Sciences*, 70(4), 1297-1315.

APPENDIX

A. Skew T log P

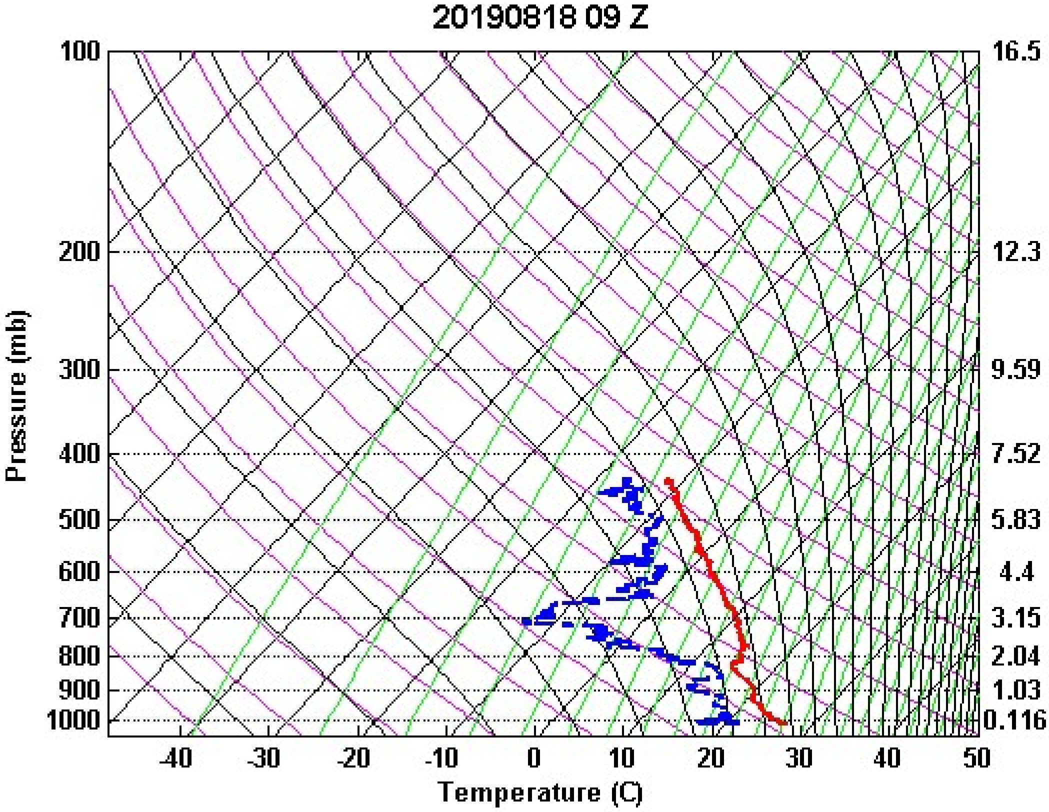

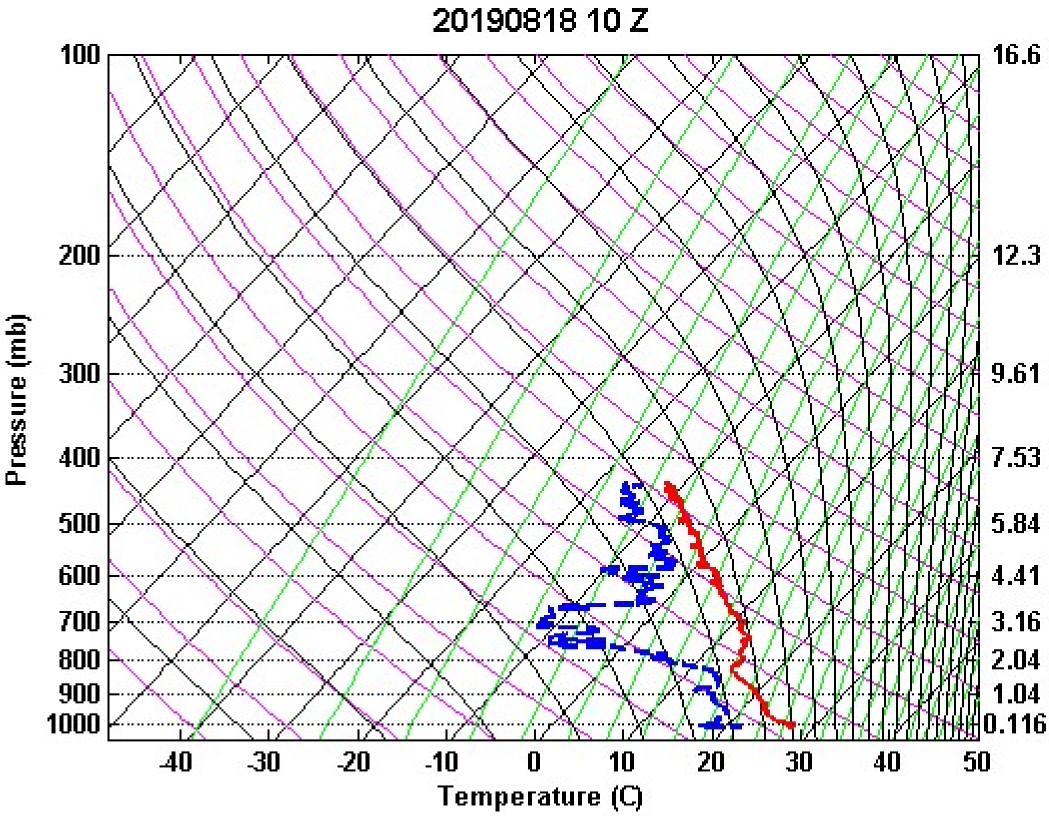

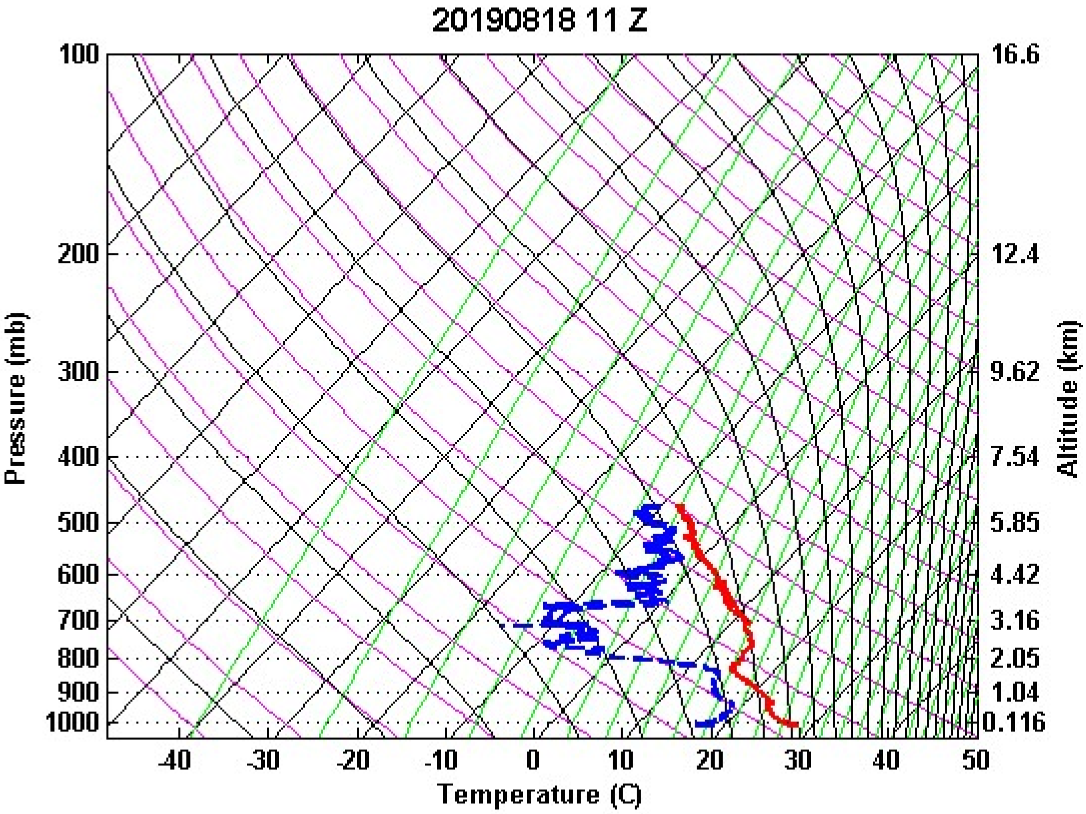
20190818 11 Z
Pressure (mb)
100
200
300
400
500
600
700
800
900
1000
Altitude (km)
16.6
12.4
9.62
7.54
5.85
4.42
3.16
2.05
1.04
0.116
-40 -30 -20 -10 0 10 20 30 40 50
Temperature (C)

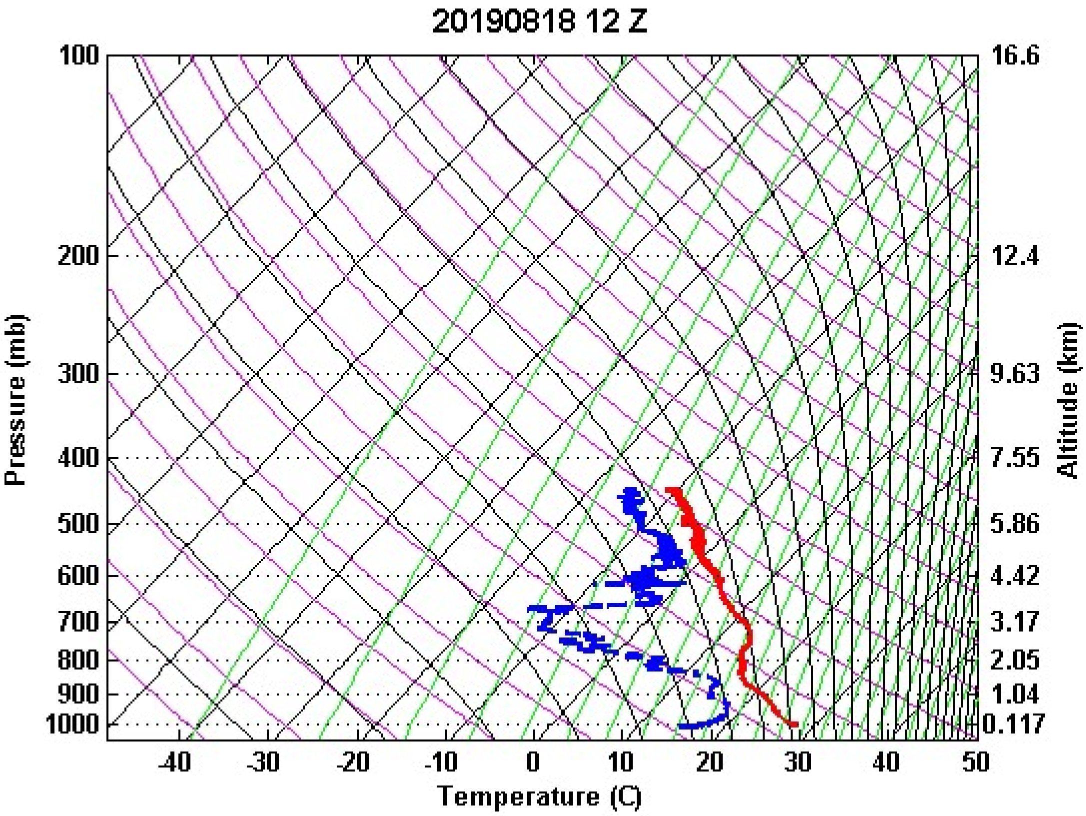
20190818 12 Z
Pressure (mb)
100
200
300
400
500
600
700
800
900
1000
Altitude (km)
16.6
12.4
9.63
7.55
5.86
4.42
3.17
2.05
1.04
0.117
-40 -30 -20 -10 0 10 20 30 40 50
Temperature (C)

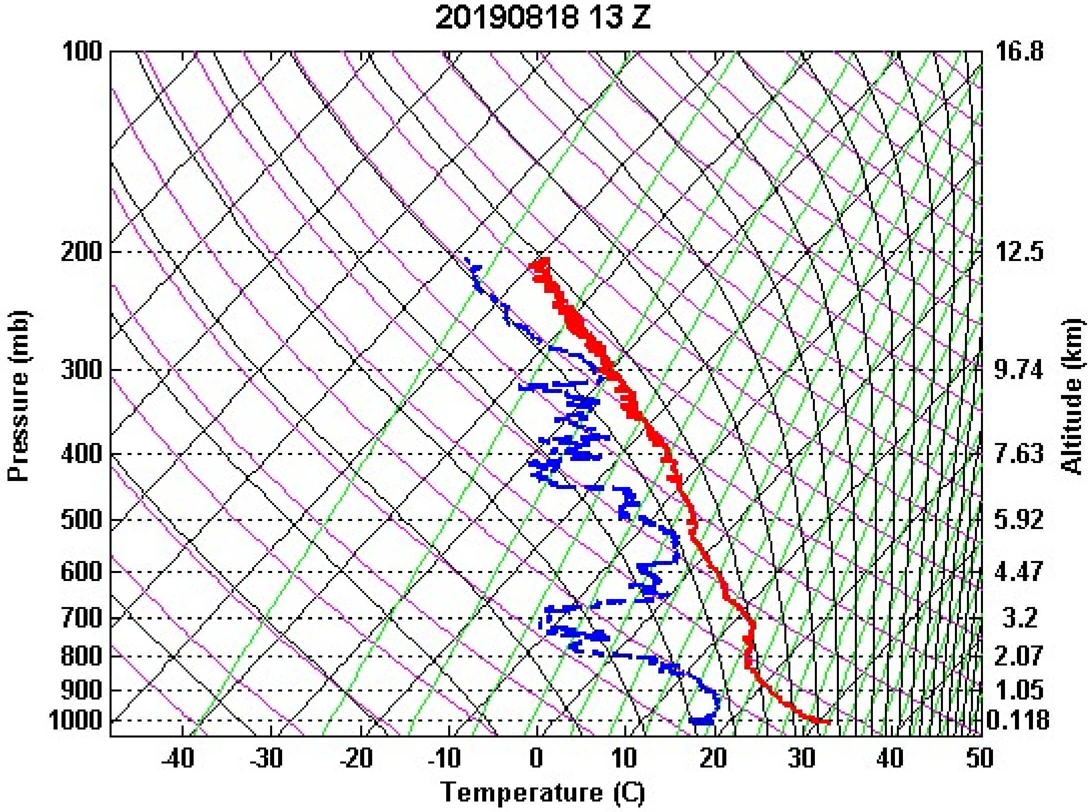
20190818 13 Z
Pressure (mb)
100
200
300
400
500
600
700
800
900
1000
Altitude (km)
16.8
12.5
9.74
7.63
5.92
4.47
3.2
2.07
1.05
0.118
-40 -30 -20 -10 0 10 20 30 40 50
Temperature (C)

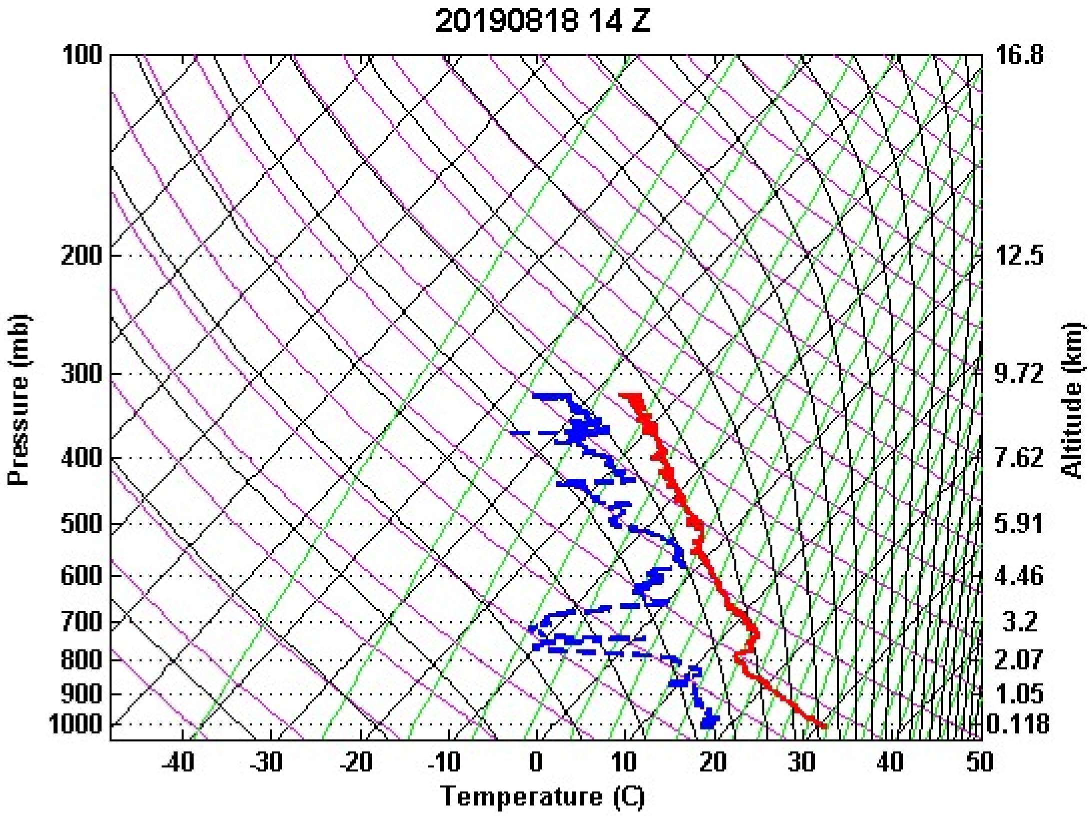
20190818 14 Z
Pressure (mb)
100
200
300
400
500
600
700
800
900
1000
Altitude (km)
16.8
12.5
9.72
7.62
5.91
4.46
3.2
2.07
1.05
0.118
-40 -30 -20 -10 0 10 20 30 40 50
Temperature (C)

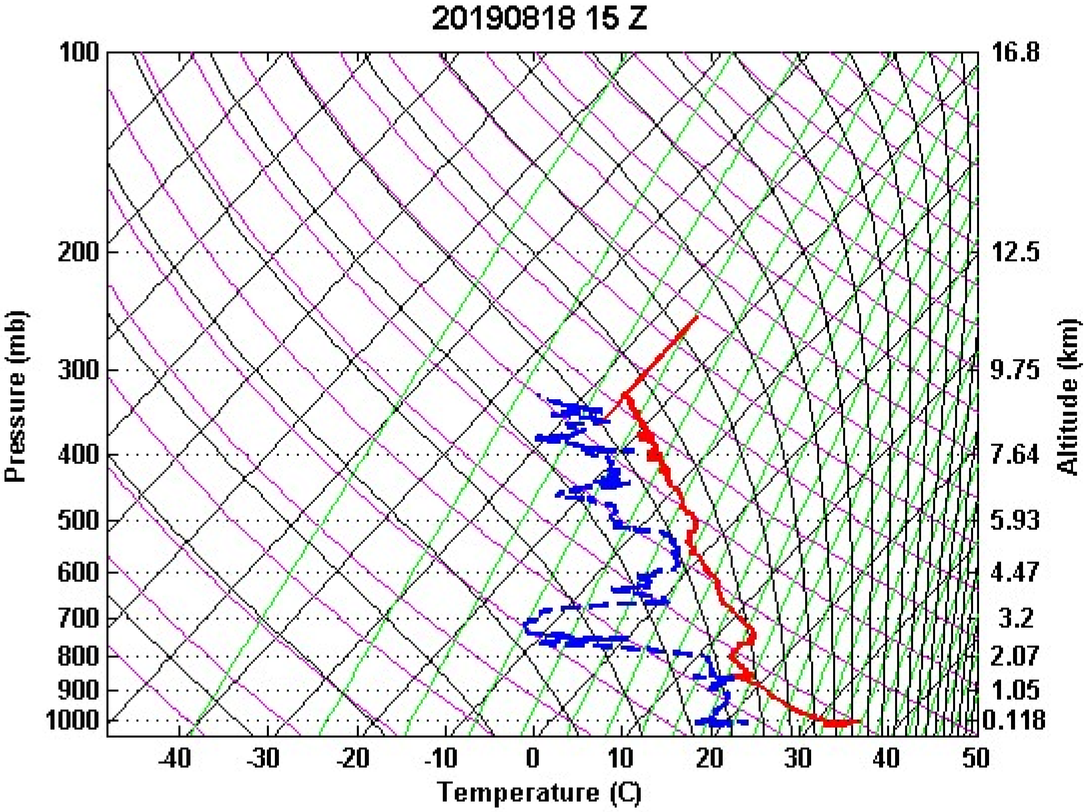
20190818 15 Z
Pressure (mb)
100
200
300
400
500
600
700
800
900
1000
Altitude (km)
16.8
12.5
9.75
7.64
5.93
4.47
3.2
2.07
1.05
0.118
-40 -30 -20 -10 0 10 20 30 40 50
Temperature (C)

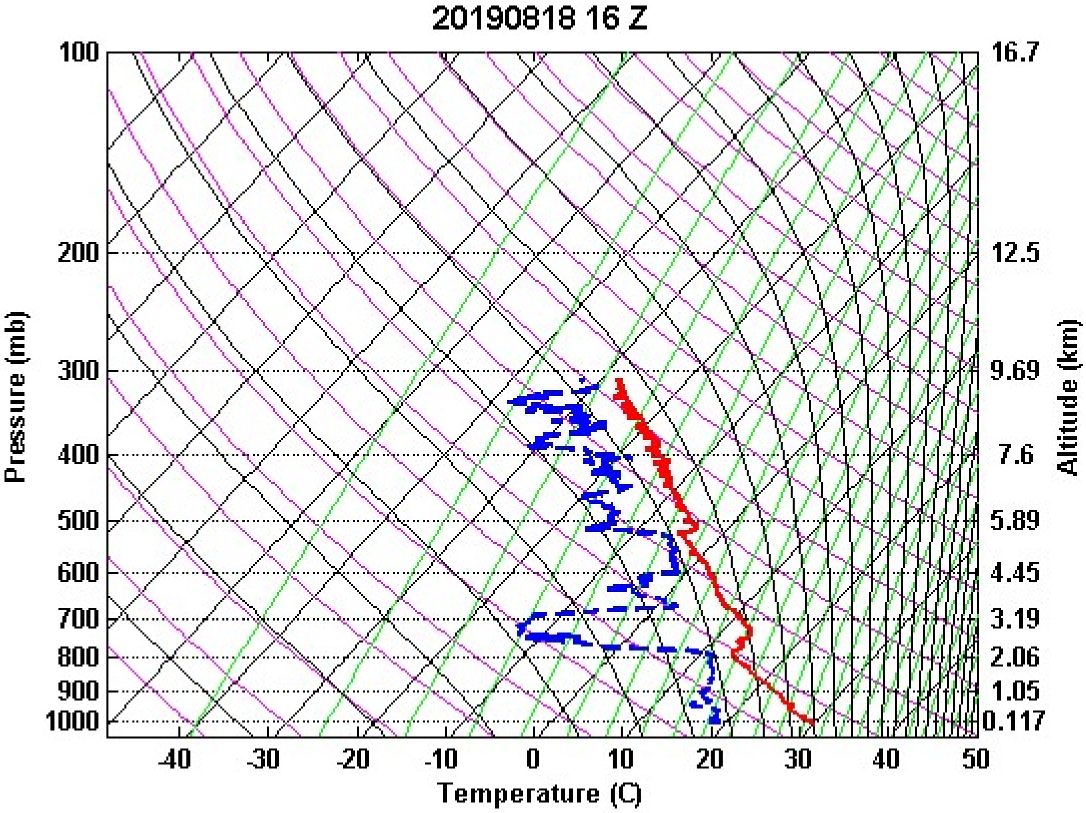
20190818 16 Z
Pressure (mb)
100
200
300
400
500
600
700
800
900
1000
Altitude (km)
16.7
12.5
9.69
7.6
5.89
4.45
3.19
2.06
1.05
0.117
-40 -30 -20 -10 0 10 20 30 40 50
Temperature (C)

B. Convergence-Divergence on Case 2